Lehigh University
Lehigh Preserve

Theses and Dissertations

1990

# Electron energy-loss spectrum imaging in the electron microscope

John Andrew Hunt
*Lehigh University*

Follow this and additional works at: https://preserve.lehigh.edu/etd

Part of the Materials Science and Engineering Commons

Recommended Citation
Hunt, John Andrew, "Electron energy-loss spectrum imaging in the electron microscope" (1990). *Theses and Dissertations*. 5271.
https://preserve.lehigh.edu/etd/5271

This Thesis is brought to you for free and open access by Lehigh Preserve. It has been accepted for inclusion in Theses and Dissertations by an authorized administrator of Lehigh Preserve. For more information, please contact preserve@lehigh.edu.

# Electron Energy-Loss Spectrum Imaging

# in the Electron Microscope

by

John Andrew Hunt

A Thesis

Presented to the Graduate Committee

of Lehigh University

in Candidacy for the Degree of

Master of Science

in Materials Science and Engineering

Lehigh University

1989

# Certificate of Approval

This thesis is accepted in partial fulfillment of the requirements for the degree of Master of Science.

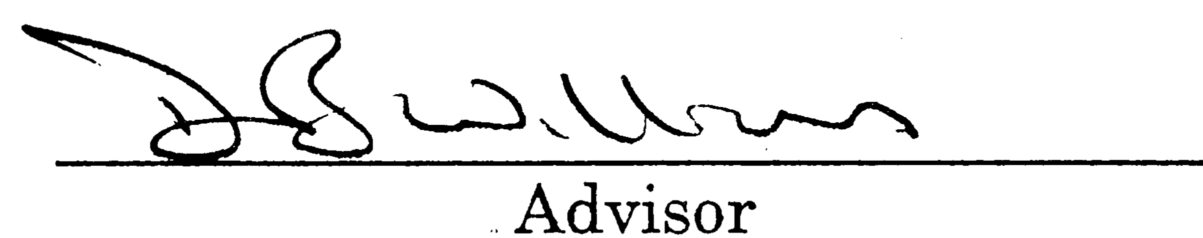

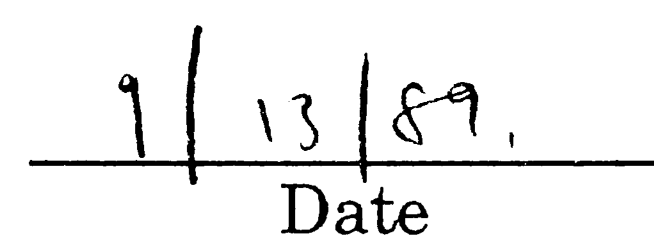

Advisor — Date

Department chairperson — Date

# Acknowledgements

As usual, the author is indebted to many individuals. I would like to thank Professor Dave Williams at Lehigh for supporting me as a graduate student and for his extrordinary patience. Chuck Fiori at NIH started me at NIH and provided his personal computer for the majority of computational work. Carol Swyt at NIH contributed many useful conversations that were particularly important to my understanding of multiple least-squares techniques. Richard Leapman at NIH is to be thanked for allowing me to work with him on numerous projects, and for frequent and inexhaustible late-night conversations on EELS. Lastly, I am grateful to the National Science Foundation for allowing me to escape the real world for several more years through their funding of this work.

# Prologue

The work described hereafter was not originally sought as a thesis project. Instead the author, in an attempt to learn about the field of electron energy-loss spectroscopy (EELS), wandered through various parts of this field, trying whatever techniques or experiments seemed interesting. This work was selected as the thesis because the work was particularly successful and relevant to the electron microscopy community.

The majority of the theoretical work and computer programming was performed at Lehigh University, as well as all inorganic sample preparation. The presented experimental work was carried out at the Electron Beam Imaging and Microanalysis lab at the National Institutes of Health (NIH) in Bethesda, Maryland. The majority of experiments were performed on a Hitachi H700H transmission electron microscope. Work since June 1989 was performed on a Vacuum Generators HB501 dedicated scanning electron microscope. None of the organic sample preparation was performed by the author. All presented EELS work was done using a GATAN 666 parallel EELS spectrometer.

This document assumes the reader is familiar with electron microscopy, but not necessary in the field of EELS. Connectivity diagrams and flow charts appear in place of exact schematics and the over one hundred thousand lines of code. The latter can be made available to those interested, but this paper is not the place for them.

# Table of Contents

**Certificate of Approval** ii
**Acknowledgements** iii
**Prologue** iv(a)
**Abstract** 1
**1. Introduction** 2
**2. Electron Energy-Loss Spectroscopy** 4
2.1 The Energy-Loss Spectrum 8
~~2.2 Electron Scattering~~ 10
2.3 Theory and Models 14
2.3.1 Cross sections 14
2.3.2 Elastic scattering models 15
2.3.3 Inelastic Scattering 17
2.3.4 Quantification using EELS 20
2.3.5 Correlation of dielectric response to cross sections 23
**3. Parallel EELS** 25
3.1 PEELS advantages 25
3.1.1 Core-loss collection efficiency 25
3.1.2 Minimizing electron dose 26
3.2 PEELS disadvantages 26
3.2.1 Artifacts 27
3.2.2 Detector limitations 27
3.2.3 Low dosage insensitivity 28
3.3 PEELS artifacts 28
3.4 Correcting PEELS artifacts 30
3.4.1 Problems in finding the channel-to-channel gain function 31
3.4.2 Gain averaging 33
3.4.3 Difference spectra 33
**4. Imaging** 37
4.1 "On-the-fly" processing techiniques 38
4.2 Batch processing 39
4.3 Drift corrections 40
4.3.1 Energy-drift correction 41
4.3.2 Probe current drift correction 42
4.3.3 Spatial-drift correction 43
**5. EELS Quantificational Imaging** 44
5.1 Two-area method 44
5.2 Linear Least-Squares 45
5.3 Comments on fitting with the two-area and LLS methods 46
5.4 Multiple Least Squares 48
5.4.1 Generalized principle of EELS MLS 49
5.4.2 Separation of core-loss signals from multiple isomorphs 51
5.5 Extended Energy-Loss Fine Structure (EXELFS) 53

5.5.1 Extended X-ray Absorption Fine Structure (EXAFS) 54
5.5.2 EXELFS Theory 55
5.5.3 Data Acquisition 61
5.5.4 Data Analysis 62
5.5.5 Conclusions on EXELFS imaging 63
5.6 Dielectric response images 63
5.6.1 Relating optical permittivity with electronic permittivity 65
5.6.2 Scattering vector dependent dielectric response experiments 67
5.6.3 Acoustic modes 67
**6. Hardware and software design** **70**
6.1 Hardware 70
6.1.1 Computer interfaces 72
6.1.2 System connections 73
6.2 Software processes 73
6.2.1 Machine-level drivers 77
6.3 Calling drivers through HLLs 79
**7. Spectrum-imaging software tools** **85**
**8. Sample experiments** **87**
**9. Conclusions** **92**
9.1 Summary of design achievements 92
9.2 Summary of experiments 93
9.3 The future of spectrum-imaging 94
9.4 Summing up ... 95
**References** **96**
**Vita** **99**

# List of Figures


**Figure 2-1:** Schematic diagram of a REELS experiment. Electrons pass from the source through the monochromator, strike the sample, and the energy spectrum of the scattered electrons is probed by a second monochromator. (Ibach..,1982) 5

**Figure 2-2:** Schematic view of a TEM EELS configuration (Williams,1987) 5

**Figure 2-3:** Typical magnetic serial EELS spectrometer. (Williams,1987) 6

**Figure 2-4:** Schematic diagram of the Gatan parallel-detection EELS spectrometer showing the pre-prism focussing coils, prism, post prism focussing coils and quadrupole lenses, and detector assembly (Krivanek,1988) 7

**Figure 2-5:** Typical EELS spectrum. (Williams, 1987) 8

**Figure 2-6:** A classical (particle) view of electron scattering by a single atom. (carbon) (a) Elastic scattering is caused by Coulomb attraction of the nucleus. Inelastic scattering results from Coulomb repulsion by (b) inner- or (c) outer-shell atomic electrons, which are excited to a higher energy state. The reverse transitions are shown by broken arrows. (Egerton,1986) 11

**Figure 2-7:** Energy-level diagram of a solid, including K- and L-shell core levels and a valance band of delocalized states (shaded); $E_F$ is the Fermi level and $E_{vac}$ the vacuum level. The primary processes of inner- and outer-shell excitation are shown on the left, secondary processes of photon and electron emission on the right. (Egerton,1986) 12

**Figure 2-8:** Angular distribution of various electron scattering phenomena. (Joy..,1979) 14

**Figure 2-9:** Scattering planes with wave vectors of incident beam ($\mathbf{k}_0$) and scattered beam ($\mathbf{k}_1$). $\mathbf{q}$ is the wave vector transferred to the target. (Schattschneider,1986) 15

**Figure 2-10:** Rutherford scattering of an electron by the electrostatic field of an atomic nucleus, viewed from a classical perspective. Each scattering angle $\theta$ corresponds to a particular impact parameter $b$; as $b$ increases, $\theta$ decreases. (Egerton,1986) 16

**Figure 2-11:** Angular dependence of differential cross sections for elastic and inelastic scattering of 100 keV electrons from a carbon atom, calculated using the Lenz model. (Langmore..,1973) (Egerton,1986) 18

**Figure 2-12:** Real and imaginary parts of the relative permittivity and the energy-loss function $IM\{-1/\varepsilon(\omega)\}$, calculated using a free- electron (jellium) model with $E_p$=15 eV and 20

$\hbar/\tau = 4$ eV (Raether,1980)
**Figure 2-13:** Bethe surface for K-shell ionization, calculated using a hydrogenic model. The horizontal coordinate is related to scattering angle. (Egerton,1979) 21
**Figure 2-14:** Regions in an EELS spectrum useful for quantification of more than one edge. (Williams, 1987) 22
**Figure 3-1:** Dark current from a Gatan PEELS spectrometer with no incident electron illumination. Acquisition time is 1 s 30
**Figure 3-2:** Channel-to-channel gain variations superimposed upon the uneven illumination of the dispersed zero-loss. 31
**Figure 3-3:** First difference spectrum showing carbon, nitrogen, and oxygen K edges 34
**Figure 3-4:** Second difference spectra of same specimen in figure 3-3 but using different energy windows. 35
**Figure 5-1:** The two-area method of background fitting 45
**Figure 5-2:** Carbon core-loss structures of a) formvar b) graphite c) diamond 52
**Figure 5-3:** EXAFS of one glassy and two crystalline forms of $GeO_2$ as a function of energy above the Ge K-shell ionization edge. (Kittel, 1986) 55
**Figure 5-4:** Left: EELS spectrum of amorphous SiN. Right: EXELFS of amorphous SiN after background subtraction. Si K-edge (solid line) and N K-edge (dashed line) shown. (Leapman,1982) 56
**Figure 5-5:** Pictorial representation of the electron interference that causes EXELFS. The ejected electron comes from the A atom. The solid circles represent the peaks of the outgoing wave function, while the dashed circles represent wave functions of backscattered electrons. Constructive interference is portrayed in **A** and destructive interference in **B**. (Schattschneider, 1986) 57
**Figure 5-6:** Mean free path for inelastic scattering of an electron. (Egerton, 1986) 60
**Figure 5-7:** Energy-loss functions for Cu and Au; the bold lines are from energy-loss measurements, the other lines were calculated from optical measurements. (Kittel,1986) 65
**Figure 5-8:** The energy-loss function $IM[-1/\varepsilon]$ and the real part $\varepsilon_1$ of the dielectric function, derived from EELS on polycrystalline films of silver, gold, and copper. (Daniels..,1970) 66
**Figure 5-9:** Electric field lines associated with surface plasmons excited in a bulk sample (a) and in a thin film (b and c). The plasmon frequency is higher in the symmetric mode (b) than in the asymmetric one (c). 69
**Figure 6-1:** Transfer of data from an I/O device into memory with and without DMA. 72
**Figure 6-2:** System connections of the spectrum-imaging system. 74
**Figure 6-3:** Dark-field acquistion interface. 75

**Figure 6-4:** EDS interface. 75
**Figure 6-5:** PEELS spectrometer interface. 76
**Figure 6-6:** Scanning coils interface. One circuit is used for each of two scan inputs. 76
**Figure 6-7:** CRT beam blanking interface. 76
**Figure 6-8:** Diagram of data being transferred from a Gatan PEELS spectrometer. 78
**Figure 6-9:** Flow chart of the PEELS driver. 79
**Figure 6-10:** Diagram of data being transferred from an EDS spectrometer. 80
**Figure 6-11:** Flow chart of the EDS driver. 81
**Figure 6-12:** Flow chart of a simple MCA display routine. 82
**Figure 6-13:** Minimizing dead time while processing on-the-fly. 82
**Figure 6-14:** Minimizing dosage during normal spectrum collection using a pre-specimen beam-blanker. 83
**Figure 6-15:** Collecting mass-loss data with a pre-specimen beam-blanker. 83
**Figure 6-16:** Collecting both a CL and a LL using a pre-specimen beam-blanker. 84
**Figure 8-1:** Processed image planes from a spectrum-image of ferritin molecules showing iron, carbon, nitrogen, and oxygen. The analysis method was linear least-squares with energy-drift corrections. 87
**Figure 8-2:** Processed image planes from a spectrum-image of myotube cells showing nitrogen, carbon, calcium, and oxygen. The analysis method was linear least-squares with energy-drift corrections. Note the total loss of beam current near the middle of the image. 88
**Figure 8-3:** Processed image planes from a spectrum-image of a beta cell showing carbon, nitrogen, and oxygen without corrected beam current drift artifacts. The planes nitrogen/carbon and nitrogen/carbon show this artifact corrected by ratioing the nitrogen and oxygen planes to a plane of a major constituent (carbon). Notice the increase in noise in the corrected planes where there is large difference in beam current. The analysis method was linear least-squares with energy-drift corrections and spatial drift corrections. 89
**Figure 8-4:** Oxygen, Iron, and Carbon image planes from a spectrum-image of Ferritin molecules. 90
**Figure 8-5:** Processed carbon plane from a spectrum-image of a beta cell. The data has been smoothed spatial and plotted as a topographical map. independent dimensions are spatial coordinates, the dependent axis is absolute mass. The analysis method was linear least-squares. 91

# Abstract

Electron energy-loss spectroscopy (EELS) is a powerful technique that is capable of providing a wide variety of information; including elemental quantification, density-of-states and occupancy, bond lengths, angle, energy, and character, radial distribution functions, thickness, and dielectric information. It is perhaps most useful when performed in an electron microscope where the information in the spectrum is confined to the probe dimensions, allowing characterization of areas less than a nanometer squared. Recent improvements in EELS spectrometer technology allow collection efficiencies of hundreds of times more than was previously possible; in some cases the efficiency is close to unity.

Some laboratories have combined the acquisition of EELS spectra with computer steering of the electron beam to produce energy-loss maps. The technique of "on-the-fly-processing" is used to collect a spectrum, calculate the mass or concentration of one or more elements, save the latter data, steer the beam to a new location and repeat the process. An important limitation of this method is that only simple processing can be performed without extending the image acquisition time.

This disadvantage is alleviated using *spectrum-imaging*. This technique collects of all the data and stores it for later processing. This allows not only the data in each spectrum to be analyzed using time-consuming methods, but also permits the spatial statistics of the collective energy-loss spectra to be exploited.

This thesis contains discussion on theory, implementation, and processing of EELS spectrum-images along with processed examples.

# Chapter 1
# Introduction

In the most simple of terms, a spectrum-image is data structure with higher dimensionality than what is normally considered an image. In its most common form a spectrum-image is similar to a normal image, but it contains an entire spectrum at each pixel whereas an image plane has only a single value. This paper is concerned with spectrum-images acquired using an electron microscope and x-ray and energy-loss spectrometers, although the techniques are applicable to other instrumentation.

Spectrum-imaging is a term first published in (Jeanguillaume.., 1988) but the technique has been practiced for somewhat longer. Astronomers have been collecting x-ray and radio spectrum-images of the heavens for many years (Seeds,1984). Several workers have performed rudimentary spectrum-imaging in the electron microscope (EM) by saving a few channels of x-ray or EELS spectra at each pixel of a small image. The latter is fundamentally different from what the author has investigated — storage of available data from an imaging experiment.

Efforts of the author have been concentrated on storing, and later processing, entire 1024 channel EELS and EDS spectra, obtained with parallel recording detectors, and their associated dark field and probe current signals at each pixel in a spectrum-image. The resulting data can be several hundred megabytes. This form of spectrum-imaging differs fundamentally from only saving a few pre-chosen channels at each pixel.

Saving all the data from an imaging experiment means that less needs to be known about the nature of the data prior to collection. It is not necessary to know ahead of time what elements are to be imaged or what parameters are to

be used for processing. When all the data is saved, complex and time consuming processing can be performed without extending data acquisition times. Data can be processed multiple times and the effectiveness of different techniques on the same data can be compared. Problems and artifacts unanticipated prior to data collection can be corrected. Because processing time and acquisition time are not related, the electron dosage to the specimen can be tailored solely according to the desired statistics and acquisition instrument limitations.

Spectrum-imaging of this magnitude was not performed previously because of limitations in computer technology. Only recently have storage devices become large enough and inexpensive enough for routine collection of even moderate-sized spectrum-images of 32 megabytes. Recent improvements in processing speed are also important. Additionally, EELS spectrum-imaging without the use of recently available parallel EELS spectrometers would not be generally useful because of poor signal collection efficiency.

The aim of this paper is to describe spectrum-imaging techniques, what EELS signals are useful to image, and what types of experiments are possible using this technique. Brief mention is made of x-ray spectrum-imaging. Chapter two is a short introduction to EELS theory necessary to understand the later coverage of EELS spectrum-image signals is provided. Many parallel EELS techniques were developed by the author and presented in chapter three along with some commentary on the strengths and weaknesses of currently available parallel EELS spectrometer technology. Chapter four discusses concepts of spectrum-imaging, and chapter five contains presently used and potential analysis techniques. Chapters six and seven contain a short description of the hardware and software created for this thesis. The results of some of the experiments performed with this method are shown in chapter nine.

# Chapter 2
# Electron Energy-Loss Spectroscopy

An electron energy-loss spectrum is a histogram of the inelastic scattering distribution of beam electrons through a solid and is plotted as electrons per channel versus energy-loss. The inelastic cross section for electron scattering is obtained directly from a plural scattering corrected EELS spectrum. This cross section is a complete description of the dielectric response of the sample.

There are two forms of EELS collection methods. Reflection EELS (REELS) involves scattering the electron beam at glancing angles as pictured in figure 2-1. The beam voltage is generally less than a few keV to keep the penetration depth low and the information within the REELS spectrum is confined to the first few atomic layers of the surface. The dielectric information obtained from this spectrum is generally not useful for determining properties of the bulk. However, the dielectric response of surfaces is important and the information that can be gathered from this techinique is useful for a variety of materials. REELS will not be discussed further here but the majority of the theory covered in this section does apply to REELS. A good review of the subject is found in (Ibach..,1982).

Tranmission EELS involves passing beam electrons through a thin specimen and observing the probability of inelastic collisions at beam energy losses from zero up to 5 keV, sometimes higher (see figure 2-2). The scattering angles of the examined portion of the beam are limited by an aperture in the diffraction plane of the EM or with an aperture at the EELS spectrometer. A significant advantage of transmission EELS is that the spectrum contains information only from within the radius of the beam. Some machines are capable of producing beam diameters smaller than a nanometer.

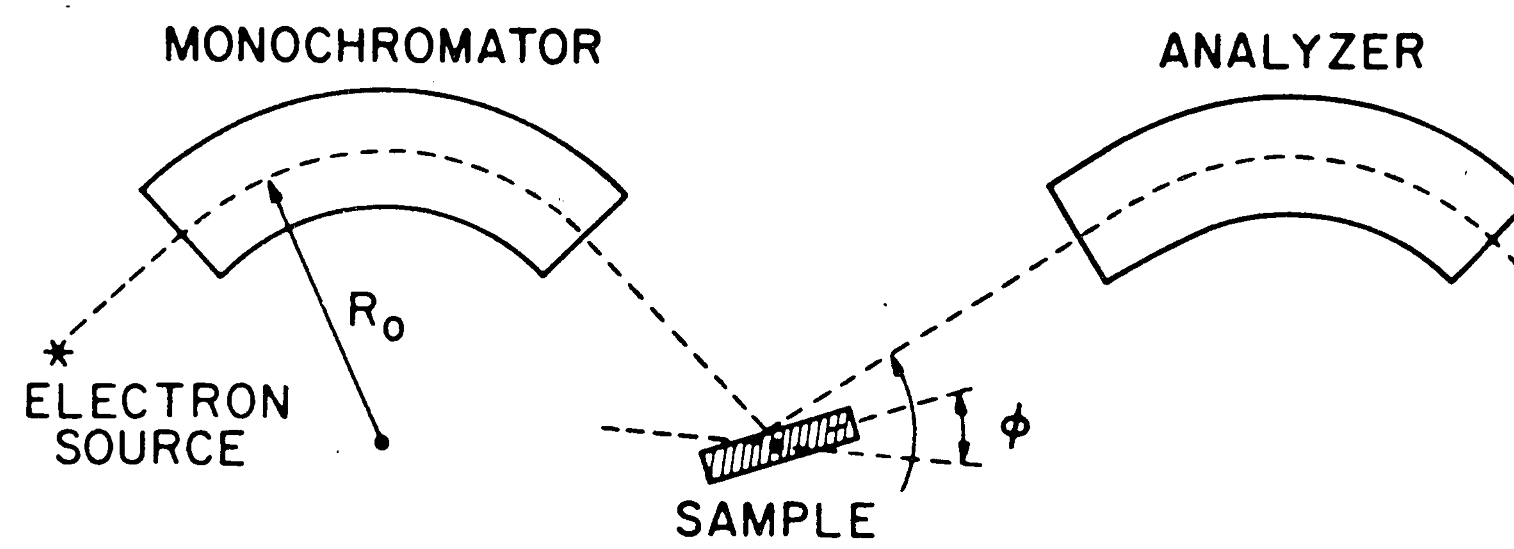


**Figure 2-1:** Schematic diagram of a REELS experiment. Electrons pass from the source through the monochromator, strike the sample, and the energy spectrum of the scattered electrons is probed by a second monochromator. (Ibach..,1982)

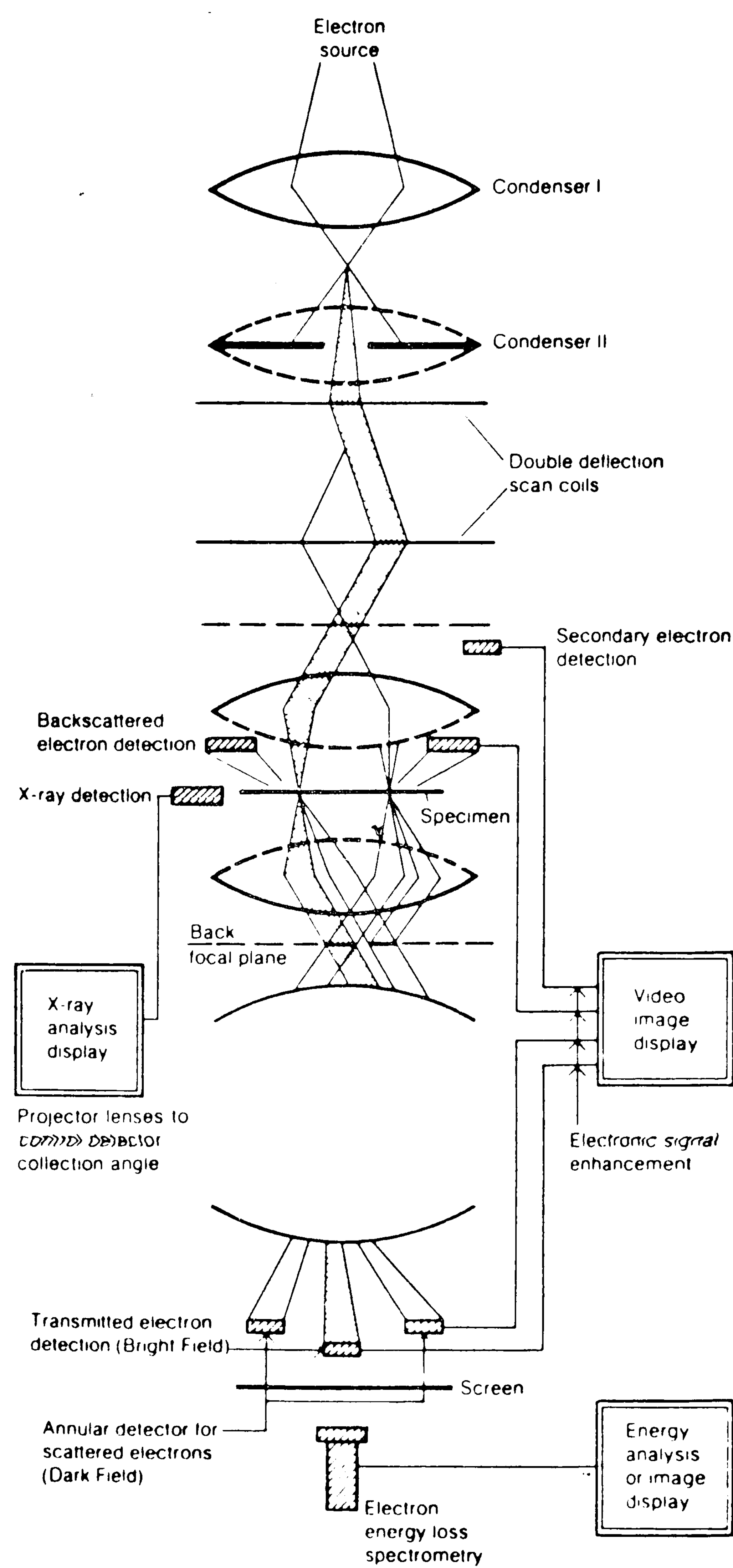


**Figure 2-2:** Schematic view of a TEM EELS configuration (Williams,1987)

When the electrons reach the energy-loss spectrometer they are focused and passed through a magnetic prism which disperses the electrons spatially as a function of energy (or energy loss). A serial EELS spectrometer has a slit that can select what portion of the dispersion, and hence what energy loss, is collected. The slit is moved along the dispersion and electrons are counted at various energy losses giving the EELS spectrum (see figure 2-3). This technique wastes the majority of the signal as the slit generally allows only 1-5 eV of electrons into the counter at a time, and a spectrum generally consists of hundreds or thousands of eV of energy loss. Recently parallel EELS spectrometers have been commercially produced (Krivanek, 1988) where the energy dispersion is focussed on an array of 1024 elements (see figure 2-4). The parallel recording technique increases collection efficiency for most experiments at least 200 times making EELS a much more viable technique for both chemical and dielectric experiments.

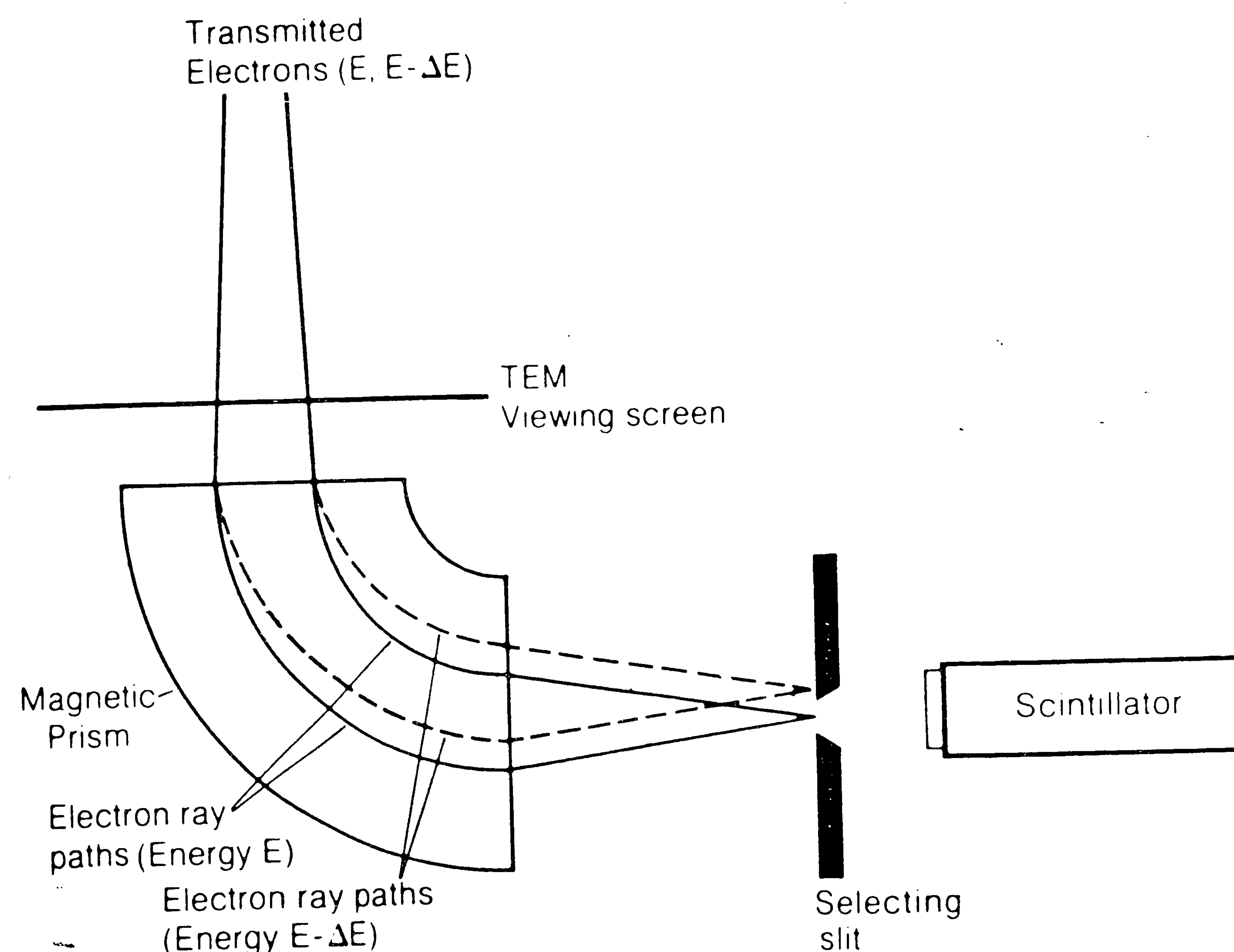


**Figure 2-3:** Typical magnetic serial EELS spectrometer. (Williams,1987)

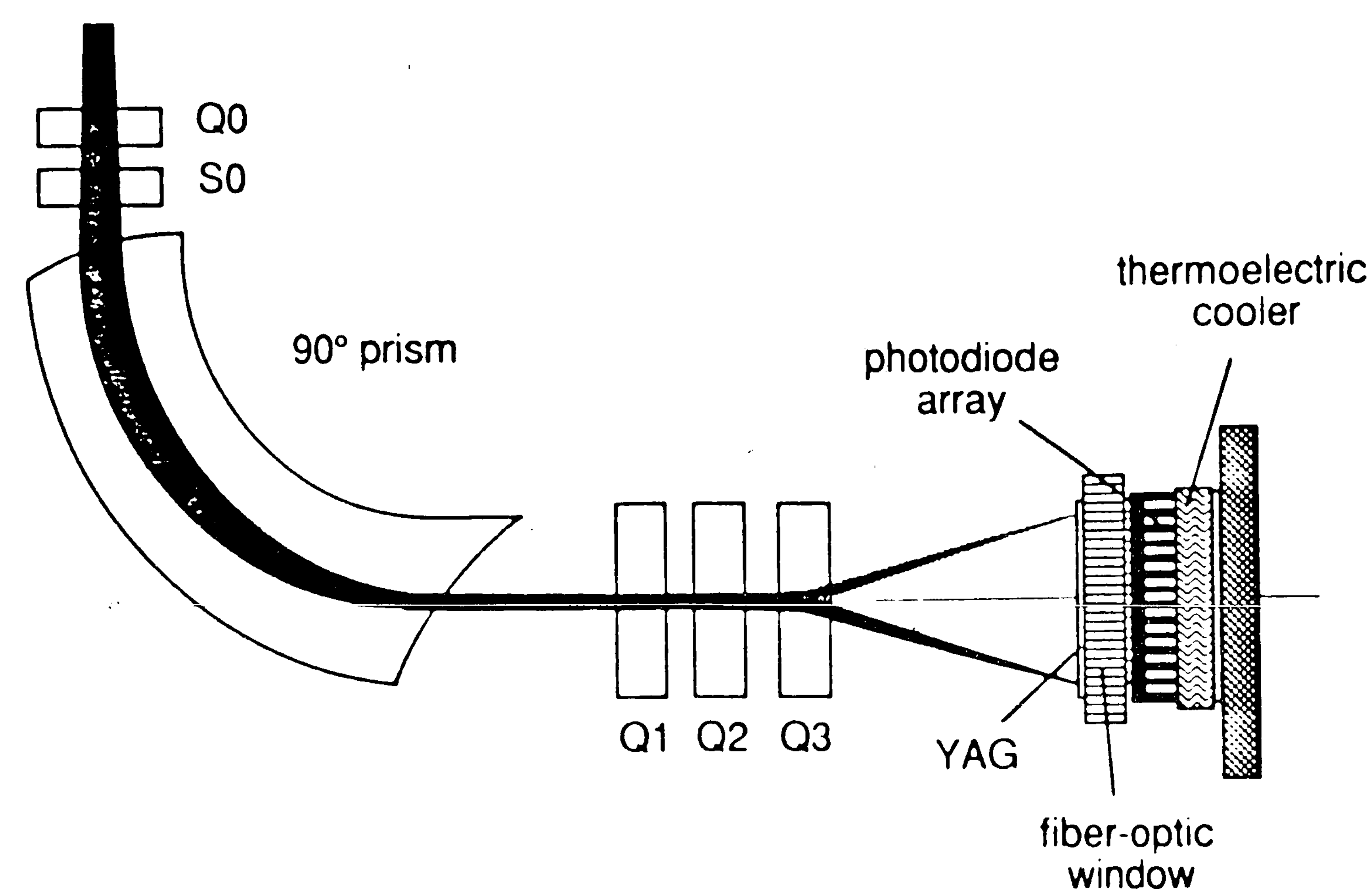


**Figure 2-4:** Schematic diagram of the Gatan parallel-detection EELS spectrometer showing the pre-prism focussing coils, prism, post prism focussing coils and quadrupole lenses, and detector assembly (Krivanek,1988)

Since the advent of PEELS, the most important instrumental limitation in EELS is the energy distribution of the beam. Most EMs use heated tungsten or $LaB_6$ filaments that produce electrons with an energy differential of greater than 1 eV. A few instruments incorporate cold field emission guns that produce energy spreads of 0.25 eV (see (Williams,1987) for details). Examination of many phenomena require higher energy resolution. Some laboratories have used energy filters to monochromate the beam at the expense of beam current, for example (Geiger,1981). There are some fundemental limitations to the minimum energy spread attainable after focussing of the beam (Boersch..,1962).

## 2.1 The Energy-Loss Spectrum

A typical energy loss spectrum is shown in figure 2-5. The first peak in the spectrum is called the "zero-loss." This peak represents electrons that passed through the specimen with no energy loss, or losses smaller that the energy width of the beam. For most instruments this includes all forward scattered elastic collisions, phonon interactions, and electrons passing through the sample unscattered except for a phase change.

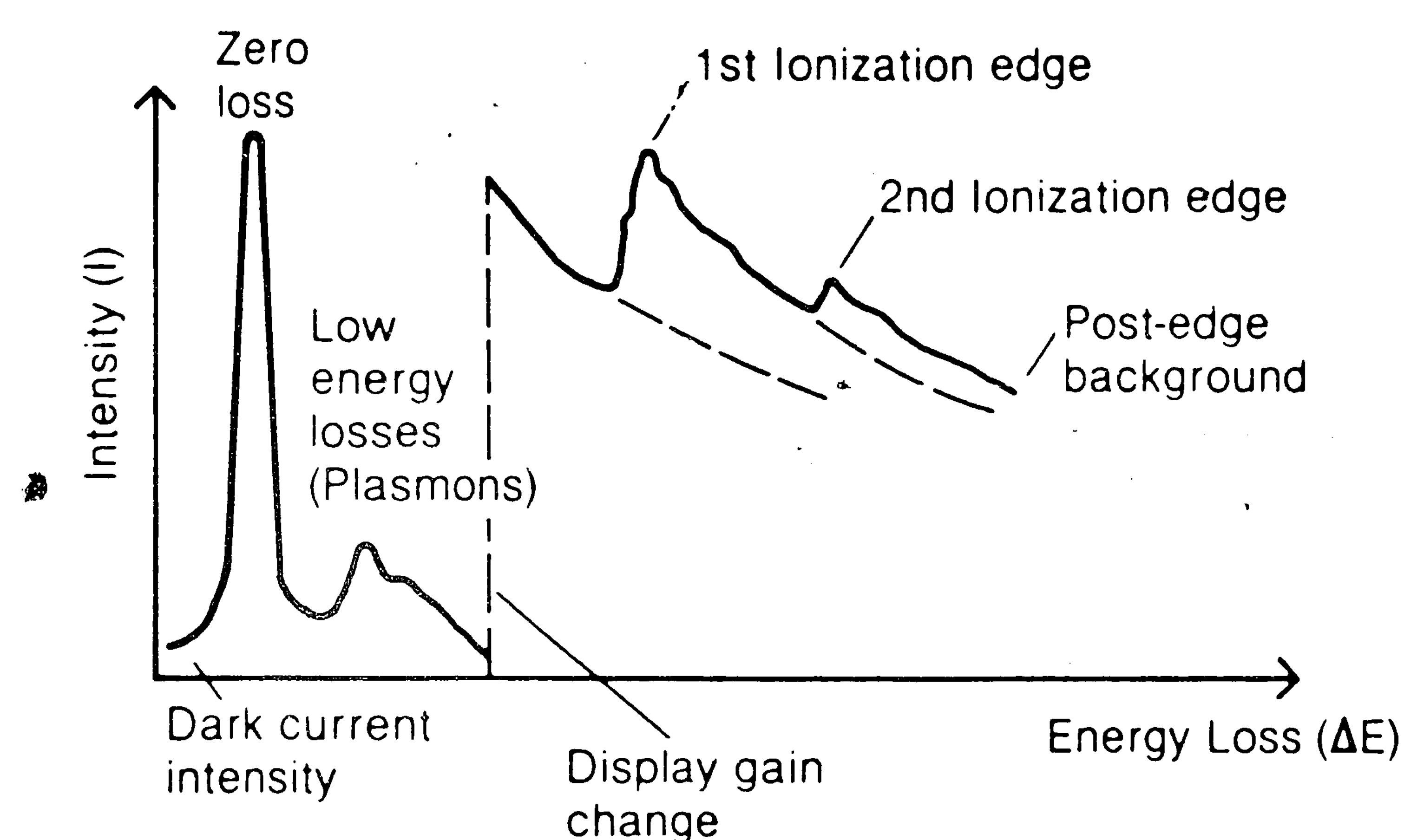


**Figure 2-5:** Typical EELS spectrum. (Williams, 1987)

The next peaks are termed "plasmon" peaks and represent collective oscillations of outer-shell electrons. In most thin specimens the plasmon peaks are not visible beyond 75 eV.

The features following the plasmons represent inner-shell scattering and are termed core-loss edges. Their intensity rises rapidly at the ionization threshold and decreases slowly with increasing energy loss. The energy-loss coordinate of the edge is approximately the binding energy of the appropriate atomic shell, and hence EELS can be used to indicate which elements occur in a specimen. Superimposed upon the exponentially decreasing tail of an edge are often more edges. The area underneath the edge minus the background can be used to determine the absolute or relative composition of that element.

Plasmon peaks and core-loss edges possess a fine structure that reflect the crystallographic and energy-band structure of the specimen. In many EMs the energy spread of the probe electrons is too large to take advantage of this information. Analysis of crystallographic structure is performed through Energy-Loss Near Edge Structure (ELNES) or Extended Energy-Loss Fine Structure (EXELFS) that generate bond distances. A variety of other methods can be used for examining density of states, occupancy, bond energies, etc.

If the specimen is sufficiently thin then the features in the EELS spectrum each correspond to a single excitation process. However, as the thickness approaches that of the inelastic mean free path of the beam electron in the material, there is a resonable probability that the electron will be scattered more than once. This is termed plural scattering and its effects must be removed for reasonable accuracy with most quantitative techniques. At 100 keV, the mean free path (λ) of most elements is between 50 nm and 175 nm. Techniques for plural scattering removal include the Fourier-ratio and Fourier-log methods (discussed in (Egerton,1986)) and more recently MLS (Multiple Least Squares) methods (Shuman..,1987) (Leapman.., 1988).

As the thickness approaches 10λ multiple scattering blurs the core-loss edges in the spectra. Multiple scattering represents multiple core-loss excitations from a single incident electron; whereas plural scattering is when the incident electron excites one or more plasmons in addition to exciting a core-loss transition or another plasmon.

## 2.2 Electron Scattering

In transmission EELS, electrons are accelerated to energies large enough to transmit them through thin specimens. The transmitted electrons interact with the atoms in the specimen. If the energy or direction of an electron is altered it is termed as "scattered." Electrons that are not scattered exhibit only a phase change from passing through the specimen. Electron scattering is divided into two broad catagories; (1) elastic scattering denoting virtually no exchange of energy, and (2) inelastic scattering indicating that there is appreciable energy transmitted from the incident electron to the specimen.

Elastic scattering is a Coulomb interaction between the incident electron and the atomic nucleus. There is little energy transmitted to the specimen in an elasic collision because the mass difference between the beam electron and the atomic nucleus is very large. This type of scattering occurs when the incident electron passes close to the high concentration of charge from the nucleus of the atom. The field from the nucleus can deflect the incident electron through high angles, often termed Rutherford scattering. If the scattering angle is greater that 90 degrees the electron is regarded as "backscattered." Although this is still termed elastic, a backscattered electron can deliver several eV to the target nucleus.

Most incident electrons do not travel close enough to the nucleus to be scattered at large angles. The field of the nucleus falls off according to an inverse-square law, but the field is further weakened farther out due to charge screening from atomic core electrons. The majority of high energy electrons are scattered only tens or hundreds of milliradians.

With truly amorphous specimens (actually only degenerate gases) elastic scattering is a continuous distribution as a function of scattering angle. In crystalline specimens the wave nature of the electron interferes with the

periodic spacing of atoms and changes the continuous distribution of scattering into one that is sharply peaked at angles characteristic of the atomic spacing. This is called "diffraction."

Inelastic scattering is a result of a Coulomb interaction between the incident electron and an atomic electron. One can think of inelastic scattering as an excitation of an atomic electron into a Bohr orbit of high quantum number (figure 2-6) or as a band transition (figure 2-7).

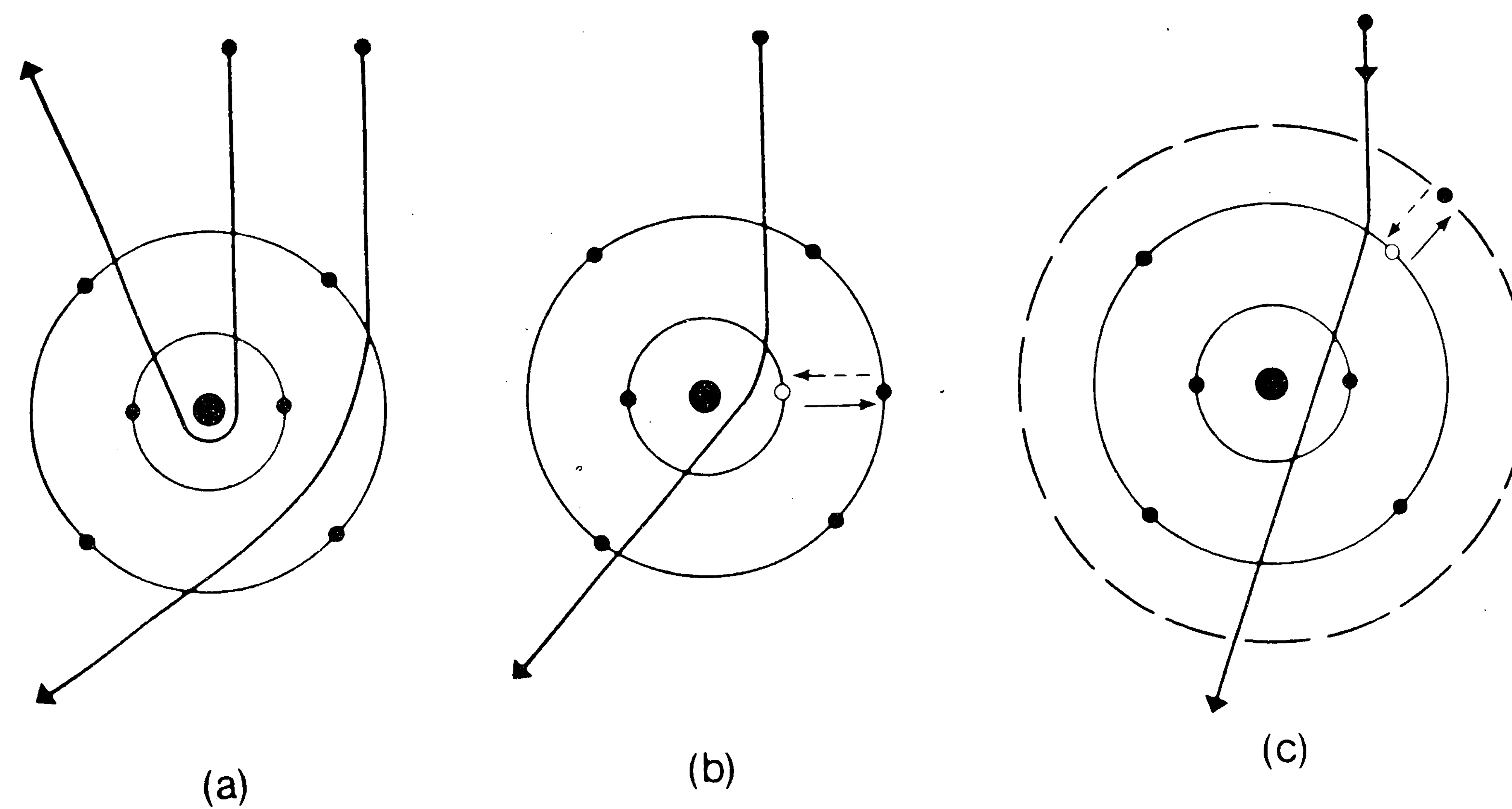


**Figure 2-6:** A classical (particle) view of electron scattering by a single atom. (carbon) (a) Elastic scattering is caused by Coulomb attraction of the nucleus. Inelastic scattering results from Coulomb repulsion by (b) inner- or (c) outer-shell atomic electrons, which are excited to a higher energy state. The reverse transitions are shown by broken arrows. (Egerton,1986)

Inner-shell electrons typically have energies of hundreds or thousands of eV below the Fermi level of the solid. A core electron can only make an upward transition if there is an empty state to accommodate it. Typically the atom will only have unoccupied states above the Fermi level and so the atomic electron can make an upward transition only if it receives an amount of energy greater than its original binding energy. Total energy is conserved at each scattering

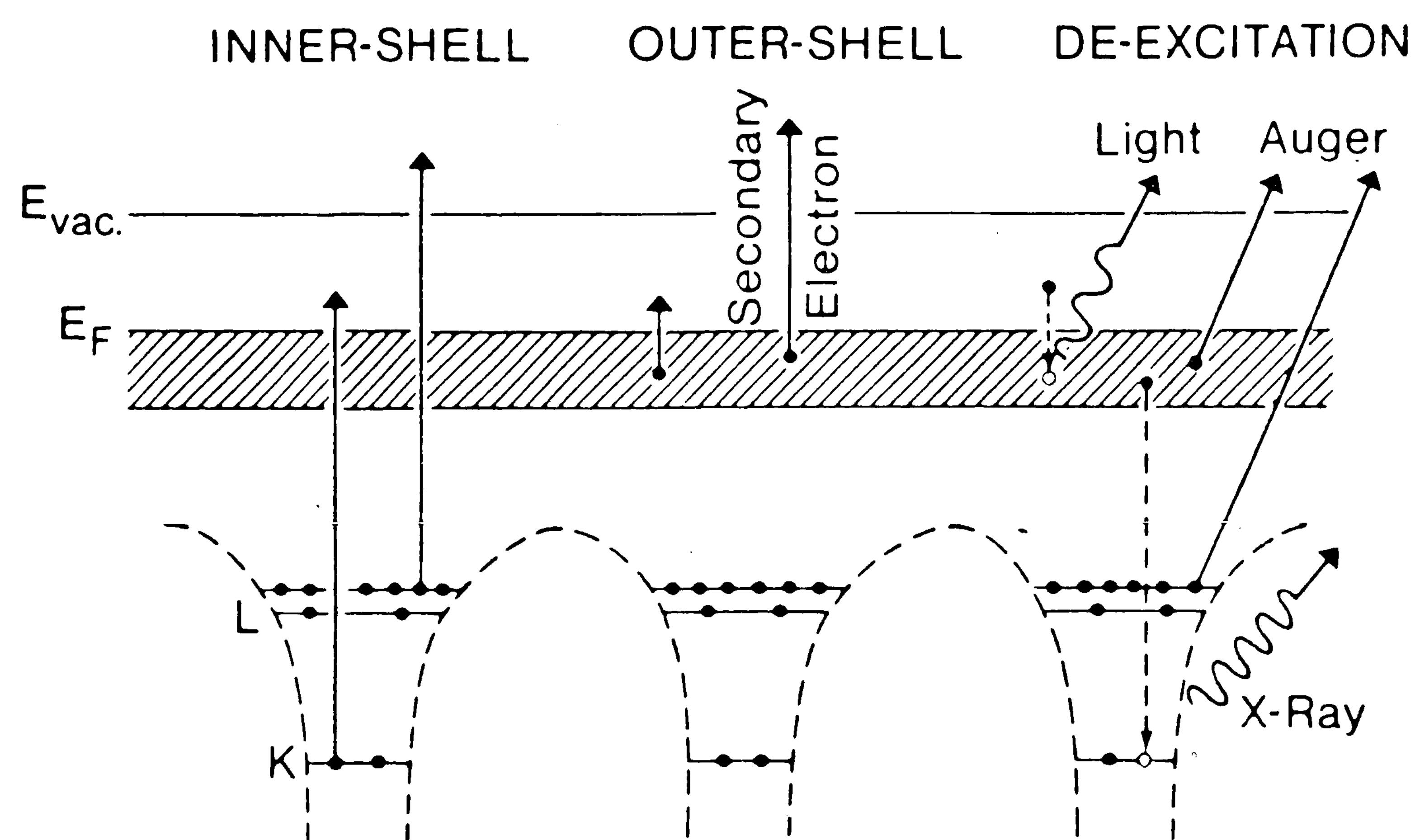


**Figure 2-7:** Energy-level diagram of a solid, including K- and L-shell core levels and a valance band of delocalized states (shaded); $E_F$ is the Fermi level and $E_{vac}$ the vacuum level. The primary processes of inner- and outer-shell excitation are shown on the left, secondary processes of photon and electron emission on the right. (Egerton,1986)

event because there is only one incident electron within the solid at a time for even very high current beams. The incident electron loses the energy given to the core electron and is thus inelastically scattered. The incident electrons are scattered on the order of 5-20 mrad at 100 keV. After an inelastic scattering event the target atom is left excited and quickly loses its energy through one of several de-excitation processes. These include characteristic x-rays that can be used for x-ray quantitation, Auger electrons (kinetic energy donated to another atomic electron), light, and heat.

Outer-shell electrons can be excited in two ways; as a single electron excitation or as a plasmon scattering.

In semiconductors and insulators, an incident electron can excite a single outer-shell electron from the valence band into the conduction band or to an empty state within the energy gap. In a metal, a single electron excitation

causes an outer shell electron to go to a higher state within the conduction band. In either case if the final state is above the vacuum level the excited electron may leave the solid as a "secondary electron." Incident electrons exciting a single outer-shell electron are scattered only 1 or 2 mrad.

A plasmon is a collective scattering of outer-shell electrons from multiple atoms within the solid. It is actually a plasma density resonance or a longitudinal traveling wave of valence electron density. This excitation can be treated as a pseudo-particle called a plasmon and its energy is given by $E=\hbar\cdot\omega$ ($\omega$ is the plasmon frequency). For the majority of solids the plasmon energy is between 5 and 30 eV and has a very short lifetime because it is heavily damped by the electrostatic restoring forces of the atomic lattice.

Plasmons are most easily understood when thought about in terms of the "Fermi gas" of electrons that occur in the conduction band of metals. However, they can also be excited in insulators. In a time averaged sense, the energy of the plasmon is distributed over several atoms. From an instantaneous viewpoint that energy can be carried by a single atomic electron. Since the plasmon energy of most solids is greater than its energy gap, plasmons can be excited in virtually all materials. Plasmons excitation is most important in materials that have electrons that behave as free particles however. In a degenerate gas there is no collective response and hence plasmon excitation is not possible. Most materials exhibit some measurable plasmon response. (Schnattschneider,1986)

The majority of plasmons are volume plasmons, or those that are excited within the bulk of the solid. Surface plasmons can be created that are confined to travel along the specimen surface and are important in very thin specimens. Surface plasmons at each surface can couple and complicate dielectric response calculation.

The distribution of different electron scattering mechanisms are shown in figure 2-8 as a function of scattering angle and energy-loss from the interaction.

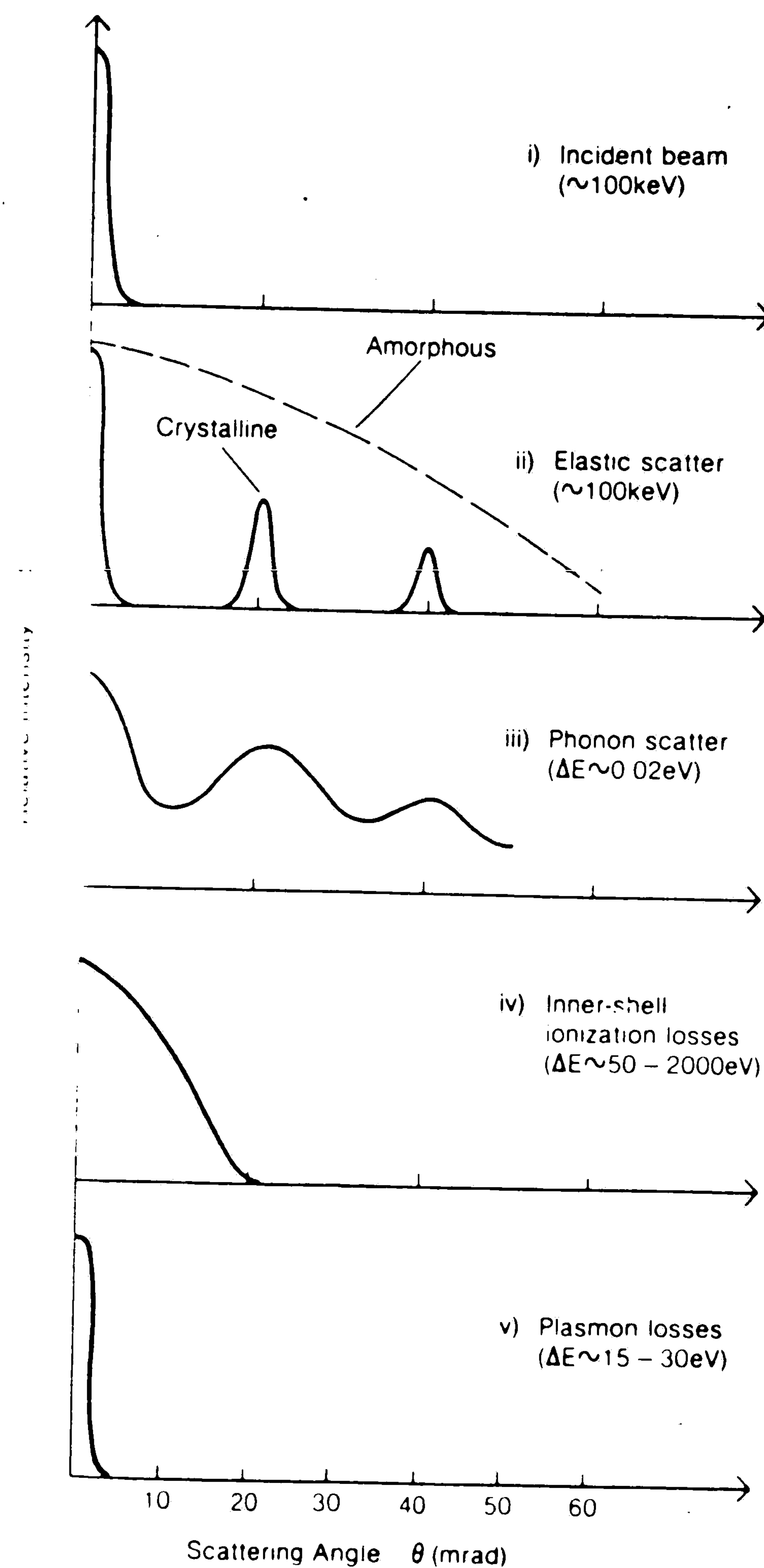


**Figure 2-8:** Angular distribution of various electron scattering phenomena. (Joy..,1979)

## 2.3 Theory and Models

### 2.3.1 Cross sections

Various scattering theories can be used to model the probability of a particular scattering event. In general this probability is a function of scattering angle, and with inelastic scattering it is also a function of energy lost during the interaction. The probability is usually expressed in terms of a cross section, σ, that has units of probability per unit distance traveled through a

particular medium. The functions that are of most interest are the differential cross sections, or $\sigma$ differentiated with respect to one or more of the dependent variables, for example scattering vector (or angle) and energy loss.

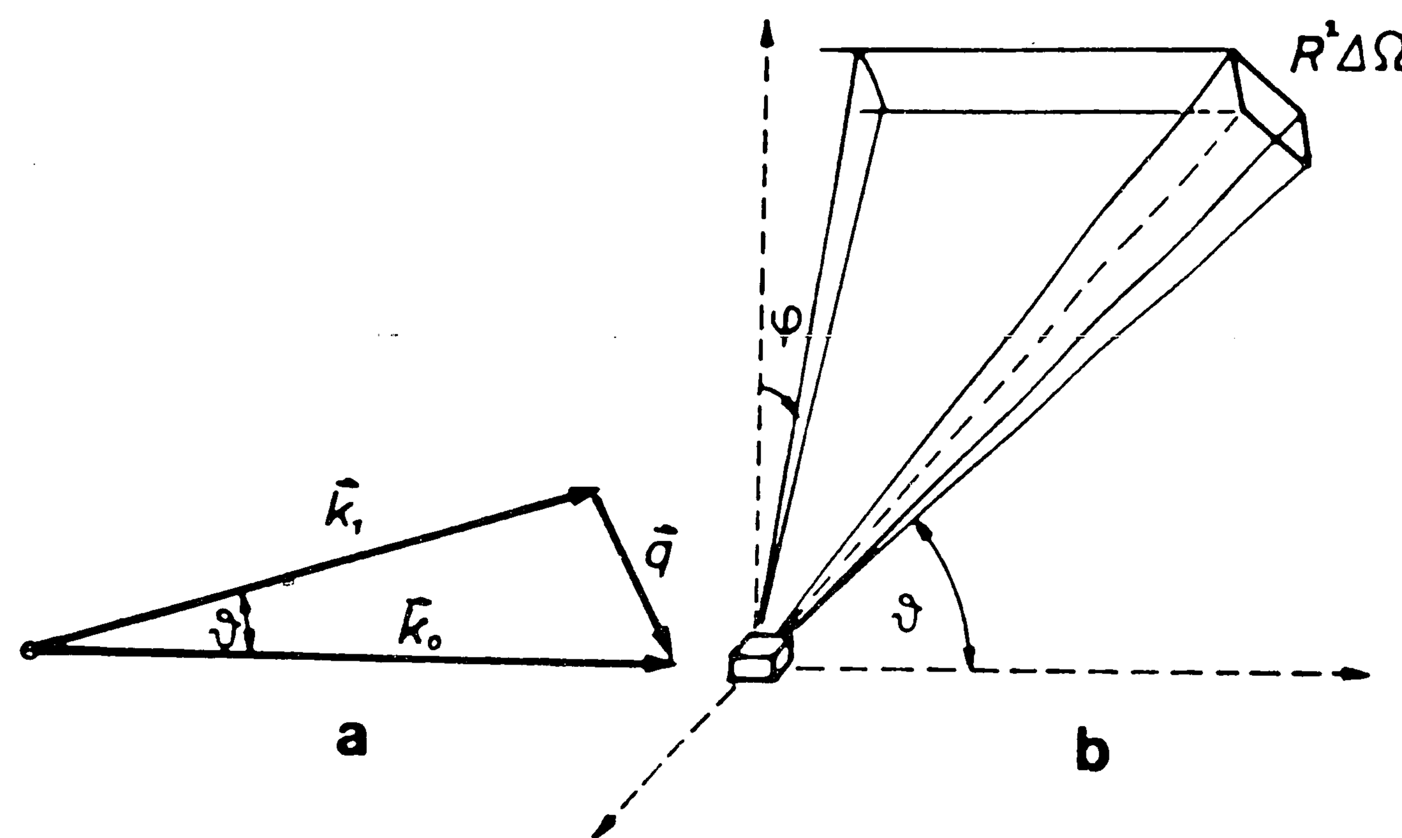


**Figure 2-9:** Scattering planes with wave vectors of incident beam ($\mathbf{k}_0$) and scattered beam ($\mathbf{k}_1$). $\mathbf{q}$ is the wave vector transferred to the target. (Schattschneider,1986)

### 2.3.2 Elastic scattering models

Although inelastic scattering is the primary focus of EELS, elastic interactions are also of interest. Some electrons are scattered both elastically and inelastically. Diffraction redistributes the electron flux within a material and alters the probability of some types of inelastic scattering. In general, elastic scattering modifies the angular distribution of inelastic scattering and this can occasionally be used as the basis of an experiment to reduce surface plasmon effects. The ratio of elastic scattering (including electrons exhibiting only a phase change) to inelastic scattering is important in absolute mass determination for elemental quantification.

Elastic scattering is often explained using classical mechanics because it is both easily understood and works suprisingly well. The first sucessful

attempts at quantifying elastic scattering were by Rutherford involving alpha particles. (Beiser,1987) The Rutherford alpha particle scattering is easily modified to account for elastic electron scattering by switching the charge and mass of the alpha particle for that of the incident electron.

$$\frac{d\sigma}{d\Omega} = \frac{4\gamma^2 Z^2}{a_o{}^2 q^4} \tag{2.1}$$

where $\sigma$ is the cross section, $\Omega$ is the solid angle of scattering, $\gamma$ is a relativistic correction factor, $Z$ is atomic number of the scatterer, $a_o$ is the Bohr radius, and $q$ is the magnitude of the scattering vector.

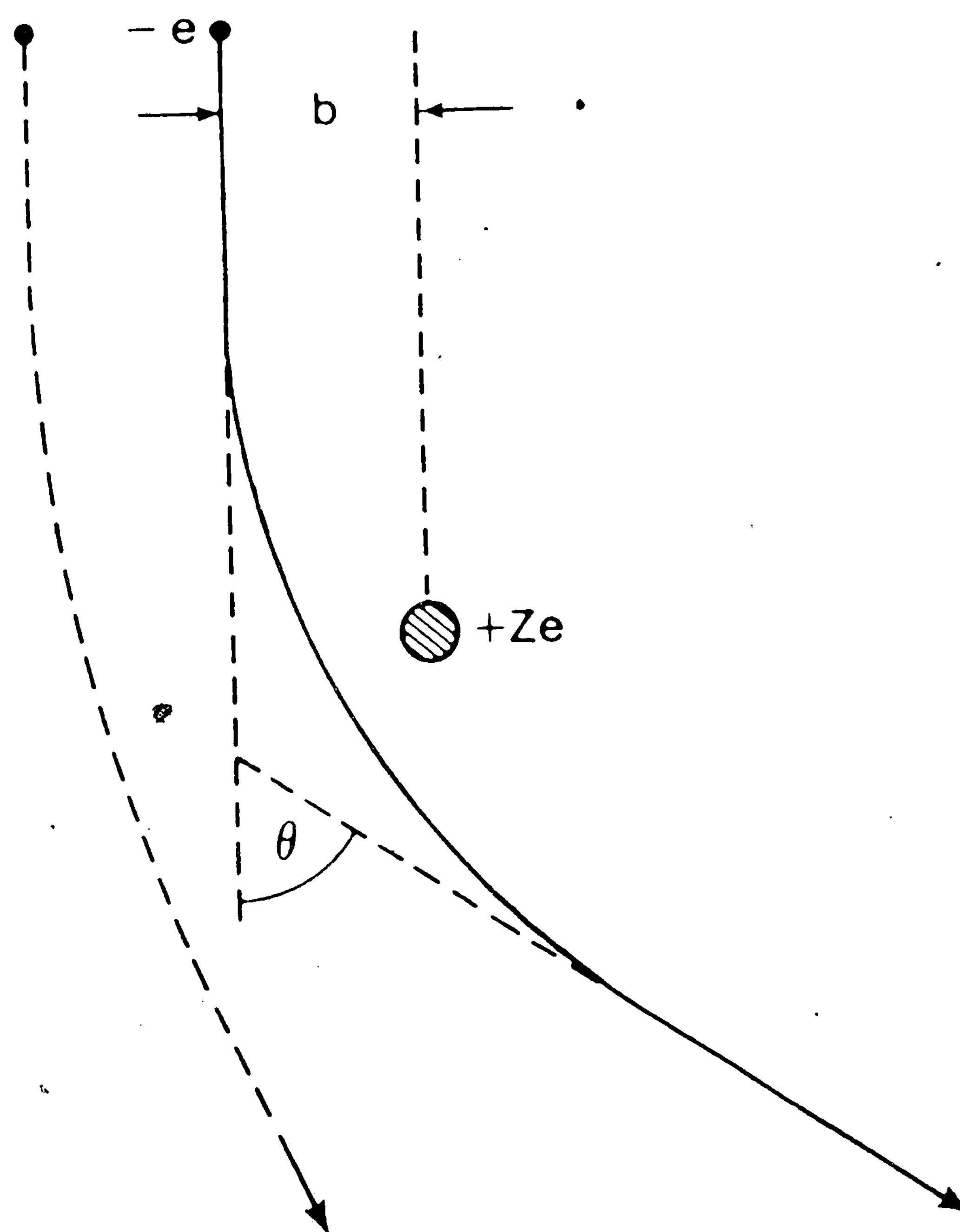


**Figure 2-10:** Rutherford scattering of an electron by the electrostatic field of an atomic nucleus, viewed from a classical perspective. Each scattering angle θ corresponds to a particular impact parameter $b$; as $b$ increases, θ decreases. (Egerton,1986)

The Rutherford equation does not consider charge screening and thus it usually overestimates elastic scattering at small $\vec{q}$. A simple method of incorporating screening is to use a "Wentzel" expression where the nuclear potential drops exponentially as a function of distance from the nucleus. An

example is shown in equation (2.2). At high atomic numbers these equations are no longer accurate and one must turn to quantum mechanics. Better cross sections have been calculated using iterative solutions to Schrodinger's equation in the Hartree-Folk and Hartree-Slater methods, and relativistic effects can be incorporated using the Dirac equation in "Mott" cross sections (Rez..,1984). Despite the sophistication of the latter methods, theoretically generated cross sections are rarely more accurate than 10% of what is seen experimentally (mainly due to bonding effects); sometimes errors exceed 50%. This has limited the accuracy of traditional EELS quantification techniques.

$$\frac{d\sigma}{d\Omega} = \frac{4\gamma^2}{a_o^2}\frac{Z}{q^2+r_o^2} \approx \frac{4\gamma^2 Z^2}{a_o^2 k_o^4}\frac{1}{(\theta^2+\theta_o^2)^2} \tag{2.2}$$

### 2.3.3 Inelastic Scattering

The classical equations for elastic cross sections can be modified to explain trends in inelastic scattering, see the Lenz equation in equation (2.3). The angular dependence of inelastic scattering is more easily seen when it is rearranged as in equation (2.4). A plot of equations for elastic and inelastic scattering is shown in figure 2-11.

$$\frac{d\sigma}{d\Omega} = \frac{4\gamma^2 Z}{a_o^2 q^4}\left[1-\frac{1}{(1+q^2 r_o^2)^2}\right] \tag{2.3}$$

where $\theta_o$ is a constant that is sometimes the *cut-off* angle for inelastic scattering.

$$\frac{d\sigma}{d\Omega} = \frac{4\gamma^2 Z}{a_o^2 q^4}\frac{1}{(\theta^2+\overline{\theta}_E^2)^2}\left[1-\left[1+\frac{\overline{\theta}_E^2}{\theta_o^2}+\frac{\theta^2}{\theta_o^2}\right]\right] \tag{2.4}$$

where $q^2 \approx k_o^2(\theta^2+\overline{\theta}_E^2)$ for small $\theta$, where $\theta$ is the scattering angle, $\theta_E = E/(\gamma m_o v^2)$, $v$ is the electron velocity and $\overline{\theta}_E$ is the angle of mean energy-

loss.

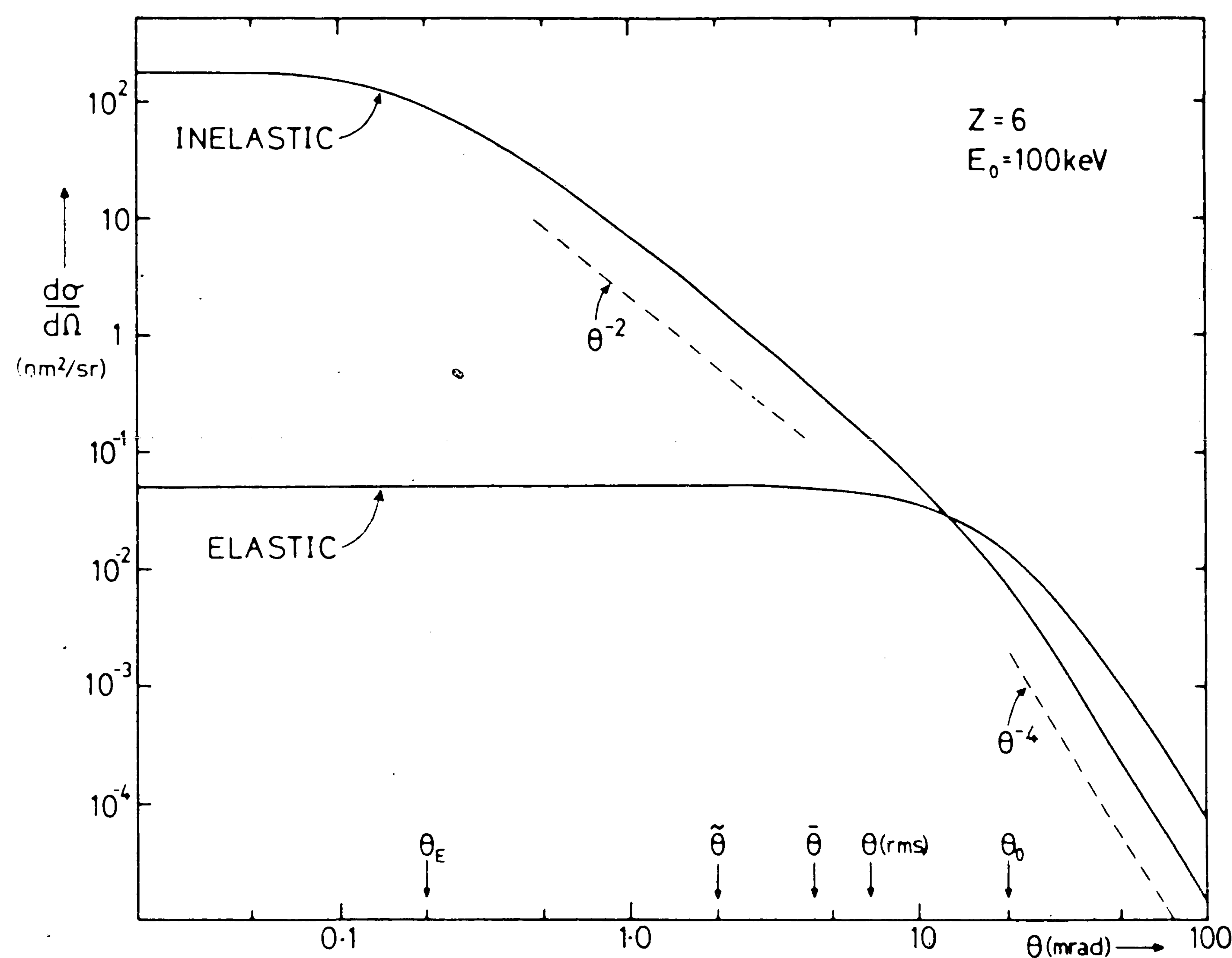


**Figure 2-11:** Angular dependence of differential cross sections for elastic and inelastic scattering of 100 keV electrons from a carbon atom, calculated using the Lenz model. (Langmore..,1973) (Egerton,1986)

Better theoretical cross sections can be calculated using quantum mechanics; the following treatment is often refered to as Bethe theory. Use of the first Born approximation gives a differential cross section in terms of the before and after transition states of each atomic electron in response to an inelastic scattering from an incident electron.

$$\frac{d\sigma_n}{d\Omega} = [\frac{m_o}{2\pi\hbar^2}]^2 \frac{k_1}{k_o} |\int V(r)\Psi_o\Psi_n^* exp(\vec{q}\cdot\vec{r})d\tau|^2 \quad (2.5)$$

where $V(r)$ is the potential causing the transition, $k_1$ is the wave vector of the incident electron after scattering, $\Psi_o$ and $\Psi_n$ are the wave functions of the initial and final states, $m_o$ is the electron mass, $\vec{r}$ is the coordinate vector, and $d\tau$

is the volume element.

The incident electron's potential can be written for non-relativistic electrons as

$$V(r) = \frac{Ze^2}{4\pi\varepsilon_o r} - \frac{1}{4\pi\varepsilon_o}\sum_{j=1}^{Z}\frac{e^2}{|\vec{r}-\vec{r}_j|} \tag{2.6}$$

where $r_j$ is the radius of the $j^{th}$ atomic electron, and $\varepsilon_o$ is the dielectric permittivity of a vacuum.

The cross section can be rewritten in terms of an inelastic form factor, analogous to the more familar elastic form factor used in diffraction. This form factor is a property of the target atom (independent of the beam electron energy) and modifies the Rutherford scattering factor in equation (2.7).

$$\frac{d\sigma_n}{d\Omega} = \frac{4\gamma^2}{a_o{}^2 q^4}\frac{k_1}{k_o}|\varepsilon_n(q)|^2 \tag{2.7}$$

where $\varepsilon_n$ is the inelastic form factor.

$$\varepsilon_n = \langle\Psi_n|\sum_j exp(\vec{q}\cdot\vec{r})|\Psi_o\rangle \tag{2.8}$$

Often the absorption of energy waves in a medium is discussed in terms of a generalized oscillator strength (GOS). The resonance frequency of the oscillator is where it absorbs the greatest amount of energy and appears as a "Gaussian-like" peak in the imaginary portion of a permittivity versus frequency plot as in figure 2-12. The GOS can be related to the inelastic form factor and differential cross section as shown in equation (2.9).

$$f_n(q) = \frac{E_n}{R}\frac{[\varepsilon_n(q)]^2}{q\,a_o{}^2} \tag{2.9}$$

where $f_n(q)$ is the GOS, $E_n$ is the energy-loss of the transition, and $R$ is the Rydberg energy (13.6 eV).

More useful in EELS is the double-differential cross section in equation

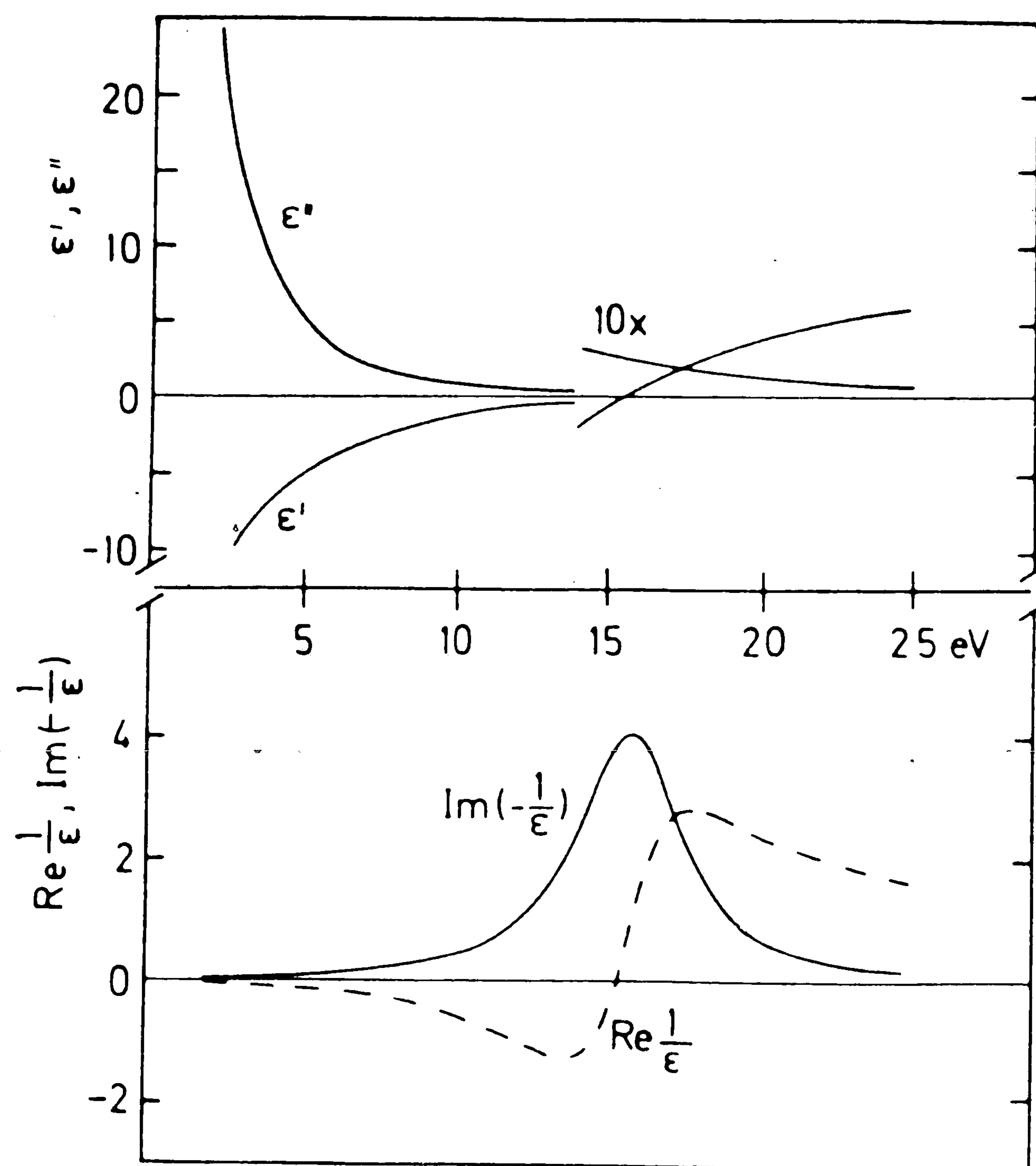


**Figure 2-12:** Real and imaginary parts of the relative permittivity and the energy-loss function $IM\{-1/\varepsilon(\omega)\}$, calculated using a free- electron (jellium) model with $E_p$=15 eV and $\hbar/\tau$ = 4 eV (Raether,1980)

(2.10). The increased complexity of a Bethe generated cross section is shown in figure 2-13.

$$\frac{d^2\sigma}{d\Omega\, dE} = \frac{4\gamma^2 R}{E\, q^4} \frac{k_1}{k_o} \frac{df(q,E)}{dE} \tag{2.10}$$

### 2.3.4 Quantification using EELS

Quantitative analysis using EELS is normally performed using theoretically generated cross sections from programs such as *SIGMAK* and *SIGMAL* by (Egerton,1981). The background underneath an EELS edge (from a plasmon or an edge of lower energy loss) is estimated to fall off as an exponential power of the energy loss (see figure 2-14). The absolute mass of an element in the sample is determined from a ratio of the edge intensity to the total intensity divided by the total cross section.

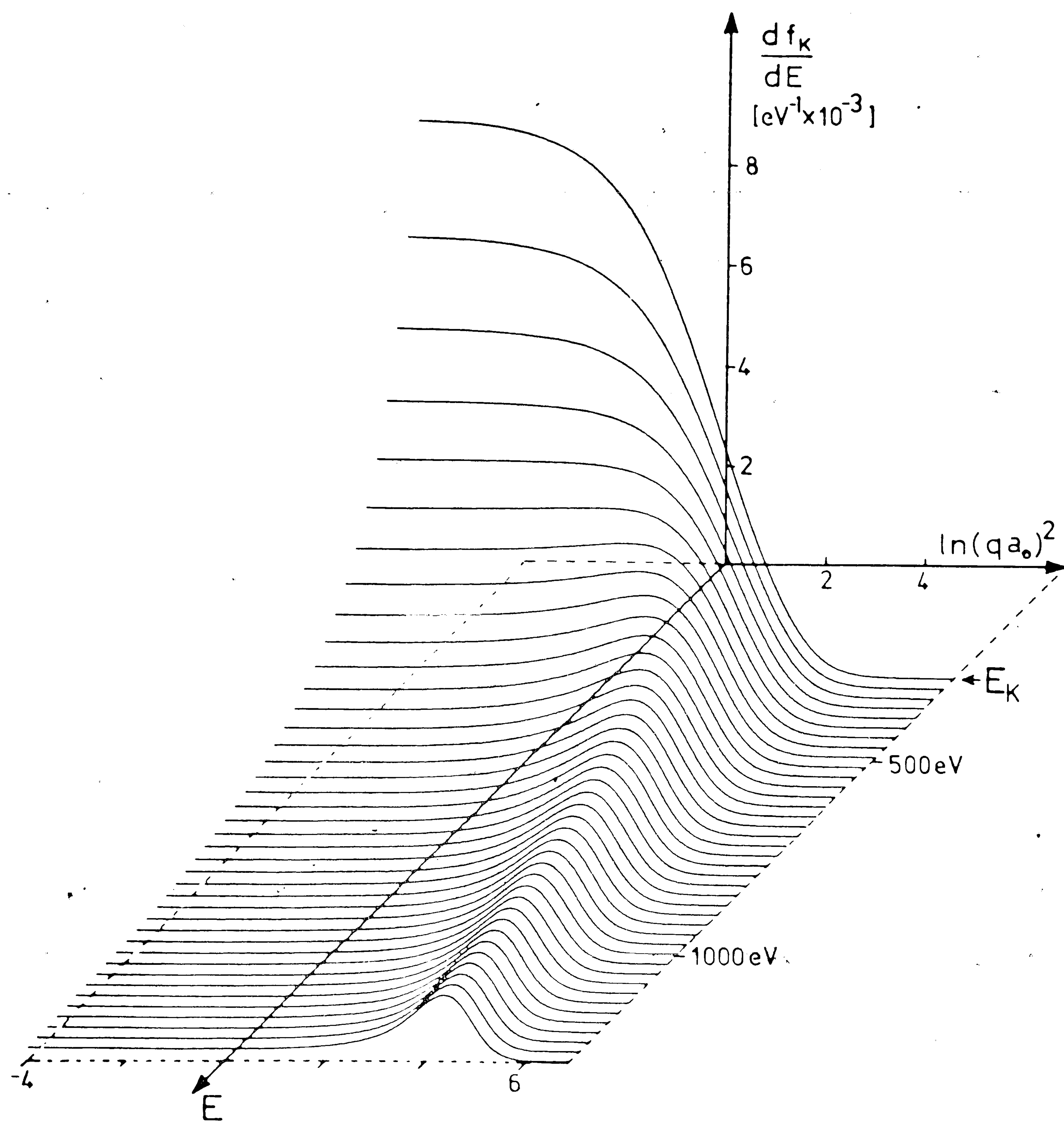


**Figure 2-13:** Bethe surface for K-shell ionization, calculated using a hydrogenic model. The horizontal coordinate is related to scattering angle. (Egerton, 1979)

$$N = \frac{I_{edge}(\beta,\Delta E)}{I_{total} \cdot \sigma(\beta,\Delta E)} \tag{2.11}$$

where $N$ is number of atoms of element $Z$, $I_{edge}$ if the intensity of the edge

corresponding to element Z collected through scattering semi-angle β and integrated from energy loss $E_A$ to $\Delta E$, and $E_A$ is the energy loss of edge $A$.

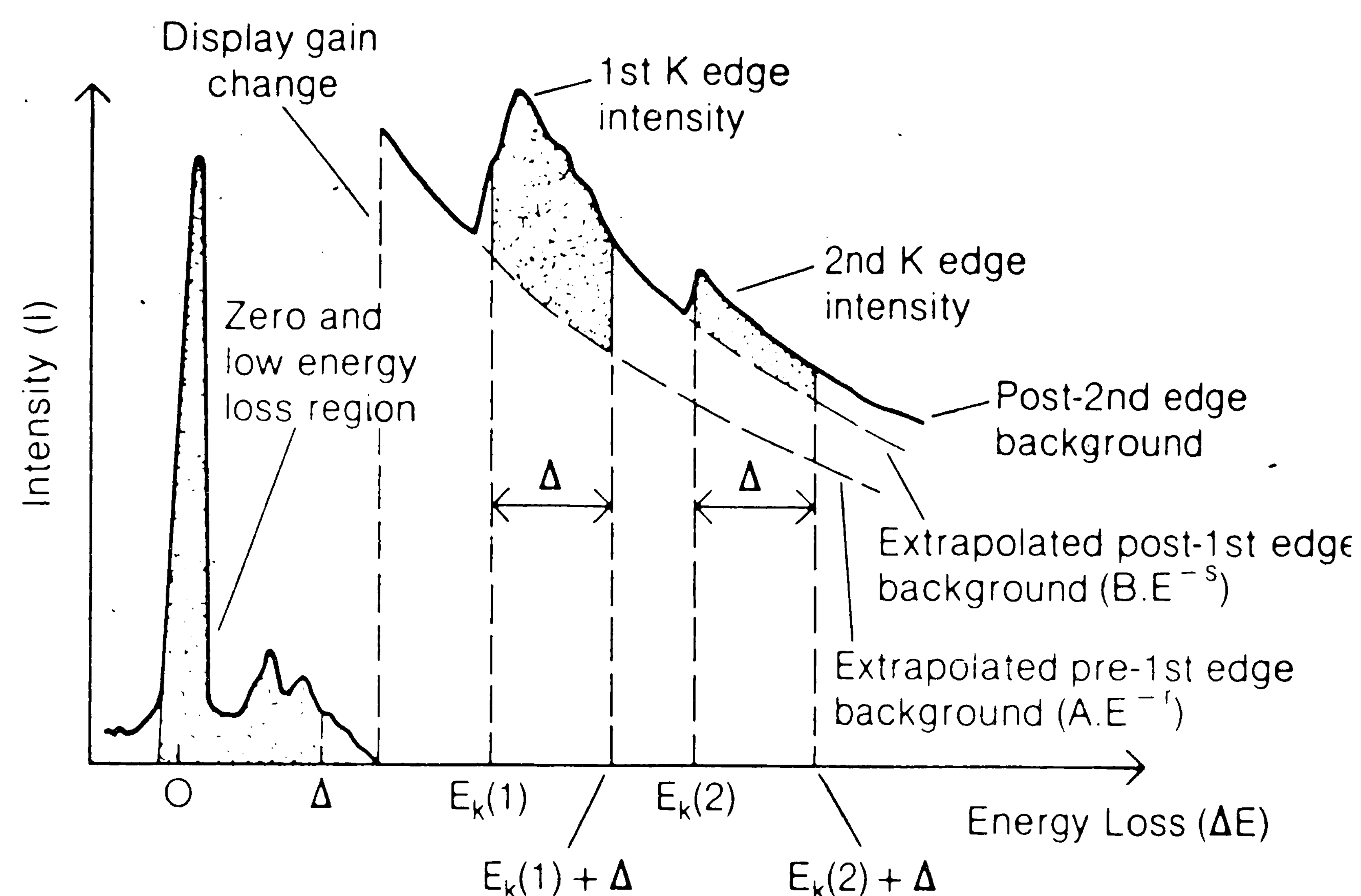


**Figure 2-14:** Regions in an EELS spectrum useful for quantification of more than one edge. (Williams, 1987)

Quantification of the mass of two or more elements relative to each other can be found according:

$$\frac{N_x}{N_y} = \frac{I_x}{I_y} \cdot \frac{\sigma_y}{\sigma_x} \tag{2.12}$$

where $N_i$ is the number of atoms of element $i$, $I_i$ is the intensity of edge $i$ (without background), and $\sigma_i$ is the inelastic ionization cross section of edge $i$.

Theoretically generated cross sections are usually based upon free atoms and are inaccurate mainly because they fail to consider bonding effects. Errors in the theoretically generated cross sections are typically as large as 30%, dramatically reducing the accuracy of this type of quantification. Recently

multiple least-squares fitting (MLS) techniques have been used to bypass the use of cross sections through fitting of reference spectra to an unknown spectrum. Expressed differently, the relative cross sections for elements in the unknown are calculated by fitting reference spectra to the unknown spectra. This technique can dramatically increase the sensitivity and accuracy of EELS. (Leapman..,1988).

### 2.3.5 Correlation of dielectric response to cross sections

Bethe theory is useful for describing inelastic scattering with inner-shell electrons, but chemical bonding significantly modifies the wave functions of the outer-shell electrons resulting in inaccurate theoretically generated cross sections. A better method of describing the interaction of a sample with an incident energy wave is through the use of the dielectric response function.

A "jellium" type model can be used to calculate the displacement of the electron cloud center from the nucleus in electronic polarization, and the displacement of the nucleus from its equilibrium position in ionic polarization. This displacement **x** gives rise to a polarization:

$$\mathbf{P} = -e \cdot n \cdot \mathbf{x} = \varepsilon \cdot \chi \cdot \mathbf{E} \qquad (2.13)$$

where **P** is the polarization vector, **E** is the electric field induced on the polarized atom, $e$ is the elementary charge, $n$ is the volume density of electrons within the atomic radius, $\chi$ is the electronic susceptibility, **x** is the shift vector of the electron charge center from the nucleus center in the jellium model.

The dielectric function is then given by:

$$\varepsilon(\omega) = 1 + \chi = \varepsilon_1 + i\varepsilon_2 \qquad (2.14)$$

where $\varepsilon(\omega)$ is the frequency dependent complex dielectric response, $\omega$ is the angular frequency of the excitation source (the incident electron).

$$\varepsilon_1(\omega) = 1 - \frac{\omega_p^2}{\omega^2+\Gamma^2} \tag{2.15}$$

$$\varepsilon_2(\omega) = \frac{\Gamma\,\omega_p^2}{\omega\,(\omega^2+\Gamma^2)} \tag{2.16}$$

where $\Gamma$ is a constant, and the resonant frequency of the jellium oscillator is:

$$\omega_p = \sqrt{\frac{n\,e^2}{\varepsilon_o m}} \tag{2.17}$$

The energy loss function is what is measured in EELS and is defined as:

$$IM\left[\frac{-1}{\varepsilon(\omega,q)}\right] = \frac{\varepsilon_2}{\varepsilon_1^2+\varepsilon_2^2} = \frac{\omega\,\Gamma\,\omega_p^2}{(\omega^2-\omega_p)^2+(\omega\,\Gamma)^2} \tag{2.18}$$

where $q = 0$ for an electromagnetic wave, and $q \approx 0$ for an electron wave. See (Kittel,1986) for details.

When an electron passes through a sample it essentially represents a step function of all frequencies. Thus an incident electron excites the loss mechanism for the entire frequency spectrum. The outer-shell electrons do this through a GOS peaked at the frequency $\omega(p)$, which is equivalent to the excitation of a plasmon of energy $E(p) = \hbar \cdot \omega(p)$. From this simple analysis, the electronic polarization oscillator frequency can be determined by merely measuring the energy-loss position of a plasmon peak.

The dielectric response function can be correlated to the partial differential cross section by combining equations (2.9), (2.10), and (2.18):

$$\frac{\partial^2\sigma}{\partial\Omega\,\partial E} \approx \frac{IM[-1/(\varepsilon(q,\omega))]}{\pi\,a_o m_o v^2 n}\,\frac{1}{\theta^2+\theta_E^2} \tag{2.19}$$

# Chapter 3
# Parallel EELS

The commercial introduction of parallel electron energy loss spectrometers (PEELS) is a revolutionary advance for the EELS researcher. PEELS offers several hundred-fold increases in signal collection efficiency over serial EELS (SEELS) and allows routine solutions to experiments that were previously exceedingly difficult or even impossible using SEELS.

## 3.1 PEELS advantages

### 3.1.1 Core-loss collection efficiency

Core-loss (CL) edges on the threshold of detectability with SEELS may be obtained with much less noise per collection time and thus may be more accurately analyzed with PEELS. Such edges include those from high- energy loss K-shell excitations and those from very low concentration elements.

The PEELS collects a typical spectrum with 100 - 500 times more counts and thus 10 - 23 times less noise per channel per electron dose than a SEELS. Therefore peaks that fall below the noise threshold with SEELS may be considerably above this level in PEELS.

A major disadvantage of EELS in the past has been its insensitivity to high atomic number (Z) elements. Because high energy-loss edges can be obtained with better counting statistics, PEELS quantitation of high Z elements is far more accurate and sensitive.

Many laboratories now perform quantitative core-loss imaging where pixels represent an absolute amount or a concentration of an element or compound. An entire spectrum is acquired and quantitatively analyzed at each pixel. Accuracy for rapidly acquired images with SEELS is compromised by

very low signal-to-noise ratios, often well below unity. This situation is vastly improved with PEELS.

### 3.1.2 Minimizing electron dose

Beam sensitive specimens require that their electron dose be minimized to minimize rapid alteration of bonding and elemental re-distribution from the electron probe. Materials systems exhibit such changes as crystallization of polymers and glasses, graphitization of amorphous carbon, and mass loss of low-Z and volatile elements. Biological systems exhibit destruction of typically fragile bonds and substantial mass loss.

The accuracy of beam sensitive materials is highly dependent on the electron dose per area. The substantial increase in collection efficiency of PEELS over SEELS allows spectra to be taken in fractions of the time necessary for a SEELS spectrum. Since PEELS acquisition times may be very short, successive spectra can be taken and analyzed separately to determine rates of mass loss or bonding changes. Spectra can then be summed for more accurate quantification.

## 3.2 PEELS disadvantages

PEELS allows the researcher to collect EELS spectra faster and with better statistics than was possible with SEELS. However, current PEELS spectrometer technology is not without difficulties — problems such as artifacts, detector limitations, and poor low-dosage sensitivities must be compensated or corrected before its full promise is realized.

### 3.2.1 Artifacts

Detector artifacts in SEELS are limited to a detector persistence that becomes important when the signal intensity of a recently scanned feature greatly exceeds the currently monitored signal. PEELS is not immune to detector persistence, but it can be safely ignored provided a steady-state signal is fixed on the array for at least one integration period prior to the collection of that signal. In any case, it is usually a trivial matter to collect a spectra such that persistence is not a problem in either SEELS or PEELS. Other PEELS artifacts, the time and temperature variant array channel-to-channel gain variations and dark current are not so mundane and require processing to minimize their effect. Removal of these artifacts has inspired new ways of quantifying very small signals and it is clear that considerably more work must be done before quantification of PEELS spectra becomes routine.

### 3.2.2 Detector limitations

Concurrent or successive acquisition of core-loss (CL) and low-loss (LL) spectra is difficult. A PEELS spectrum is actually the sum of one or more readouts (integrations) of the parallel detector to measure signals in excess of the dynamic range of the detector. The minimum integration time of the Gatan PEELS is 12.3 ms. A one nanoamp zero-loss (ZL) from a one electron-volt (eV) wide (energy spread at FWHM) probe and a 0.5 eV per channel dispersion will saturate the array in under 150 μs. If the intensity of the CL signal is optimized so that it uses a significant fraction of the array's dynamic range then the accompanying LL, taken even with the smallest integration time, will most likely saturate the array. Newer models of the Gatan PEELS include an attenuator which steers the dispersion off the detector array quickly to minimize array exposure. Although this is a step in the correct direction,

asymmetries in successively collected spectra with the attenuator suggest that hysteresis with the attenuator's dipole lens compromises signal quality. In addition, the speed of the attenuator is not fast enough for some experiments.

### 3.2.3 Low dosage insensitivity

Some ultra-low dose experiments can not be performed using the Gatan PEELS in a straight-forward manner because of the large minimum integration time. High resolution experiments with doses of $10^4$ - $10^6$ electrons per square nanometer may require dwell times of 1 ms or less. Charge trapping of electrons in the photo-diode detector array limit the sensitivity of an element when it contains less than the current generated by 1000 incident electrons. Additionally, high readout noise effectively masks small signal differentials of less than 100 - 300 incident electrons per channel. Use of correctly biased CCD arrays can correct for the non-linearity of the *detective quantum efficiency* (DQE) for small signals. The placement of an image-intensifier between the scintillator at the detector array could boost the DQE to unity.

Future versions of commercial PEELS units will incorporate charge-coupled devices (CCD's) with higher readout speeds that will eliminate the large minimum integration time problem. In the interim, a high-speed pre-specimen beam blanker seems the most appropriate means for bypassing the large minimum integration time.

## 3.3 PEELS artifacts

Processing methods used in SEELS are often not appropriate for PEELS. These procedures do not account for PEELS artifacts and they are often too insensitive to small signals that can be obtained with good statistics using PEELS.

The term *dark current* denotes the signal that is read from the array even

when there is no illumination incident on the array. The author has chosen to divide this signal into two parts, $S_1[t, t_i, ch, T]$ and $S_2[t_i, ch, T]$ — where $t$ is elapsed time, $t_i$ is the integration time, $ch$ is the channel number, and $T$ is temperature of the array. $S_1$ is due to the persistence of the array (incomplete charge readout) and is not an artifact provided that (1) the signal is steady-state and remained on the array for at least $t_i$ prior to signal collection; (2) the signal in each channel before signal collection did not exceed the signal during collection. The artifact may be unimportant even if these conditions are not met. $S_2$ is mainly due to charge leakage from the array and is a strong function of $t_i$ and $T$. Parameterization of $S_2$ for constant $T$ provides an adequate model for artifact removal from large signals, but acquisition of the signal is more accurate. In addition, large variations of $S_1$ and $S_2$ as functions of $T$ may render such models useless.

With the Gatan 666 spectrometer, the offset of the dark current can be adjusted. This is optimally set so that the minimum dark current in any channel is about 10 counts. The dark noise profile is significantly different between Gatan spectrometers. Each count in a spectrum represents about 30 electrons, and the maximum signal per channel per integration is 16383 counts.

Channel-to-channel gain variations in the detector array are caused by small variations in the efficiency and collection area of each cell of the array. This artifact can be removed accurately by dividing the dark current corrected spectrum by the relative gain function. This function is measured by evenly dispersing a small portion of the zero-loss peak over the entire array and scaling the function so that the smallest channel value is unity. Problems arise with this form of gain function measurement because intensity variations within the zero-loss peak prevent even illumination over the array.

Although the gain function is only weakly related to temperature, it does

**Figure 3-1:** Dark current from a Gatan PEELS spectrometer with no incident electron illumination. Acquisition time is 1 s

vary slightly over a period of several months due to exposure related changes in the scintillator material covering the array. In the Gatan 666 spectrometer it is rare to find a channels efficiency vary in excess of five percent.

Future versions of commercial PEELS are likely to incorporate CCD's that will not exhibit the dark current artifact when biased correctly. However, any parallel detector is apt to channel-to-channel gain variations. This artifact is easily corrected provides the gain function of the active portion of the array is accurately known.

## 3.4 Correcting PEELS artifacts

The most obvious method to correct the raw PEELS spectrum is to acquire a dark current spectrum before the specimen spectrum using identical integration times. The dark current is next subtracted from the specimen spectrum and is divided by the gain function. This method doubles the noise in the processed spectrum, but preserves edge shape and areas and thus spectra

**Figure 3-2:** Channel-to-channel gain variations superimposed upon the uneven illumination of the dispersed zero-loss.

can be processed as normal SEELS spectra. The noise level can be reduced asymptotically to the specimen spectrum noise level by increasing the number of readouts in the dark current spectrum and scaling appropriately.

### 3.4.1 Problems in finding the channel-to-channel gain function

The channel-to-channel gain function for a particular set of spectrometer and microscope operating conditions can be known to a very high accuracy. However, this is not necessarily useful particularly for a 1 dimensional detector array because small changes in the operating conditions can change the gain of a single channel by several percent.

This effect occurs because the energy-loss dispersion is not focussed upon

the entire height ($Y$ direction) of the detector array. Small changes in the spectrometer or microscope conditions change the position of the dispersion on the array in the $Y$ direction. Inhomogeneities in the detector or scintillator material can change the efficiency of a portion of a detector cell. Thus movement of the dispersion over such defects will alter the channel-to-channel gain function.

This condition is quite restrictive. Changing operating conditions such as beam voltage, collection angle of the spectrometer, focussing conditions of the microscope, and any of the lens settings within the spectrometer will cause the dispersion to move along the array. For this reason it is often best to use a method of spectrum analysis or collection that does not require knowledge of the channel-to-channel gain function.

If the spectrometer incorporates a two-dimensional array where the dispersion is focussed over elements in both directions along the array, then this problem can be minimized. The gain function for each cell can be determined and it is then assumed that the cell dimensions are so vanishingly small and that the dispersion will never partially illuminate a cell.

There is a method developed by the author that does not require a change in spectrometer settings between calculation of the gain function and measurement of the spectrum. It uses the computer programmable drift tube voltage offset generator to sweep a spectrum across the array without the use of the spectrometer lenses. The disadvantage of this method is that a dispersion of 0.5 eV per channel or less is required. The procedure is described below.

### 3.4.2 Gain averaging

This method was first used in EELS by (Shuman,1984). It involves shift adding $n$ spectra, each offset in starting energy from the previous spectrum by the amount of the shift, usually equivalent to the energy width of a single channel (the energy dispersion). For large $n$, at least more than 15, channel-to-channel gain artifacts are effectively eliminated. If dark current effects are large then the dark current signal should be removed from each spectrum prior to gain averaging.

This method was found to be excellent in removing artifacts for large $n$; its effectiveness is largely dependent on the size of the gain variations. It is the method of choice for spectra collected with good counting statistics.

### 3.4.3 Difference spectra

The use of difference spectra can greatly enhance the visibility of very small edges without curve fitting. Quantification of difference spectra can be more successful than conventional techniques because the information important to analysis may be weighted more heavily when fitting in differential space. Because the edge shape and area are not preserved, quantitative analysis must be performed by fitting differentiated reference spectra of standards to the unknown difference spectrum. Difficulties occur in selecting the energy window which is dependent on the width of the feature that is to be enhanced. A properly selected energy window will remove the background beneath the edge without the inaccuracies associated with curve fitting. Integration of the differentiated signal with the correct choice of integration constants can restore the normal edge shape and areas.

More significant advantages of difference spectra are realized when it is used to remove PEELS artifacts. A second difference can be used for this

**Figure 3-3:** First difference spectrum showing carbon, nitrogen, and oxygen K edges

purpose when three spectra, $A$, $B$, and $C$, are acquired with an energy shift of the starting channel from the previous spectrum by an energy window. These spectra are combined according to the equation $D = 2B-A-C$ to form the second difference, $D$. The dark current and the channel-to-channel gain fluctuations are effectively removed.

A major disadvantage of the difference spectra approach is that areas and edge shapes are not preserved and thus new deconvolution and fitting software is required to analyze them directly. For second difference spectra it is often more sensible to save the component spectra so they may be combined either for a normal or a first or second difference spectrum. Difference spectra can be

**Figure 3-4:** Second difference spectra of same specimen in figure 3-3 but using different energy windows.

integrated to yield normal spectra with the proper integration constants.

Multiple least squares (MLS) or simplex fitting algorithms can compensate for the difficulties encountered with difference spectra. These techniques rely on reference spectra taken from standards of known compositions that are processed in a fashion identical to the specimen spectrum. The reference spectra are then fitted to the specimen spectrum and the fitting parameters give the relative concentrations.

Removal of plural scattering is difficult and inaccurate using Fourier techniques if the thickness of the specimen is not uniform under the electron probe. An excellent method to deconvolve such spectra bypasses the Fourier

techniques and uses MLS or other fitting of convolved reference spectra. One or more plasmons in the LL are used to mathematically convolve the single-scattering reference spectra for an edge, and are then fitted to that edge along with the unconvolved reference spectrum. Here the parameters from the fit also give the average thickness of the specimen which is useful in absolute quantification. This technique can be applied to both differentiated and normal spectra provided the reference spectra and specimen CL spectra undergo identical processing.

Difficulties in this technique arise when multiple types of bonding occur in different proportions than in the reference spectra. This situation can occur in images, for instance in a system that contains both amorphous and graphitic carbon. Reference spectra must then be taken from different standards each representing, preferably exclusively, a type of bonding for an element, and each convolved with the desired plasmons. The relatively large number of reference spectra that must be fit to the unknown spectra offer many degrees of freedom and require very well chosen fitting weights to prevent apocryphal results. The procedure is discussed more fully later.

# Chapter 4
# Imaging

The term *image plane* used herein refers to a multidimentional representation of data with zero or more independent dimensions and a single dependent dimension. An *image* is composed of one or more equidimensional image planes. The dimensionality, D, of an image or image plane refers to the number of independent dimensions. A typical example of both an image (and also an image plane) is a black-and-white photograph — this is a 2D image possessing three total dimensions, two independent spatial dimensions and one dependent intensity dimension. A color photograph is composed of three such image planes with the dependent dimensions represented by the intensities of cyan, magenta, and yellow (the complements of red, green, and blue).

Images in electron microscopy can become more complicated, such as in the case of a "spectrum-image" (Jeanguillaume..,1988). A typical spectrum-image consists of a spectrum collected for each pixel in two spatial dimensions. Thus there are three independent dimensions, two spatial and one energy, and one dependent dimension of counts.

Spectrum-images can become still more complicated. An example would be a 4D spectrum-image with two independent spatial dimensions, one independent energy-loss dimension, one independent scattering angle dimension, and a dependent counts dimension.

Spectrum-images are usually processed into 2D images for viewing. In the case of an EELS spectrum-image there may be N core-loss edges per pixel that can be processed yielding N image planes. For three image planes it is convenient to assign each plane a CRT beam color (ie. red, green, and blue) and modulate the intensity of each beam as function of space and the value of its

image plane. Thus three image planes can be simultaneously and independently observed in a single image.

The term "quantification imaging" is adopted here to describe images that directly relate quantities such as mass, concentration, bond lengths, dielectric response, etc. These are different from "qualitative imaging" where the dependent axis does not directly correspond to the quantity of interest, but there is some relationship to that quantity. An EELS or x-ray spectrum-image can be processed to generate a quantificational image of elemental concentrations as a function of spatial coordinates. A bright field image would be considered a qualitative image because its intensity is not directly related to such quantities.

Data collection for quantificational images can be divided into two types. The first is "on-the-fly" acquisition where data for a pixel is acquired, processed, the collected data is discarded, and only the processed data is stored. The stored data is generally a set of processed 2D or 1D image planes. The second type is batch collection where a 3D (or larger) spectrum-image is collected and stored for later processing.

## 4.1 "On-the-fly" processing techiniques

Until very recently, compositional image data was only collected using "on-the-fly" techniques to minimize data storage. In EELS, a typical image processed this way would involve collecting a spectrum for a single pixel, processing that spectrum to obtain and record the counts under one or more core-loss edges, and discarding the collected spectrum. Typically calculations for pixel N would be performed while a spectrum for pixel N+1 was being acquired. The process would be continued for each pixel in the image and the stored data would be one plane of data for each element. The amount of storage required for this was substantial up until only a few years ago.

Storage requirements for processed images (in words)

| Image size (pixels) | 1 plane | 2 planes | 3 planes |
|---|---|---|---|
| 64x64 | 4K | 8K | 12K |
| 128x128 | 16K | 32K | 48K |
| 256x256 | 64K | 128K | 192K |
| 512x512 | 256K | 512K | 768K |
| 1024x1024 | 1M | 2M | 3M |

Limitations with "on-the-fly" processing occur because processing times and acquistion times are related. For simple processing there need not be a problem but complicated processing may cause unreasonably long acquisition times.

## 4.2 Batch processing

Batch processing of EELS image data (or x-ray image data) was only performed recently in electron microscopy because the storage demands had previously been too costly. These techniques store large amounts of the collected data for later processing.

Storage requirements for a spectrum-image (in words)

| Image size (pixels) | 1K ch /pixel | 2K ch /pixel | 3K ch /pixel |
|---|---|---|---|
| 64x64 | 4M | 8M | 12M |
| 128x128 | 16M | 32M | 48M |
| 256x256 | 64M | 128M | 192M |
| 512x512 | 256M | 512M | 768M |
| 1024x1024 | 1G | 2G | 3G |

Processing individual EELS spectra in an image "on-the-fly" is often insufficient for quantitative imaging. The capability to process the spectrum-image multiple times is gained by saving the entire spectrum- image and batch processing the data. Erroneous fitting and unexpected acquisition problems

that frequently cause "on-the-fly" processing errors can often be overcome through modifications to the processing software without re-acquiring the image. Edges whose existence were not predicted prior to acquisition can also be processed. Most importantly, processing time need not be limited to acquisition time, and thus complicated and robust analysis routines may be used. Multiple least-squares (MLS) fitting routines in place of linear least-squares (LLS) and area ratio techniques can greatly improve accuracy and detectability. Other time-consuming analysis methods such as isolating chemical effects and dielectric information can be employed. Processing time for such routines most likely far exceed the desired acquisition time, particularly when specimen drift, beam sensitivity, and microscope operating costs are concerns.

On a multi-tasking system, it is possible for batch processing to begin while data is being collected. The author has concluded that the only reason to do "on-the-fly" processing is when batch processing can't be performed because of equipment and storage limitations. Conservation of storage space is the only significant advantage of "on-the-fly" processing over batch processing. A minor advantage is that the image is immediately ready for display after "on-the-fly" image processing.

## 4.3 Drift corrections

When acquiring an image it is possible for any of the independent coordinates to drift from their presumed positions. For the spatial dimension this can be due to random specimen drift induced by vibration or by localized specimen heating. The energy-loss dimension can drift from slow changes in the beam accelerating voltage or from descanning errors causing the beam to enter the EELS spectrometer at varying angles.

The probe current can also change during an image; this can be considered a change in the scaling factor of the dependent dimensions of the spectrum-image.

Energy drift in a high-quality STEM using descanning coils should be negligible. Spatial drift will be a problem in any microscope at high magnifications over long periods of time. Probe current changes may not be important for thermionic sources but are significant with field emission sources. The H700H TEM where much of this work was performed exhibited large energy, current, and spatial drift problems. Thus it was necessary to develop means of correcting for these faults to obtain reasonable images.

### 4.3.1 Energy-drift correction

This correction is best done after acquisition because it can become relatively complex and it is often done incorrectly on the first attempt. The basis behind the correction is to find a "feature set" of invariant features at fixed energy-loss such that at least one member of this set is found in each pixel of the spectrum-image. The object of the correction is to calibrate the energy scale of the spectrum in each pixel of the spectrum-image by matching a feature of known energy-loss to a feature in the spectrum.

The first step is to find an element in the feature set that occurs in the spectrum with sufficient signal quality. Next, some characteristic of the feature must be exploited — for instance the maximum value in an edge or the slope of the edge threshold. A region in the spectrum is chosen to search for the feature selected, and the characteristic chosen is used as the search criterion.

Searching for the maximum value within a region is the most simple algorithm and can work quite well if that region is smoothed first. Still, in a noisy spectrum shot noise can seriously corrupt this method. A more robust and

slightly more involved technique is to search for an abrupt change in slope of a core-loss threshold. These methods work best for K- and L-shell edges, less well for higher order shells. Perhaps the best method is the fitting of an element in the feature set to the spectrum using a simplex method that varies both the energy-loss and feature height during the fit. If the feature includes only the first few electron volts of the core-edge then the correlation between the reference feature and the spectrum feature will be high even with significant plural scattering.

### 4.3.2 Probe current drift correction

When using a field emission source the intensity of the probe will often change by 50% for either long or short periods of time; sometimes the intensity will disappear altogether for fractions of a second. In such situations the probe current or an analogous signal must be recorded and used to scale the spectrum. The scaling is usually performed after acquisition.

This is often the most serious drift in spectrum-imaging. The current striking the selected-area aperture is the optimum signal to collect for this purpose, but this requires an aperture that is electrically isolated from the column. In microscopes where this is not possible the dark field signal can be used in its place. The current on the condensor apertures may not be useful because of variations in the probe current may not be linear over all angles, particularly with field-emission sources.

When none of these signals can be collected there are a few options. Under some conditions the low-loss signal can be collected as shield current on the Gatan 666 PEELS — this can not be relied upon in the general case because some energy losses may pass through the gap between the shield and the detector array. Sometimes the probe current can be estimated from the LL. If

the LL is not available it is occasionally reasonable to use the entire recorded spectrum to calculate the scaling factor, provided the spectrum includes the the low energy-loss edges of the major constituents.

### 4.3.3 Spatial-drift correction

Performing this correction "on-the-fly" is not clearly inferior or superior to correcting after acquisition. The former requires no additional storage space and ensures that the pixel dwell time is the same for each point in the image. Batch spatial-drift correction requires large amounts of data to be stored each time a test for drift is made. If the specimen does drift then some pixels will have longer equivalent dwell times than others, i.e. the beam dose for each point within the specimen image area is not constant. Additionally the dimensions of the processed image may be different from the unprocessed image. The author prefers to use on-the-fly spatial-drift correction and use tests for drift performed frequently enough that the image drifts no more than one or two pixels per test (generally at the end of each scan line).

# Chapter 5
# EELS Quantificational Imaging

"On-the-fly" techniques are typically restricted to non-intensive calculations such as the two-area method or linear least-squares (LLS). Batch processing allows far more complicated techniques. The techniques in this section were examined with hopes of using the processed information for imaging. Only the methods that calculate mass or concentration have been implemented.

## 5.1 Two-area method

This is a fast and accurate method for estimating the number of counts in a core-loss edge for compositional microanalysis when plural scattering effects are negligible or have been corrected. Its minor computational demands make it a natural choice for quantitative imaging because it requires far less processing time than linear least-squares (LLS).

The intensity of the spectrum from the ionization threshold of the core-loss edge of interest to an arbitrary energy of lower energy loss is assumed to be:

$$J_{ideal}(E) = A \cdot E^{-r} \tag{5.1}$$

where $J$ is the intensity at energy-loss $E$, $A$ and $r$ are constants.

Two windows are chosen directly before the core-loss edge threshold as in figure 5-1. The intensities of these windows $I_1$ and $I_2$ are geometrically averaged in log-log space to produce values at $E_2$ and $E_3$. These points are used to fit a line in log-log space that extends beneath the core-loss edge through the window $I_b$. The counts below this line are integrated between $E_2$ and $E_4$ resulting in the intensity within the window $I_b$.

(Egerton, 1986) demonstrates that the errors created from this

**Figure 5-1:** The two-area method of background fitting

approximation do not exceed 1% from the ideal power-law model when $r$ is less than 6 (as is typical in an EELS spectrum).

Equations for the two-area method are shown below:

$$r \approx \frac{log(E_2/E_1)}{2\,log(I_1/I_2)} \tag{5.2}$$

$$A = \frac{(1-r)I_2}{E_2^{\,1-r} - E_3^{\,1-r}} \tag{5.3}$$

$$I_b = \frac{A\,[E_4^{\,1-r} - E_2^{\,1-r}]}{1-r} \tag{5.4}$$

## 5.2 Linear Least-Squares

This method also assumes that $J_{ideal}(E)$ follows the power law in equation (5.1). Its basis is to minimize the fit parameter $\chi$ which is equivalent to minimizing the squared difference between $J_{ideal}$ and $J_{actual}$ in log-log space.

$$\chi^2 = \sum_i \frac{log(J_{ideal,i}) - log(J_{actual,i})}{s_i^2} \tag{5.5}$$

$s_i$ is the standard deviation for each channel and is usually held constant.

By minimizing $\chi^2$, a straight line under the edge can be fit in log-log space using the standard LLS equations.

$$y = m \cdot x + b \tag{5.6}$$

$$m = \frac{N\sum X_i Y_i - \sum X_i \sum Y_i}{N\sum X_i^2 - (\sum X_i)^2} \tag{5.7}$$

$$b = \frac{\sum Y_i - m\sum X_i}{N} \tag{5.8}$$

where $X_i = log(E_i)$, $Y_i = log(J_{actual}(i))$, $E_i$ is the energy-loss at channel $i$.

The fit is performed on a window before the core-loss edge, such as between $E_1$ and $E_2$ in figure 5-1. As with the two-area method, once $A$ and $r$ are known the intensity in the window $I_b$ is found using:

$$I_b = \frac{A\,[E_4{}^{1-r} - E_2{}^{1-r}]}{1-r} \tag{5.9}$$

## 5.3 Comments on fitting with the two-area and LLS methods

Both of these methods work well when plural scattering effects are minimal, or the spectrum can be said to represent a single-scattering distribution (SSD). The two-area method introduces an approximation error but this can be considered minimal in comparison to the other errors that plague EELS microanalysis. These larger errors include:

- *Choice of fitting window position and size.* The value of $r$ changes slightly as a function of $E$. Changing the fitting window position and size will change the counts calculated for $I_b$. This effect can be minimized by choosing $\sigma_i$ to weight channels close to the edge threshold most strongly.

- *Choice of integration window position and size, and cross sections.* Generally ionization cross sections are theoretically generated using programs such as *SIGMAK* and *SIGMAL* (Egerton,1981). However bonding effects can introduce errors into these cross sections as larger than 50%. Additionally, white lines and other large near-edge effects are often not correctly predicted using theoretical models.

- *Plural scattering.* The redistribution of counts beyond the CL threshold due to plural scattering will cause these methods to underestimate of the number of counts that belong in the associated SSD spectrum. The situation for single spectra can be corrected using either the Fourier-log or Fourier-ratio technique, but these methods are generally too time consuming and unstable to be used for each pixel of an image.

These uncertainties give cause for many laboratories to consider EELS as little more than a curiosity — not an accurate method for microanalysis. Although a seasoned EELS researcher can often select the correct parameters and cross sections, EELS fitting to a power-law equation is not a "turn-key" technique. Until it becomes such, many researchers will choose more straighforward techniques such as x-ray microanalysis over EELS even in situations where the sensitivity or accuracy of EELS is clearly superior.

## 5.4 Multiple Least Squares

It is possible that multiple least-squares (MLS) techniques are a step closer to a "turn-key" approach of microanalysis. Here reference spectra are fit to the unknown spectrum to find the relative concentrations of the reference elements and the thickness of the specimen.

The first attempts at using MLS fitting by the author used techniques developed by (Shuman...,1987) and (Leapman...,1988) on carbon, oxygen, and nitrogen within a beta cell. These techniques are somewhat specialized for biology because they require (1) a "major element" or an element that is both a major constituent and precedes the other elements of interest in energy-loss, and (2) they assume that the bonding within these specimens do not noticably alter the core-loss edge shape in the unknown spectrum with respect to the edge shapes within the reference spectra. The latter restriction presents a difficulty for materials systems because chemical shifts from bonding effects can signficantly alter edge shapes as a function of concentration. Thus reference spectra are not apt to be identical to the SSD components of the unknown spectrum.

The major strengths of the MLS technique are:

- Plural scattering effects can be accurately removed without knowledge of specimen thickness, specimen cross sectional shape and uniformity (at the beam), and the low-loss spectrum need not be collected. In PEELS it is often not convenient or even possible to record both the CL and LL portions of the spectrum under the same microscope conditions, particularly during imaging. Without a LL spectrum for each CL spectrum, Fourier based techniques can not be used. Additionally, Fourier based techniques require an even thickness, homogenous elemental distribution under the beam — a

condition that is often difficult to meet.

- The cross sections of the analyzed elements need not be theoretically generated thus removing the largest source of error from the quantification process.

### 5.4.1 Generalized principle of EELS MLS

EELS MLS fitting was developed for biological systems by (Shuman..,1987) and (Leapman..,1988), but these treatments are not applicable to all specimens. The following treatment is a generalization of MLS methods developed by the author so that MLS may also be applied to inorganic materials.

A set of *convolution* spectra are created from the single-scattering intensity, $J^{SSD}(E)$, of each reference spectrum, and is referred to as $S_i(E)$. It suffices in most instances to use only the ZL and the first plasmon of the reference spectrum as $S_i(E)$. The convolution spectra are defined as:

$$C_{ij}(E) = k_{ij} \prod_{j \geq 0}^{*} S(E) \qquad (5.10)$$

$k_{ij}$ is a weighting function that describes the probability of plural scattering $j$ times in CL signal $i$. For a specimen with a homogeneous elemental distribution and even thickness under the beam, $k_j = k_{ij}$ obeys Poisson statistics,

$$k_j = \frac{1}{j!} \frac{t}{\lambda_t} \qquad (5.11)$$

where $t$ is the specimen thickness and $\lambda_t$ is the mean free path for plasmon excitation.

The experimentally acquired reference SSD spectra, $R_i(E) = R_{i,0}(E)$, are next convolved to form a new set of *convolved reference spectra*,

$$R_{ij} = R_{i,0} * C_{ij} \qquad (5.12)$$

For example, $R_{0,0}(E)$ is the SSD for the first CL edge, and $R_{1,0}(E)$ is the SSD for the second CL edge. $R_{0,1}(E)$ is a convolved reference spectrum for the

first element where every electron has undergone two energy-loss events.

The CL signal $J_i^{CL,SSD}$ for element $i$ is related to the reference spectra through $W_i$,

$$J_i^{CL,SSD} = W_i \cdot R_i(E) \tag{5.13}$$

where $W_i$ is the relative concentration of element $i$.

The plural scattering distribution (PSD) of the CL signals are,

$$J_i^{CL,PSD} = W_i \sum_{j>0} R_{ij}(E) \tag{5.14}$$

The CL signals in the unknown spectrum combine to form the *measured unknown spectrum*,

$$\sum_{i \geq 0} J_i^{CL}(E) = \sum_i W_i \sum_{j \geq 0} R_{ij}(E) \tag{5.15}$$

This equation is grossly over-specified and may converge to aphocryphal solutions if all the degrees of freedom are permitted. To make the problem managable, (Leapman...,1988) make several assumptions. They first assume that $S(E)$ is simply a delta function for the zero-loss and a single plasmon from the low-loss of a reference spectrum. This is a valid approximation because the intensity of the remaining SSD spectrum is close to zero in comparison — even more so after multiple convolutions with itself. The method assumes there is a "major element", one that produces the largest edge and is at the lowest energy-loss. An additional constraint is that as the constituent elements are varied in concentration the shape of the core-edges is invariant. For biological samples these conditions are not usually restricting because carbon has a large cross section, its edge is at a low energy loss, and it is usually the major detectable component in biological systems.

For the first iteration of the fit it is assumed that $W_i \cdot R_{ij} = 0$ for ($i$>0 and $j$>0). An equivalent statement is that there is no plural scattering on the edges of the minor elements. This iteration determines the relative weighting factors

$W_i$ of the reference spectra and the weighting function $k_j$ of the plural scattering terms of the major element.

Following iterations assume that the $k_j$ factors of the major element from the previous iteration describe the plural scattering of the minor elements for the current iteration. The fit recalculates $W_i$ for all elements and $k_j$ for the major element. The fit stops when $k_j$ converges to within a specified tolerance.

The technique is excellent for quantifying even small overlapping edges convolved with up to four plasmons. However, this method can not be directly applied to the majority of materials samples without modification. Inhomogeneous elemental distribution under the beam invalidates the assumption that $k_j = k_{ij}$. A major element may not always exist.

A more serious difficulty is the presence of multiple forms of bonding to the same element. If the reference spectra contain different shapes of core-edges due to bonding differences, the technique will be inaccurate. This situation can be solved if a reference spectrum for each type of bonding is used in the fit.

### 5.4.2 Separation of core-loss signals from multiple isomorphs

An MLS routine was used to separate core-loss signals from three isomorphs of carbon: amorphous (from formvar), graphite, and diamond.

The near edge regions of the three reference spectra were fitted to the unknown spectrum. It was assumed (somewhat incorrectly) that plural scattering was unimportant because the plural scattering effects do not dramatically change the very near-edge region.

First $\sum_i J_i^{SSD,CL}(E)$ was found for $i$ = 0,1,2 (formvar carbon, graphite, diamond) by removing the background beneath the carbon edge with a LLS method. $k_{j>0}$ is assumed to be zero. $R_1, R_2, R_3$ were obtained from specimens

**Figure 5-2:** Carbon core-loss structures of a) formvar b) graphite c) diamond

containing only formvar, graphite, and diamond respectively. The fit then iteratively solves for $W_i$.

The average fitting time with energy-drift correction was 17.97 seconds per pixel on the system described in chapter six. When applied at each point on a 128x128 pixel spectrum-image the image planes were obtained in under 3.5 days. Fitting with $k_{j \geq 0}$ would have required far longer.

## 5.5 Extended Energy-Loss Fine Structure (EXELFS)

The local density of states and binding energies alter the shape of the pre-ionization edge foreground, and slightly change the energy threshold of an ionization edge. This information can be used to determine various bond characteristics. Techniques such as energy-loss near-edge fine structure (ELNES) and extended energy-loss fine structure (EXELFS) extract bonding angles, lengths, and energies from oscillations along the post-ionization edge background.

EXELFS was investigated in an attempt to use bond-lengths as an imaging signal across different phases or grain boundaries. ELNES was also examined but its interpretation is not useful for imaging with measurable energy-drift. Energy-drift correction here is very complicated because the relative energy changes of edge thresholds are of interest.

Superimposed upon the exponentially-decreasing post-ionization core-loss edge in an electron energy-loss spectrum is a fine structure. This fine structure consists of intensity oscillations which are observable along the post-edge for several hundred eV, provided no other ionization edges interfere in this range and the noise level in the spectrum is sufficiently small. The oscillations of interest occur more than 50 eV past the ionization edge and is termed EXELFS, whereas oscillatory fine structure that exists within the 0 - 50 eV range past the ionization edge are termed near-edge fine structure or energy-loss near-edge structure (ELNES).

The history of EXELFS is brief and relatively little research has been conducted due to instrumental limitations. Previously ELNES was given more attention than EXELFS because counting statistics are less important in ELNES. This may change because of the commercial introduction of parallel EELS. Despite its youth and lack of attention, EXELFS deconvolution is well

developed due primarily to theory borrowed from a similar and older technique, extended x-ray absorption fine structure (EXAFS).

### 5.5.1 Extended X-ray Absorption Fine Structure (EXAFS)

EXAFS arises from oscillations superimposed upon the absorption cross section of an inner-shell electron in an x-ray absorption spectrum (XAS). The oscillations are generated from interactions of the electrostatic potential of the excited core electron with the local atomic environment (Sayers.., 1971) and thus the structural information obtained from EXAFS is predominately due to nearest neighbors.

The probe used in EXAFS is typically a synchrotron radiation source because large, highly monchromatic x-ray energies are desired. Advantages of EXAFS over EXELFS include the ability to examine bulk specimens, less radiation damage, and easier deconvolution of the structural information. EXELFS advantages over EXAFS include the ability to examine thin foils with spatial resolution on the order of nanometers, shorter acquisition times when analyzing small Z elements, and the ability to weight structural information toward a particular direction within a specimen.

An in-depth treatment of EXAFS will not be covered here as it is not an EELS technique. However the theory of generating structural information from the oscillatory fine structure is virtually identical in EXAFS and EXELFS. Figure 5-3 demonstrates three EXAFS spectra of the Ge K-shell absorption fine structure in amorphous $GeO_2$, and the tetragonal and hexagonal crystalline polymorphs of $GeO_2$. The spectrum of the amorphous sample is very similar to that of the hexagonal $GeO_2$ spectrum suggesting that the short-range order of the glass is close to hexagonal.

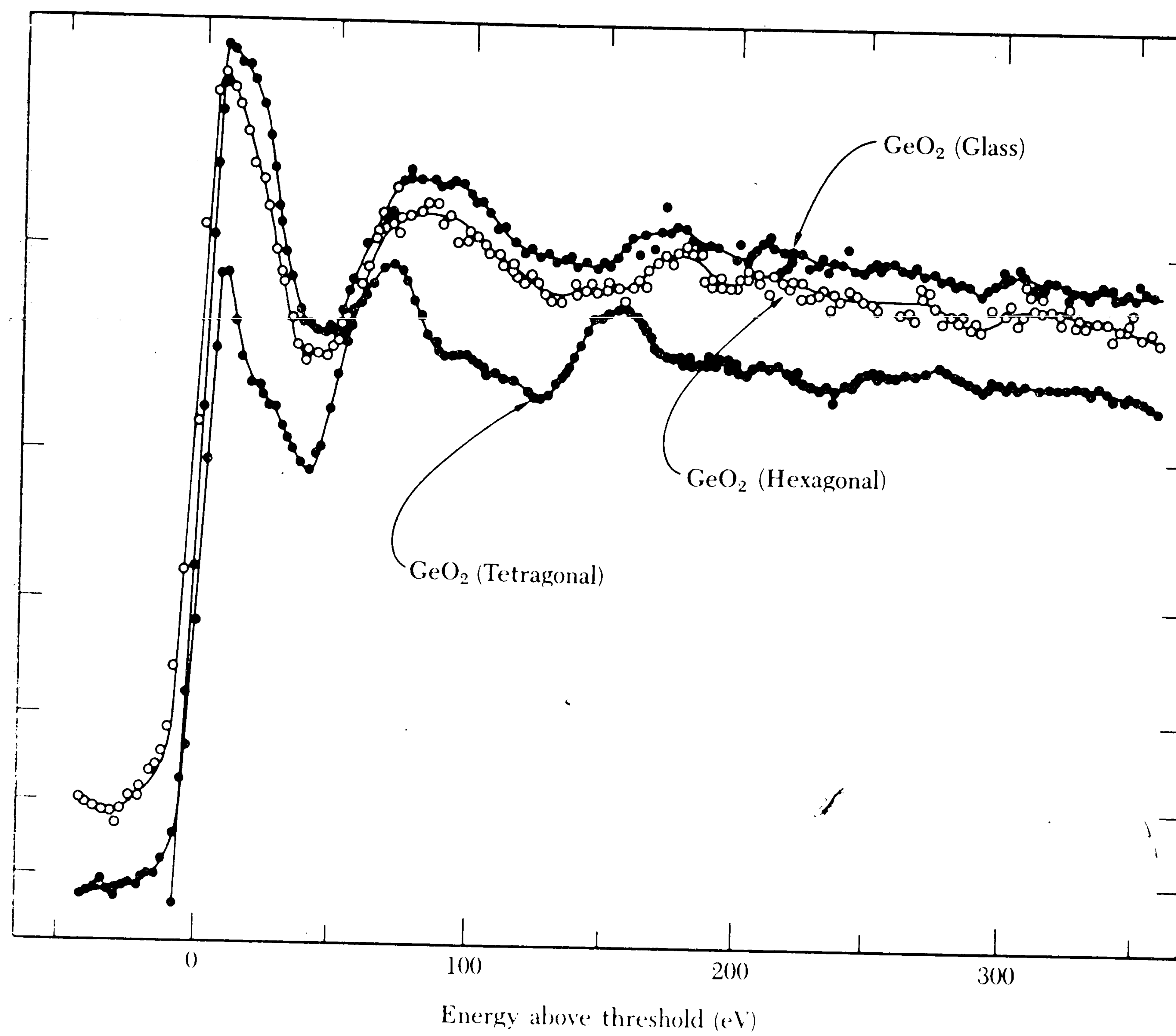


**Figure 5-3:** EXAFS of one glassy and two crystalline forms of $GeO_2$ as a function of energy above the Ge K-shell ionization edge. (Kittel, 1986)

### 5.5.2 EXELFS Theory

For examination of fine structure past an ionization edge it is useful to write the inner-shell differential inelastic cross section as a product of the density of final, or post-ionization states $N(E)$ and an atomic transition matrix $M(E)$:

$$J(E) \approx \frac{d\sigma_i}{dE} \approx |M(E)|^2 N(E) \tag{5.16}$$

Where $J(E)$ is the intensity of single scattering as a function of energy loss $E$ and is taken directly from an EELS spectrum that has been corrected for plural scattering. Beyond the ionization threshold and up until the next higher energy ionization threshold, $M(E)$ can be considered to be a smoothly decaying function, and therefore variations in $J(E)$ reflect the density of states (DOS) above the Fermi level. Although this model is greatly simplified, it provides a reasonable basis for the interpretation of EXELFS (and EXAFS) (Egerton, 1986).

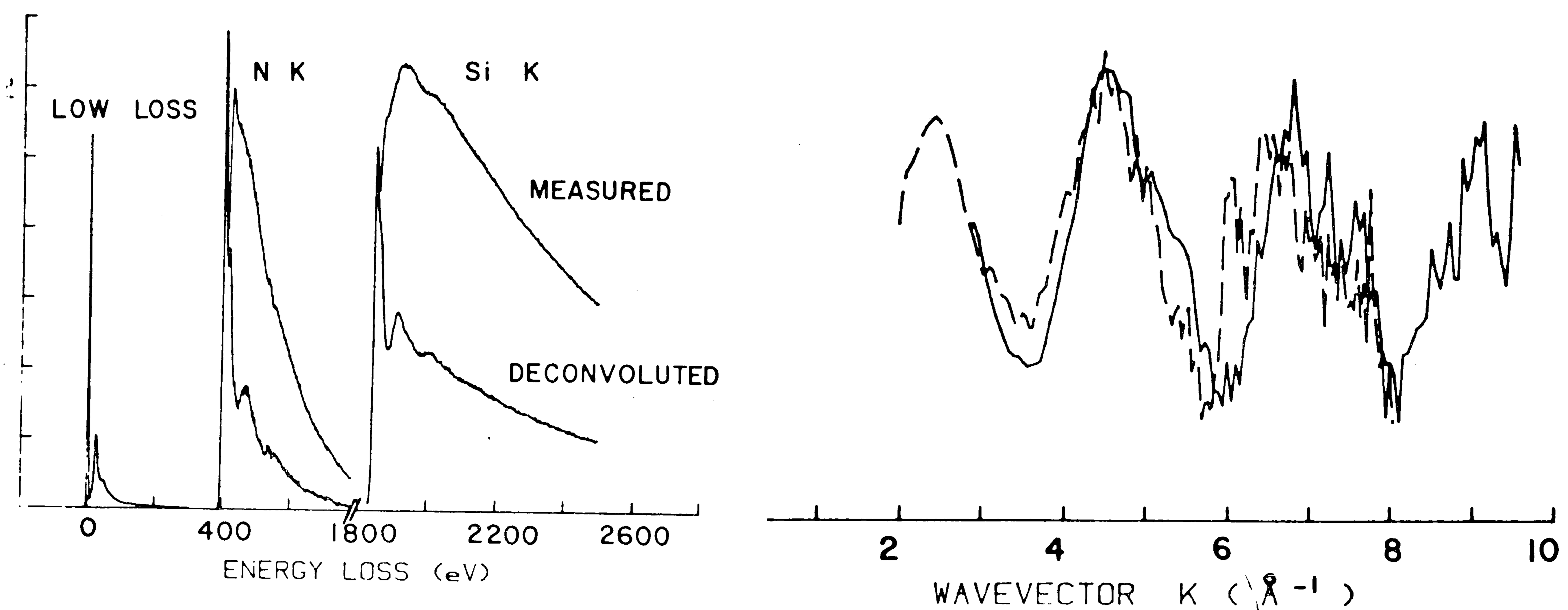


**Figure 5-4:** Left: EELS spectrum of amorphous SiN. Right: EXELFS of amorphous SiN after background subtraction. Si K-edge (solid line) and N K-edge (dashed line) shown. (Leapman,1982)

To be included in the extended fine structure, a core electron must be ionized to a kinetic energy of at least 50 eV, and thus it behaves as a free electron. As the electron leaves its binding level it may be modeled as an outgoing spherical wave, with a wave vector **k**,

$$k = \frac{2\pi}{\lambda} = \frac{[2m_o(E-E_k)]^{1/2}}{\hbar} \tag{5.17}$$

Where $E$ is again energy loss and $E_k$ is the energy loss corresponding to

the ionization threshold. The ejected electron has a very small wave vector and hence the probability of a high-angle elastic collision (backscattering) with the nearest neighbors or the next nearest neighbors approaches unity. Weak oscillations on the post-ionization edge (fine structure) are caused by the constructive and destructive wavefront interference between the ejected electron leaving the host atom and the backscattering of the electron off a nearest neighbor. The interference is alternately constructive and destructive depending on the wavelength $\lambda$ of the ejected electron and the return path length $2r_j$, where $r_j$ is the radial distance to the $j^{th}$ shell of the backscattering atom.

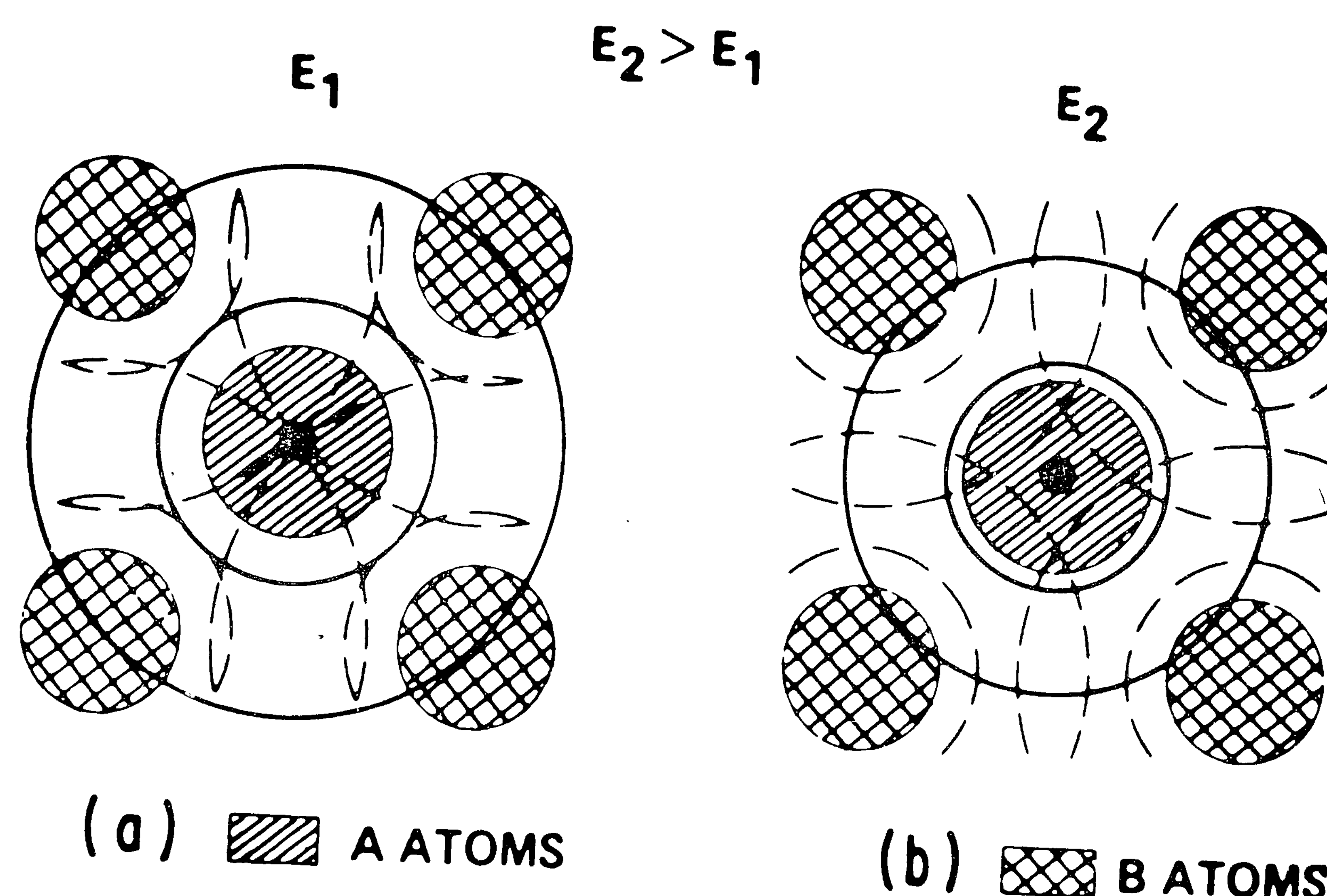


**Figure 5-5:** Pictorial representation of the electron interference that causes EXELFS. The ejected electron comes from the A atom. The solid circles represent the peaks of the outgoing wave function, while the dashed circles represent wave functions of backscattered electrons. Constructive interference is portrayed in **A** and destructive interference in **B**. (Schattschneider, 1986)

Assuming that the effects of plural scattering are negligible or have been corrected, the oscillatory fine structure can be represented in a normalized form:

$$\chi(E) = \frac{J(E) - A(E)}{A(E)} \qquad (5.18)$$

where $A(E)$ is the smooth energy-loss intensity that would exist if no fine structure were generated and can be calculated from a single-atom model (Egerton, 1986). Although $A(E)$ can be calculated, it is more accurate to fit a smoothly varying function such as a cubic spline through the post-edge region of $J(E)$; the remaining intensity is the unnormalized fine structure. Approximating the ejected and backscattered electron wave functions as plane waves and assuming that multiple backscattering can be ignored, standard EXAFS theory can be used to interpret the behavior of $\chi$ (Sayers.., 1971):

$$\chi(k) = \sum_j \frac{N_J}{r_j^2} \frac{f_i(K)}{k} \exp(-2r_j / \lambda_i) \exp(-2\sigma_j^2 k^2) \sin [2kr_j + \phi(k)] \qquad (5.19)$$

Where the summation is over increasingly larger shells of neighboring atoms of shell radius, $r_j$. The most significant contribution to the fine structure occurs from scattering off nearest neighbors ($j$ = 1) unless the scattering power of these atoms is small ($Z$ = 1,2,3). Contributions from other shells decrease rapidly as $r_j$ increases and thus structural information beyond a nanometer requires excellent counting statistics to provide a high signal-to-noise ratio. $N_j$ is the number of atoms in shell $j$ and is known as the radial distribution function (RDF). The RDF describes the probability of an atom occuring at $r_j$ ; it is a function of the distance from the ionized atom and the elastic scattering cross section of atoms in shell $j$.

The elastic scattering form factor, $f_j(k)$, describes the backscattering event probability as a function of the magnitude of the wave vector of the ejected electron, $k$. For light elements $f_j(k)$ can be predicted using a Rutherford model:

$$|f_j|^2 = \frac{4\gamma Z^2}{a_o^2 q^4} \approx \frac{Z^2}{4a_o^2 k_o^4} \qquad (5.20)$$

Where $a_o$ is the Bohr radius, $q$ is the magnitude of the scattering vector ($q \approx 2k_o sin(\tau/2)$, for small $\theta$), and $\gamma^2$ is the relativistic correction that is unity for the ejected electron. This simple model fails for heavy elements because core electrons screen the nucleus, reducing its effective charge. The Rutherford model can be adapted to incorporate screening by reducing the $Z$ term, as in the Lenz atomic model:

$$|f_j|^2 = \frac{4\gamma Z^2}{a_o^2(q^2 + r_o^2)^2} \tag{5.21}$$

The screening radius, $r_o$, can be estimated by using the Thomas-Fermi statistical model for low $Z$,

$$r_o = a_o Z^{-1/3} \tag{5.22}$$

and a modification to the Thomas-Fermi model can be used for high $Z$:

$$r_o = 0.9 a_o Z^{-1/4} \tag{5.23}$$

The Lenz method underestimates small-angle scattering at very high $Z$ primarily due to the neglect of electon exchange but is generally sufficient for EXELFS. Several more accurate and calculation intensive quantum-mechanical methods such as the Hartree-Foch, Hartree-Slater, Langmore, or Bethe formulae exist for improved accuracy at very high $Z$.

The definition of low and high $Z$ is somewhat vague and varies for each model. For the purpose of screening, high $Z$ is considered to start in the fourth period and continue up through mercury.

Inelastic scattering of the ejected electron after scattering changes $k$ and the interaction between the incoming and outgoing spherical waves. The damping term $exp(-2r_j/\lambda_i)$ is a function of the mean free path for inelastic scattering, $\lambda_i$. Absorption is a strong function of **k** and occurs from both electron-electron and electron-phonon collisions (see Figure 5-6). $\lambda_i$ is generally

less than 1 nm for electron energies less than 100 eV, so inelastic scattering limits the range of shell radii ($r_j$) that contribute to the RDF (Egerton, 1986). The lifetime of the core hole ($\tau_h$) produced when the electron is ejected is another spatial resolution limitation in EXELFS.

)

**Figure 5-6:** Mean free path for inelastic scattering of an electron. (Egerton, 1986)

The statistical broadening of RDF peaks relates to deviations from the mean position of an atomic shell and are caused by vibrational energies, ie. thermal, zero-point, phonons, etc. The term $exp(-2\sigma_j^2k^2)$ is a Fourier transform of the radial-distribution function. The disorder parameter $\sigma_j$ is similar to the Debye-Waller term $u_j$ used in diffraction theory to account for scattering from phonons, but differs in that only the radial components of the relative motion between the central ionized atom and the backscattering atom are of concern in EXELFS. The $u_j$ term is used to correct for the loss of elastic scattering at the expense of phonon scattering and is based on mean-square atomic

displacements perpendicular to the plane of elastic scattering. The value of $\sigma_j$ is dependent on the charge and mass of the backscattering atom, and the strength and directionality of the bonding.

The interference between the incoming and outgoing spherical waves is considered in the term $sin[2kr_j+\phi_j(k)]$ of equation (5.19). The phase change induced upon the electron wave as it travels through the fields of the emitting and backscattering atoms are represented by $\phi$. This phase difference can be split into two components, $\phi_e$ and $\phi_b$, arising from the emitting and backscattering atoms, and can be calculated individually from atomic wave functions. Symmetry of the emitted wave and its associated phase change are modified by the dipole selection rule such that a K-shell ionization emits a wave with a $p$-symmetry and an $L_{23}$ ionization produces a wave with a $d$-symmetry. $\phi_b$ differs in each case. In crystalline materials the symmetry is further modified by specimen orientation, allowing measurement of bond lengths in specific directions.

### 5.5.3 Data Acquisition

The amplitude of the EXELFS oscillations is typically less than 5% of the post-ionization background and thus extraction of structural information from these modulations requires high channel counts to obtain high signal/noise ratios. Shot noise is introduced into the EELS spectrum through fluctuations in the incident beam energy generally caused by beam filament instabilities. Small energy variations such as the Gaussian filament energy distribution (less than 5 eV, typically less than 2 eV) that are less than half the periodicity of the EXELFS modulations (20 eV or more) do not affect the EXELFS analysis with even moderate counting statistics. It is the shot noise that makes large counts necessary, beyond the capabilities of the majority of microscopes equiped soley

with serial EELS.

### 5.5.4 Data Analysis

Two methods of extracting the RDF from the EXELFS modulations, $\chi(k)$, were found in the literature. The original procedure used for EXAFS (Sayers..,1971) is based upon conversion of the EXELFS data into Fourier space. An alternative and more accurate method uses non-linear curve fitting of $\chi(k)$ to an assumed model of the atomic structure and varying the elastic form factor ($f_j$), the coordination number ($N_j$), and the disorder parameter ($\sigma_j$). Both analyses begin with an EELS spectrum of the core-loss edge and background that has been corrected for plural scattering.

Analysis is most accurate and straightforward if a K-shell edge is used, although this is not possible for $Z > 15$ because the amplitude of the K-edge becomes to small and the L-edge should be used to obtain the necessary signal/noise ratio. For transition metals, the $L_1$ edge occurs within the energy range of the $L_{23}$ EXELFS modulations and must be removed by subtracting off the counts due to the $L_1$ edge. The size of the $L_1$ edge and background can be estimated from the height of the $L_{23}$ edge and the relative transition probablities of these edges. For transition elements beyond $Z = 22$, the $L_2$-$L_3$ becomes significant (greater than 5 eV) and the mutual interference of the EXELFS modulations from each edge makes separate treatment for each edge necessary (Leapman.., 1982).

### 5.5.5 Conclusions on EXELFS imaging

Computation time of the RDF using EXELFS exceeds 25 seconds per pixel on the system described in chapter six. Difficulties in determining the onset of the core edge lead to errors as large as 100% in bond length determination. To resolve this problem even more substantial algorithms must be developed, further increasing the processing time. A 64x64 pixel EXELFS image is predicted to require 4 days of processing time.

## 5.6 Dielectric response images

Processing an EELS spectrum-image for dielectric response yields a four dimensional image; two spatial dimensions, a frequency dimension and an independent complex dielectric coefficient dimension. This section deals with the procedure of extracting the dielectric response function from an EELS spectrum. Only analysis of individual spectra has been attempted so far — the processing algorithms must be optimized to reduce computation times for imaging.

Analysis must be performed on a spectrum with plural-scattering effects removed. The single-scattering intensity $J^1$ is related to the imaginary part of the reciprocal of the complex relative dielectric response function (or the energy-loss function) as follows:

$$J^1(E,\beta) = A \cdot B(E) \cdot IM[\frac{-1}{\varepsilon(E,\beta)}] \tag{5.24}$$

$$\varepsilon(E,\beta) = \int_{q=0}^{\beta} \varepsilon(E,q)\, dq \tag{5.25}$$

where $\beta$ is the collection semi-angle of the spectrometer.

The single-scattering intensity can be calculated using a "Fourier-log" or "Fourier-ratio" technique discussed earlier. If the specimen is very thin then

the raw spectrum may be assumed to be free of multiple scattering. However, spectra from very thin specimens exhibit strong surface-loss components that may invalidate equation (5.24) and it is probably more accurate to deconvolve a spectrum from a slightly thicker sample.

The factor $A$ in equation (5.24) simply relates the energy-loss function to the spectrum intensity as a "stopping power" constant:

$$A = \frac{2I_o t}{\pi a_o m_o v^2} \tag{5.26}$$

where $I_o$ is the total beam current contributing to the spectrum, $t$ is the specimen thickness, $a_o$ is the Bohr radius, and $m_o$ and $v$ are the mass and velocity of the incident electrons.

The function $B(E)$ is referred to as an aperture correction and is used to normalize a spectrum taken with a collection aperture.

$$B(E) = \int_0^{\beta} \frac{\theta \, d\theta}{\theta^2 + \theta_E^{\,2}} \tag{5.27}$$

where $\theta_E$ is the characteristic angle,

$$\theta_E = \frac{E}{\gamma m_o v^2} \tag{5.28}$$

Once the energy-loss function is known, determining the dielectric response function is identical to that of optical techniques. The Kramers-Kronig relation is used to find the real part of the response according to equation (5.29). This technique is discussed more fully in (Kittel, 1986).

$$RE\left[\frac{1}{\varepsilon(E,\beta)}\right] = 1 - PP\,\frac{2}{\pi}\int_o^{\infty} IM\left[\frac{-1}{\varepsilon(E,\beta)}\right] \frac{E'\,dE'}{E'^2 - E^2} \tag{5.29}$$

where $PP$ is the principle part.

### 5.6.1 Relating optical permittivity with electronic permittivity

For small collection angles (scattering vector $\vec{q}$) the electronic permittivity, $\varepsilon(q,E)$, is essentially identical to the optical value, $\varepsilon(0,E)$ (Egerton,1986). The optical permittivity is a transverse property of the material, i.e. the electric field of the electromagnetic wave displaces atomic electrons in a direction perpendicular to the beam direction. The electronic permittivity produces a longitudinal displacement of atomic electrons and changes electron density in the form of plasmons. The transverse and longitudinal components are equal only at sufficiently small $\vec{q}$. However, there is little evidence for any significant differences when collection angles are small (less than 10 mrads) (Daniels..,1970) (see figure 5-7).

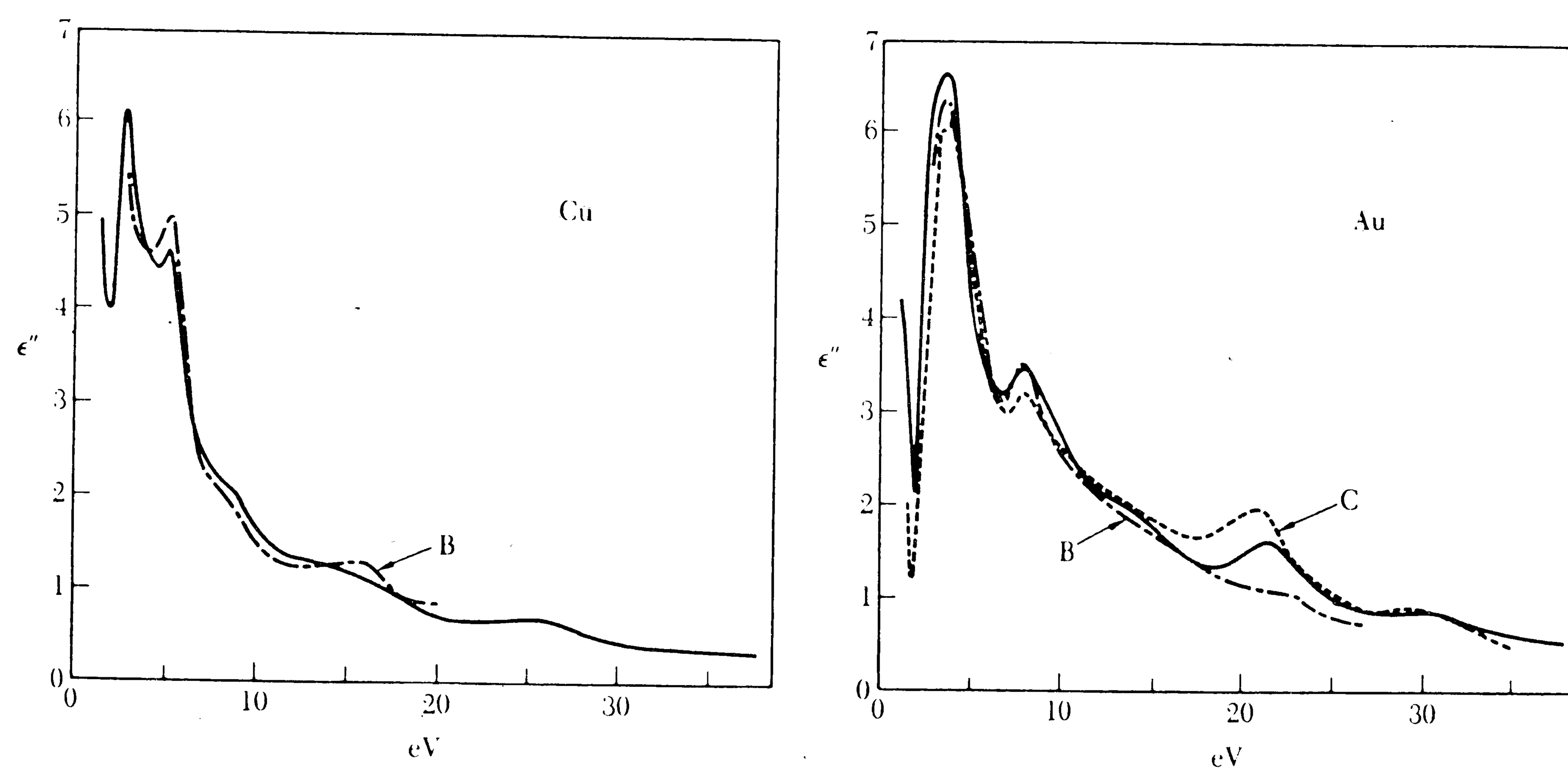


**Figure 5-7:** Energy-loss functions for Cu and Au; the bold lines are from energy-loss measurements, the other lines were calculated from optical measurements. (Kittel,1986)

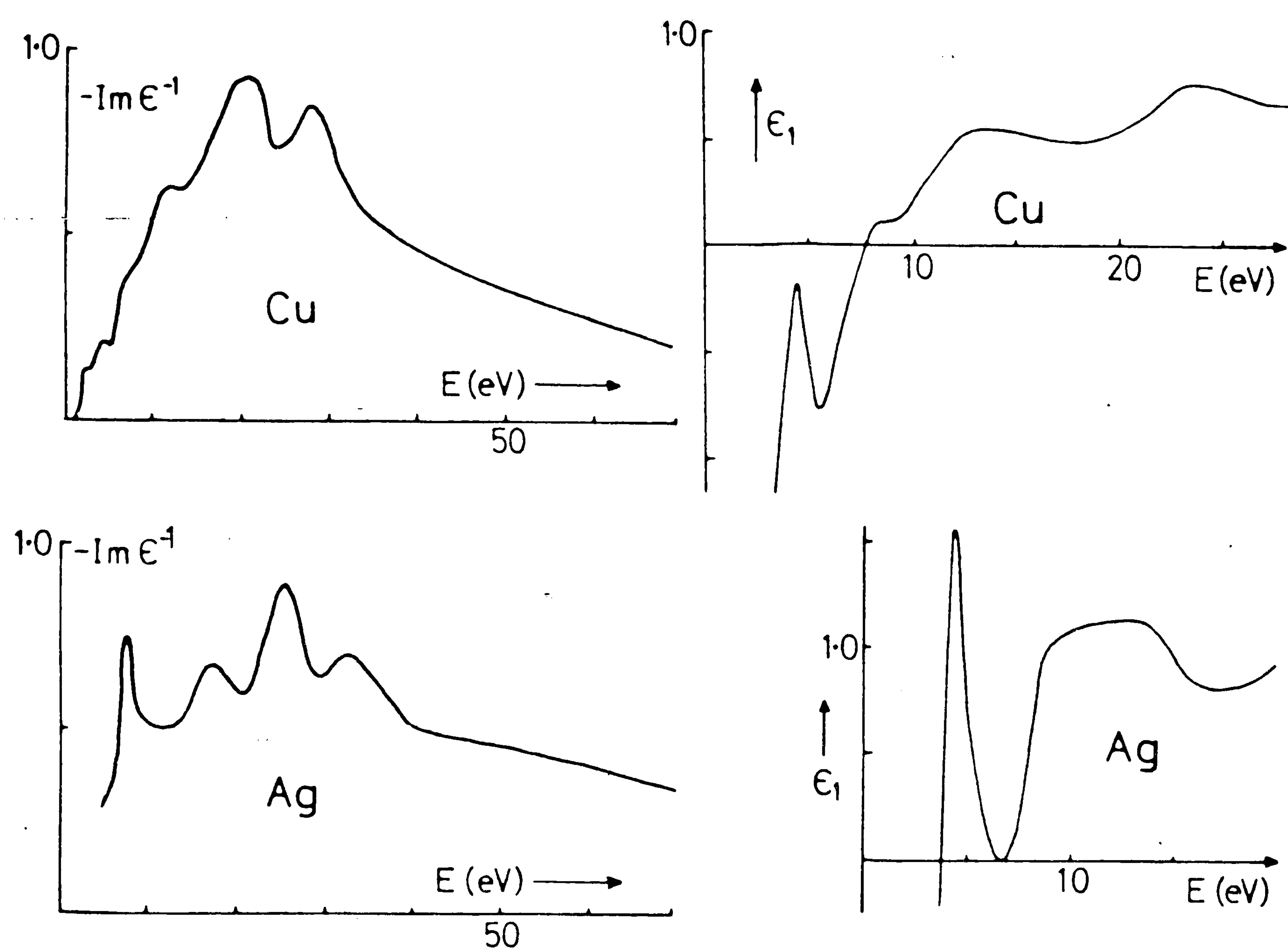


**Figure 5-8:** The energy-loss function $IM[-1/\varepsilon]$ and the real part $\varepsilon_1$ of the dielectric function, derived from EELS on polycrystalline films of silver, gold, and copper. (Daniels..,1970)

### 5.6.2 Scattering vector dependent dielectric response experiments

The dielectric response function can be calculated as a function of scattering vector q as follows.

1. Two spectra are acquired; one at collection semi-angle $\beta$, the other at $\beta+\beta'$, where $\beta'$ is small (around 1 or 2 mrad).

2. A spectrum corresponding to collection from only angles $\beta$ (spectrum #1) to $\beta+\beta'$ (spectrum #2) is calculated by subtracting spectum #1 from spectrum #2.

3. The energy-loss funtion is calculated and the Kramers-Kronig transformation is used to find the dielectric response function for $q = 2 \cdot k \cdot sin(\beta/2)$. ($k$ is the wave vector of the incident electron)

4. The process is repeated for multiple values of $\beta$ from 0 to perhaps 100 mrads. This will yield the dielectric response as a function of both energy and scattering vector.

The dielectric response can be found as a function of position on a specimen giving a "dielectric response map." $\varepsilon(q,E,X,Y)$ is an enormous amount of data but it is managable with the systems developed for this thesis.

### 5.6.3 Acoustic modes

The dielectic theory of layered 2D structures (superlattices) is of current interest in the semicondutor industry (Schattschneider,1988). Within each single layer of the lattice both symmetric and asymmetric modes propagate from an electronic perturbation. The symmetric mode (lower branch) corresponds to phase motions of electrons on opposite surfaces of a layer. The asymmetric mode (upper branch) corresonds to out-of-phase motion. (see figure 5-9) Surface

plasmons on each of the layers couple to form a set of N eigenmodes where N is the number of layers. When N is large the modes span a quasi-continuum (as in band gap theory) in the energy-momentum domain — these modes represent periodic oscillations inside the whole specimen and can be considered volume plasmons. The lower and upper boundaries of the continuum are analogous to acoustical and optical phonons. The plasmon continuum falls into a previously inaccessible energy momentum range and is more fully described in (Schattschneider,1988).

Acoustic frequency dielectric response may be calculated in real materials either by creation of a superlattice or through extremely thin specimens. With the latter the specimen width must be on the order of approximately 1/2 the mean free path (MFP) of the incident electrons — a difficult specimen to make. A superlattice could be created by alternating deposition of the material of interest to a depth of 1/2 of a MFP and a monolayer or two of a conductor. A description of surface plasmon interaction is found in (Egerton,1986).

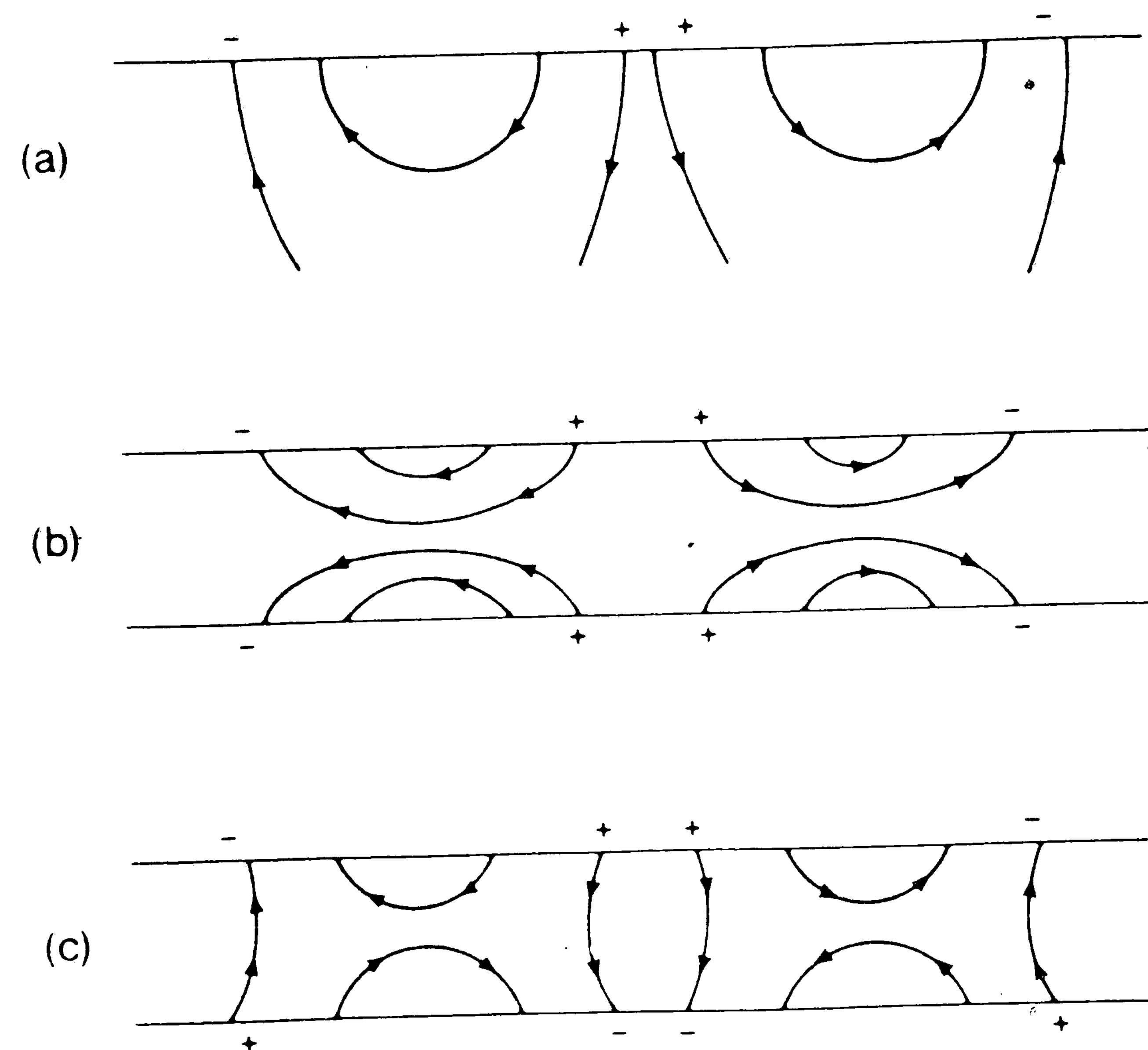


**Figure 5-9:** Electric field lines associated with surface plasmons excited in a bulk sample (a) and in a thin film (b and c). The plasmon frequency is higher in the symmetric mode (b) than in the asymmetric one (c).

# Chapter 6
# Hardware and software design

The increased recording efficiency of parallel EELS (PEELS) warrants the use of more involved acquisition and processing techniques than was necessary, or even possible with serial EELS. This increased complexity places greater demands on the computer systems controlling data acquisition. Multichannel analyzers systems with small resources and limited programming facilities are not capable of exploiting the full capabilities of the PEELS spectrometer.

Preliminary efforts of the author with the Gatan PEELS spectrometer were concentrated on development of a flexible acquisition system at the National Institutes of Health. Hardware control is performed through machine-language drivers called from high-level languages (HLL) such as FORTRAN and C. The software drivers and hardware were designed to minimize processor involvement in the data collection process, resulting in the capability to collect data while processing continues within the parent HLL. This design simplifies the HLL program structure and minimizes data collection dead time.

This chapter is intended to give an overview of the hardware and software designed for spectrum-imaging collection. Electronics are shown using block diagrams and software processes are depicted using general flow-charts.

## 6.1 Hardware

The system was created around an IBM personal computer (PC) AT clone, although any reasonably sized computer system could be used. The availability, quality, and low cost of PC hardware and development software allowed rapid system enhancements. Advantages of a PC based system include:

- *Cost.* A basic system can be constructed for around $5,000 (US). A

more expensive version could reasonably reach $10,000. Either is inexpensive in comparison to a commercial multi-channel analyzer (MCA).

- *Hardware.* A wide range of expansion peripherals is available; including analog-to-digital converters (ADC) and digital-to-analog converters (DAC), counter-timers, and digital I/O cards. Also printers, plotters, disk and tape drives, mice, etc.

- *Software.* A great variety of PC languages and general data analysis packages are commercially available.

- *Availability.* PC's are very popular; hence data and programs can be shared easily.

- *Flexibility.* Most importantly, PC based systems can perform many experiments that MCA manufacturers cannot. Reasons for this include: superior architectures of new and constantly evolving PC hardware, difficulty in making some experiments and routines general and idiot-proof enough for commercial release, the economics of producing very complicated software for a very small marketplace, etc.

Disadvantages include:

- *Initial setup.* Building your own system requires much software and hardware design and debugging.

- *User-hostility.* Users of esoteric functions must have a good knowledge of the hardware. The development time necessary to make every feature idiot-proof and user friendly is sometimes prohibitive.

### 6.1.1 Computer interfaces

Precise timing on PC's is difficult because asynchronous events (specifically interrupts) can take hundreds of microseconds of processing time from the microprocessor at a time. These interruptions can cause errors with the high data transfer rates characteristic of spectrum-imaging.

The solution is to use direct-memory access (DMA) to transfer large amounts of data (such as EELS spectra) and external timers to signal (using interrupts) the end of data collection.

DMA is fast because it does not rely on the microprocessor to store data from an I/O device into memory. It can store information while the processor is working on something else. (see figure 6-1.) DMA is used to transfer bright- and dark-field data, x-ray data, and EELS spectra. An important design philosophy for this project was to use DMA whenever more than 1000 bytes of information per second were likely to be transferred. This minimizes the processors' involvement in data collection, allowing it to do other tasks.

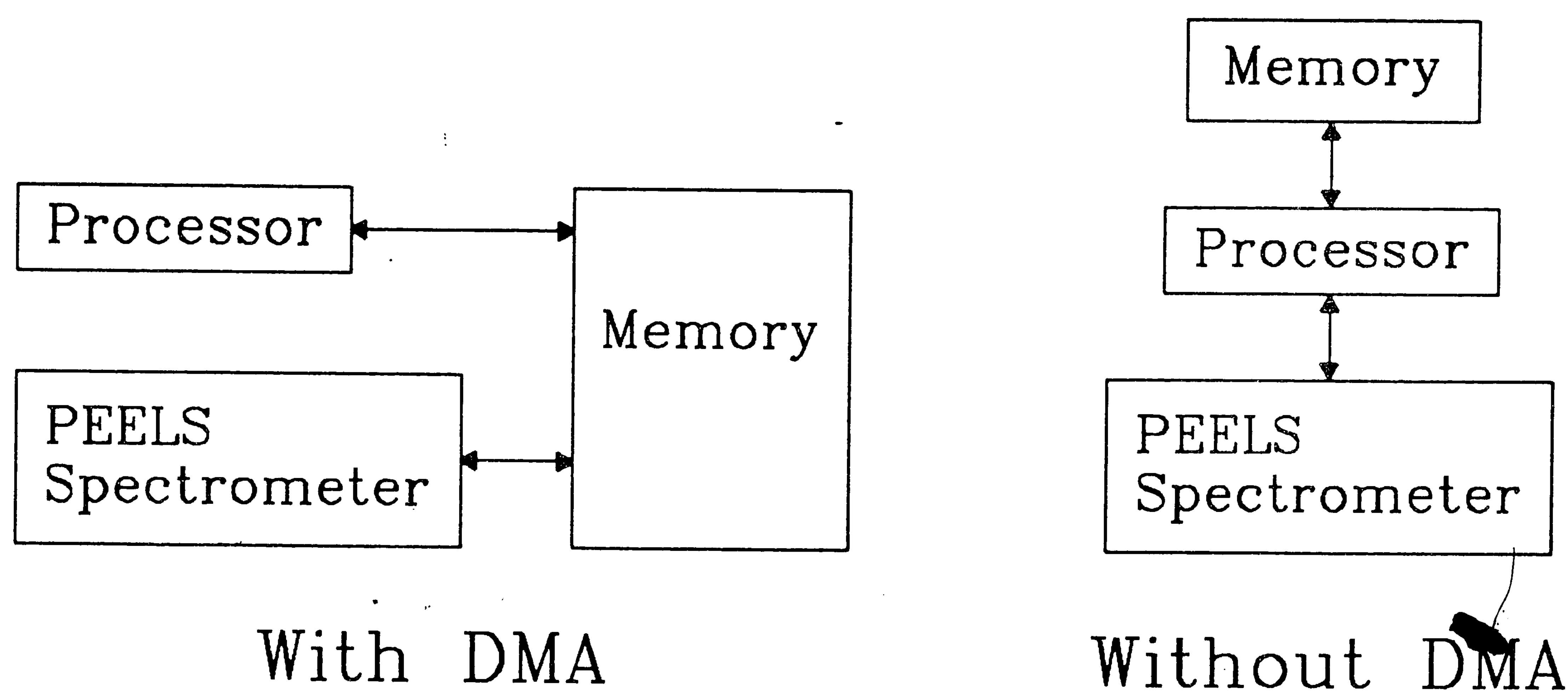


**Figure 6-1:** Transfer of data from an I/O device into memory with and without DMA.

Interrupts are signals to the processor indicating that another task needs servicing. The processor save some information about the task it is currently

executing and then jumps to the new *interrupt service routine.* When this routine is finished the processor returns to the original task. Interrupts are used in this design to signal the end of dwell times while imaging, and to indicate that an error has occured with some pieces of the hardware.

### 6.1.2 System connections

The general connectivity of the system is shown in figure 6-2. Subsequent figures show further detail where relevant.

## 6.2 Software processes

Hardware control is performed through machine-language drivers called from a HLL. The software drivers and hardware were designed to minimize processor involvement in the data collection process, resulting in the capability to collect data while processing continues within the parent HLL.

EELS spectra were initially viewed and recorded with a few lines of FORTRAN. Shortly after, 1024 channel EELS spectra were saved at each point in images as large as 256x256 with as little as 50 lines of FORTRAN, and later processed with several hundred lines of C. Acquisition of spectra and images have since advanced considerably, but the process remains inherently simple.

Experiments designed in HLLs that use the aforementioned drivers are easily constructed. The data acquisition coding is straightforward and terse because the experimenter is shielded from the minutiae of device level programming. When coding is uncomplicated, a user is more likely to attend to detail that will improve the quality of the experiment. Since the choice of HLL is arbitrary the user can most likely choose a familiar development environment, thus speeding development and increasing the inclination to undertake more complex experiments.

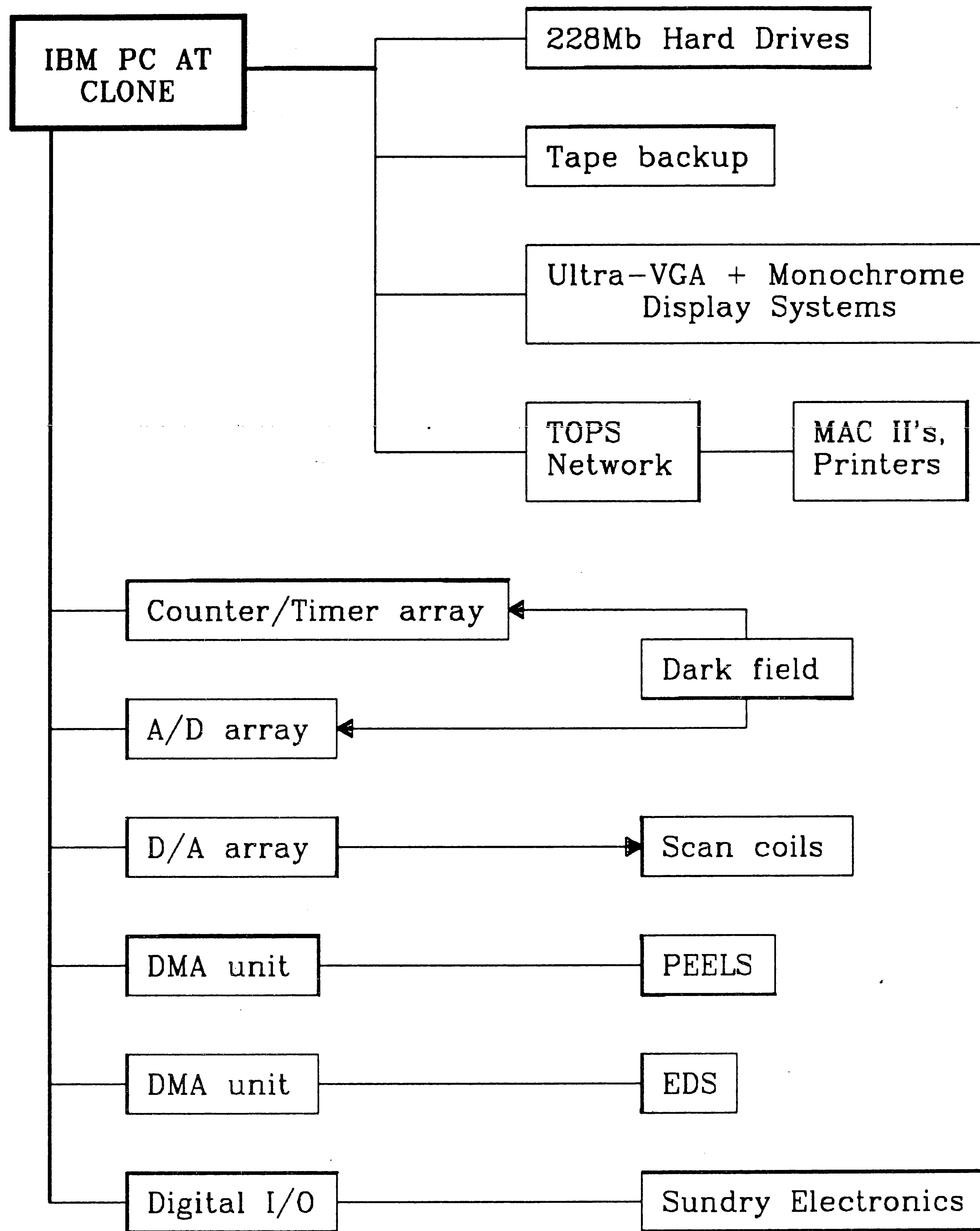


**Figure 6-2:** System connections of the spectrum-imaging system.

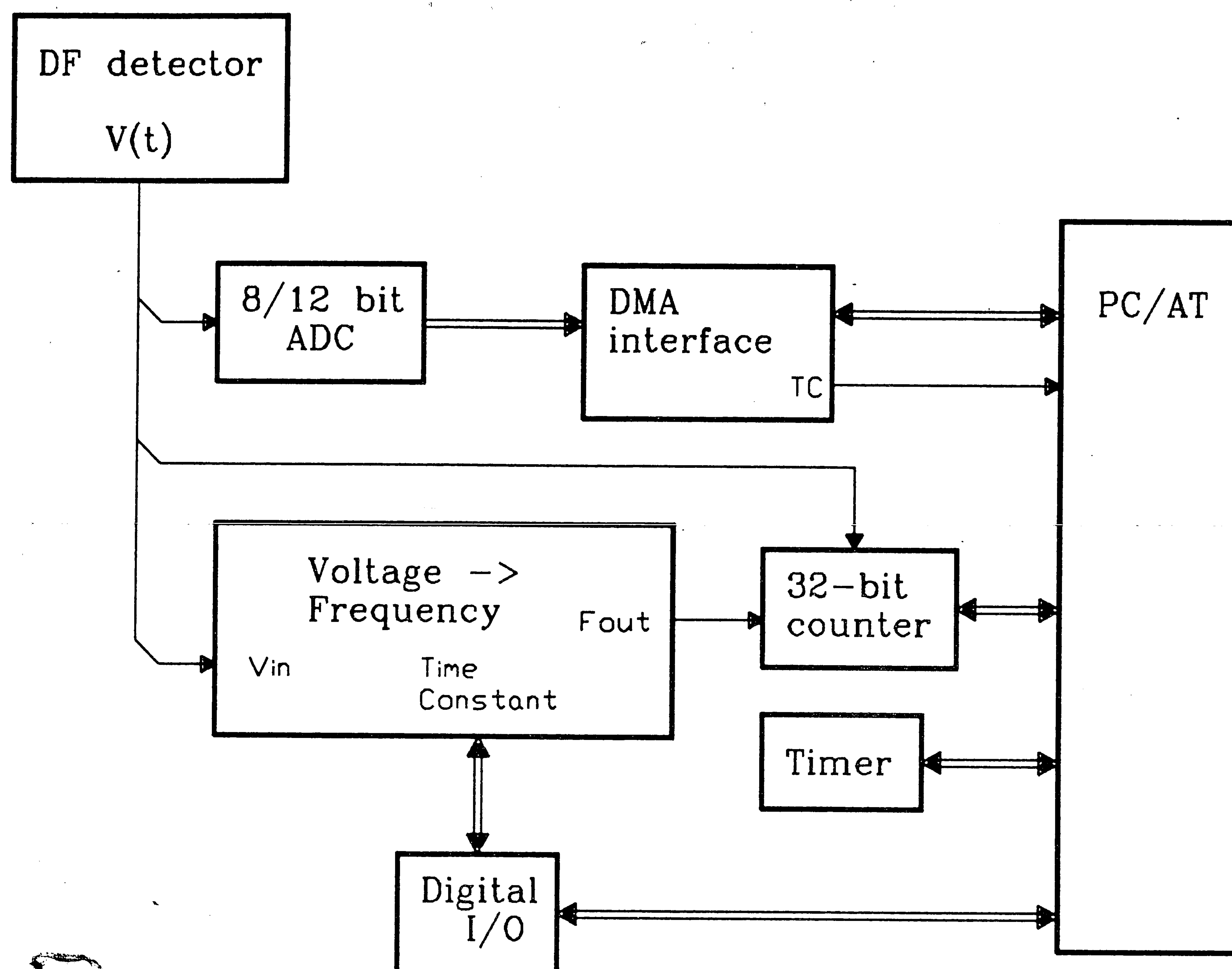


**Figure 6-3:** Dark-field acquistion interface.

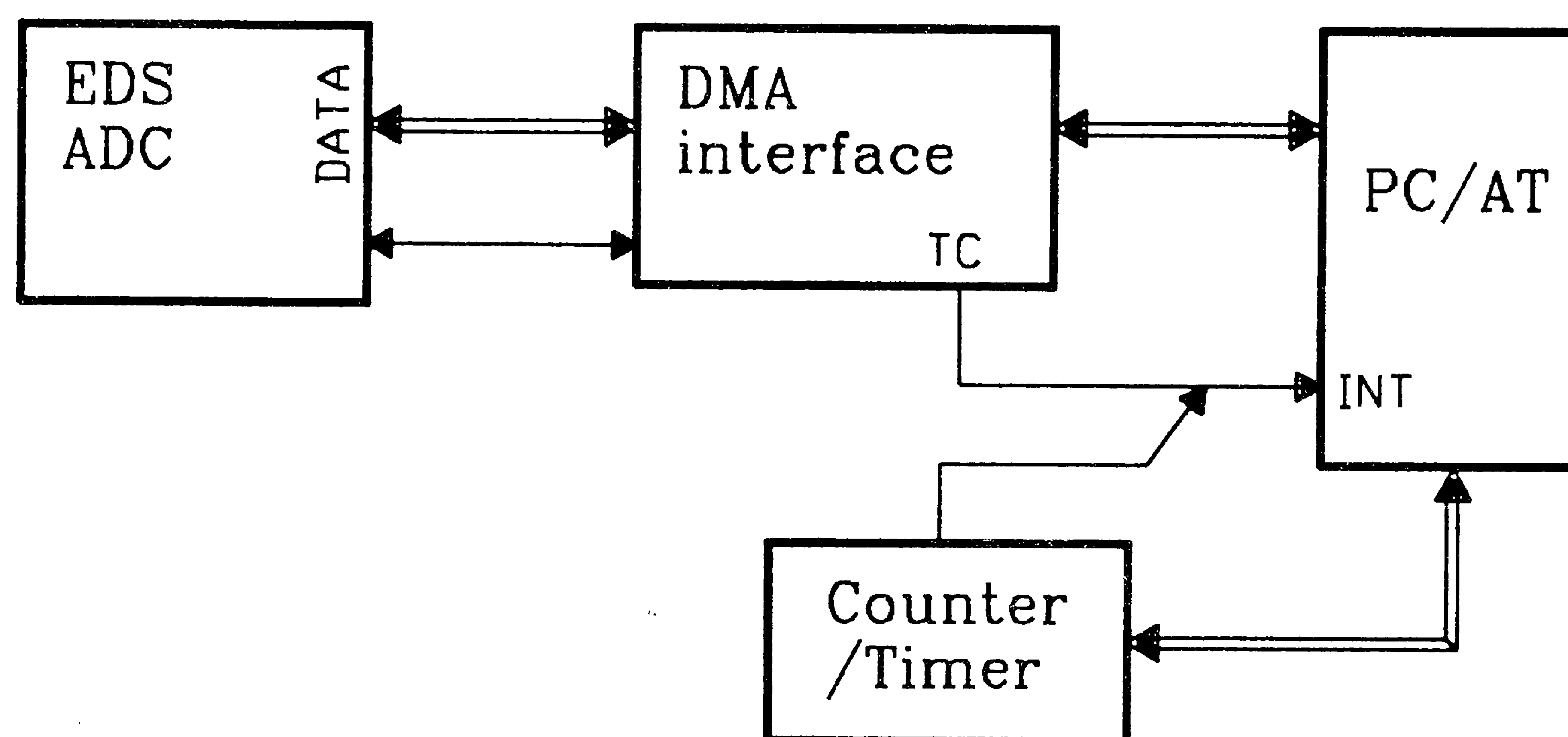


**Figure 6-4:** EDS interface.

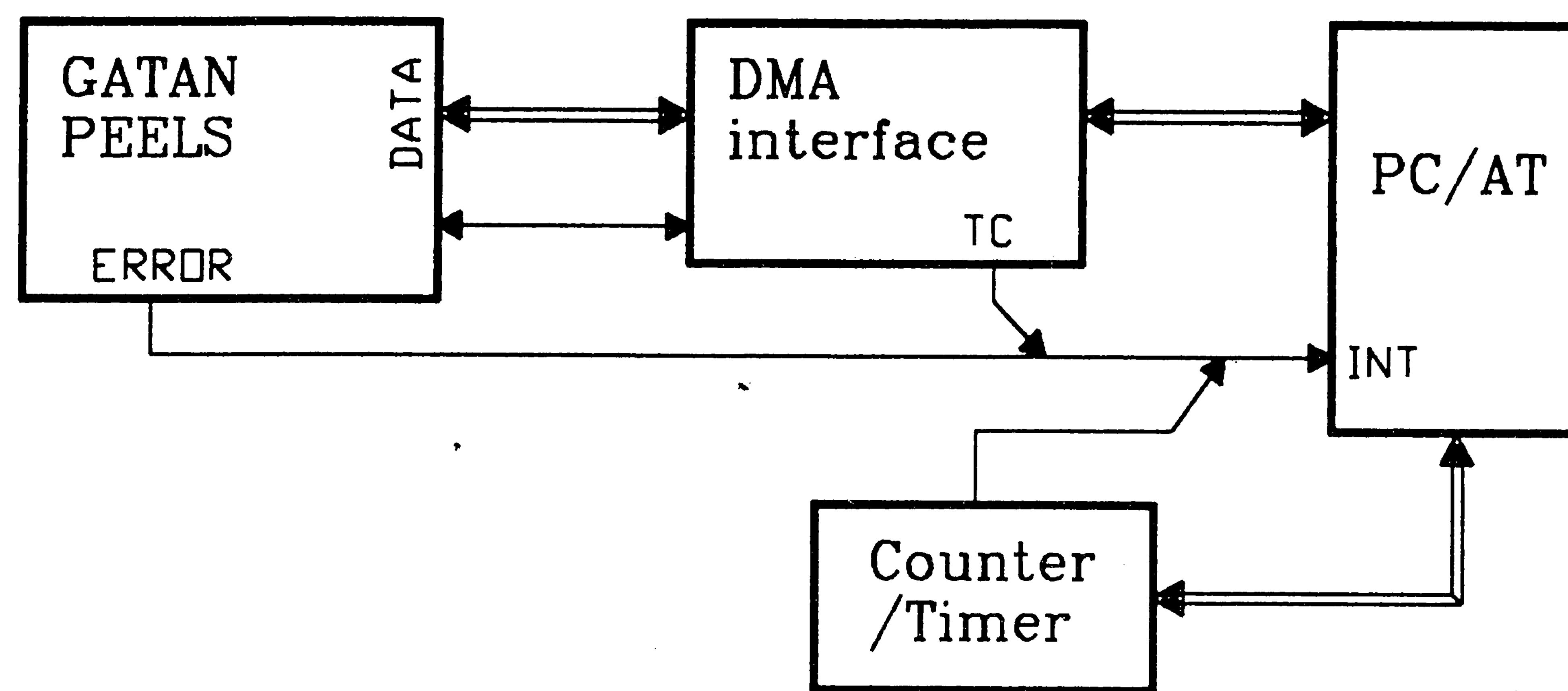


**Figure 6-5:** PEELS spectrometer interface.

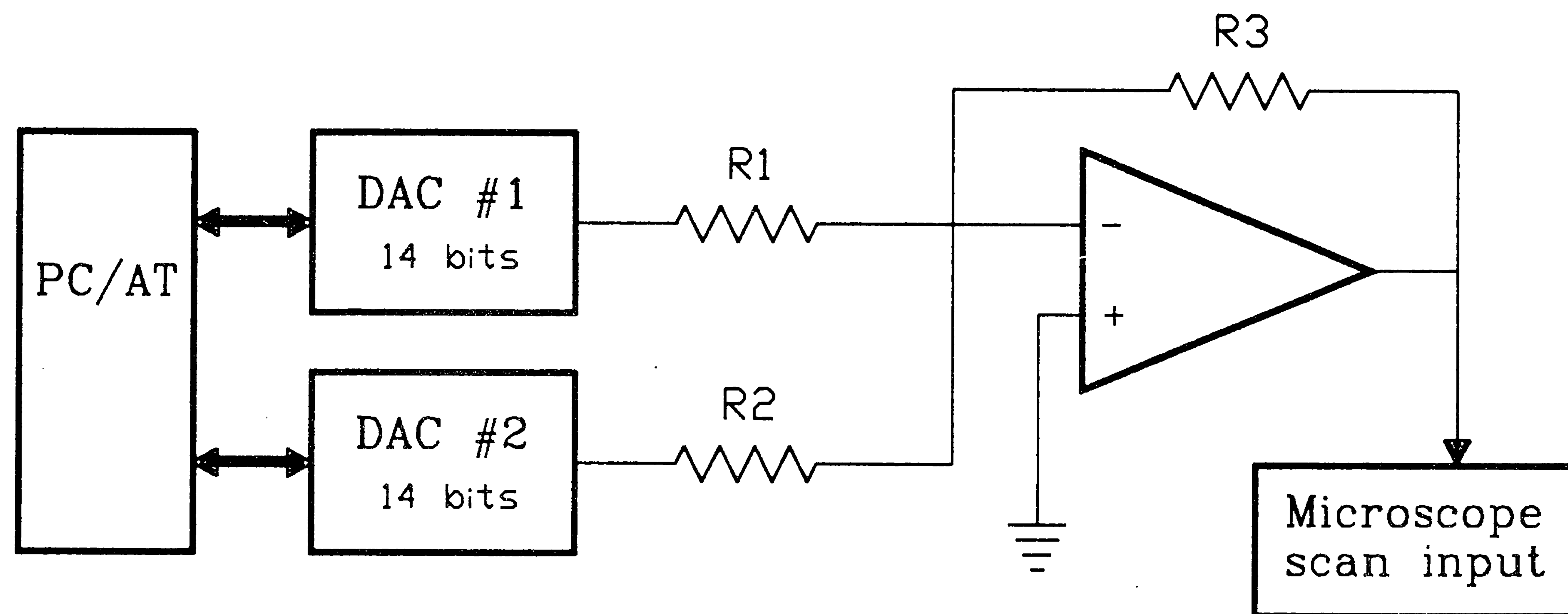


**Figure 6-6:** Scanning coils interface. One circuit is used for each of two scan inputs.

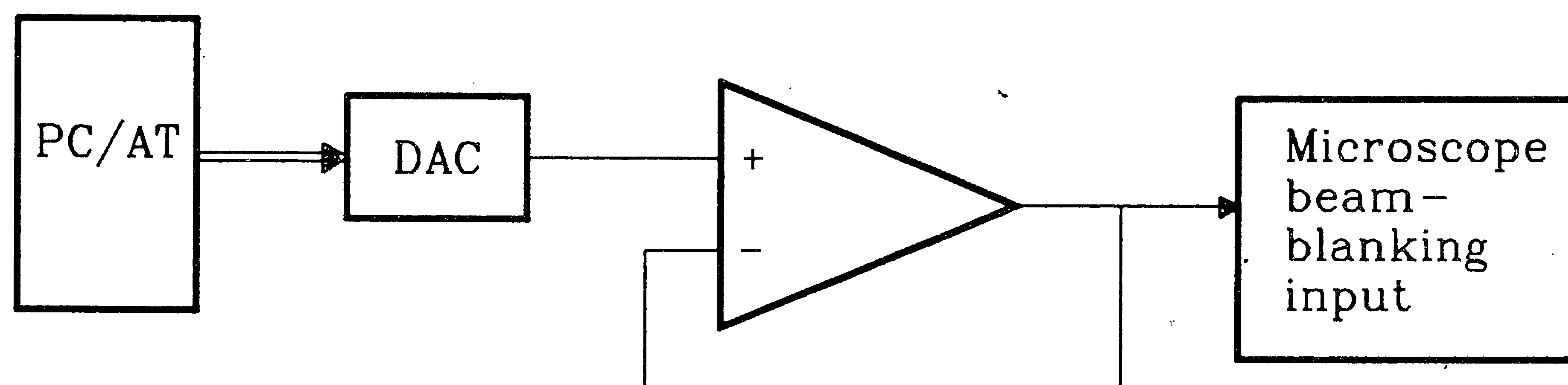


**Figure 6-7:** CRT beam blanking interface.

### 6.2.1 Machine-level drivers

The device drivers, or the software that directly communicates with the hardware, were written in machine language to maximize speed. To understand how these rountines work it is first necessary to understand how data is transferred from the spectrometers.

The PEELS spectrometer begins acquisition when it receives a command from the computer. It continues to collect and transmit spectra until a stop command is issued, or there is an error. When the start command is issued there is a setup delay equal to the readout time of the detector (see figure 6-8). Afterwards, the shield current is digitized and sent to the computer. The next data does not arrive until after the integration time has elapsed. From then on the array counts are transmitted in rapid succession until the entire array has been read out. The computer has either 9 or 18 microseconds to store each word (depending on what the readout time is set for) otherwise the spectrometer reports an error. The process is then repeated except for the setup delay.

A PEELS spectrum is transferred into memory using DMA one integration at a time. At the end of an integration transfer an interrupt is issued and the processor acts on this data. The action is dependent on the routine's initial settings. If a simple, multiple-integration spectrum is desired then the routine sums the integrations in a buffer. In a time-series, the integration is saved on disk or in memory as a separate spectrum. In a spectrum-image, the beam is moved to a new position and the integration is saved on disk or in memory (see figure 6-9). This entire process can be implemented while the parent program continues processing.

X-ray data is somewhat simpler. When an x-ray arrives at the EDS detector it is processed and its energy is output on a bus. The spectrometer will not process another x-ray until this word is read from the bus, so no errors are

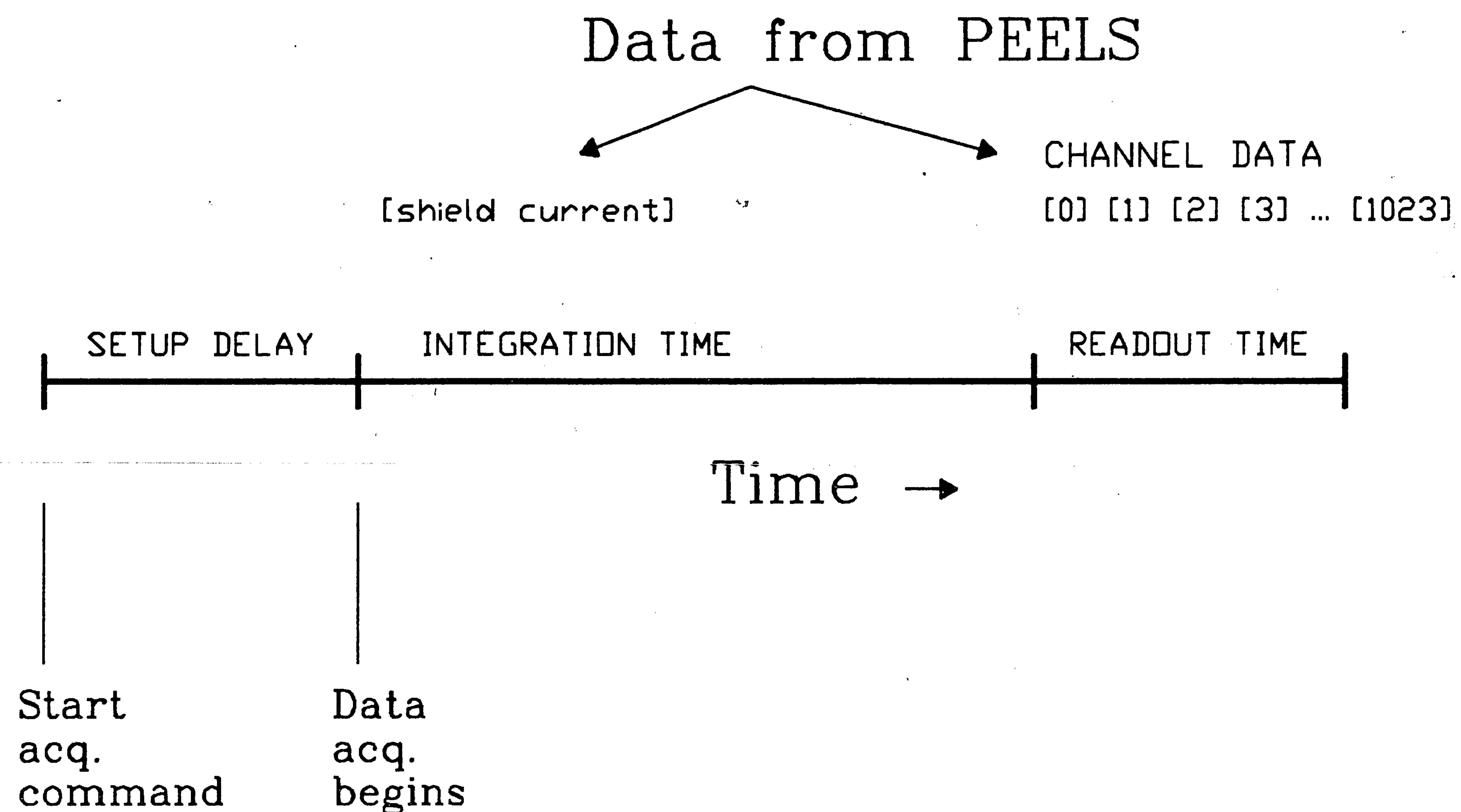


**Figure 6-8:** Diagram of data being transferred from a Gatan PEELS spectrometer.

generated when the computer falls behind in data collection. The processing time of each x-ray is usually dependent on the energy of that x-ray.

The data is transferred into a queue using DMA. When the length of the queue reaches a certain point an interrupt is issued indicating that the data needs to be processed. The data is then read from the queue and stored in a histogram of energy versus counts. The interrupt ends and control is returned to the HLL. Another interrupt is issued when it is time for data collection to stop.

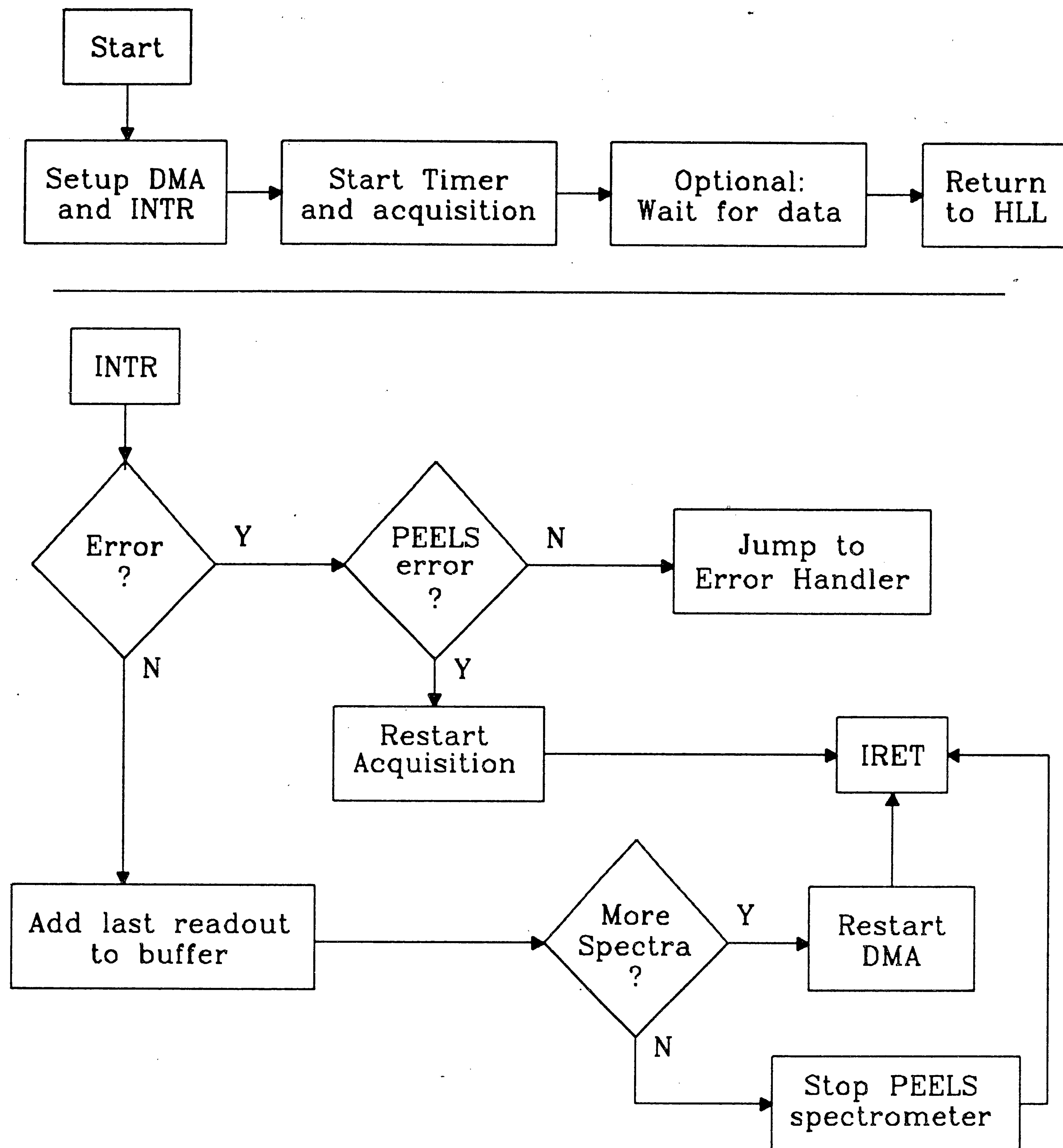


**Figure 6-9:** Flow chart of the PEELS driver.

## 6.3 Calling drivers through HLLs

The machine-language drivers can be combined to create experiments. Figure 6-12 shows how a simple spectrum display program can be written in just a few lines of code. Figure 6-13 shows how to minimize data collection dead time while processing on-the-fly.

More complex experiments are easily created as shown in figure 6-14.

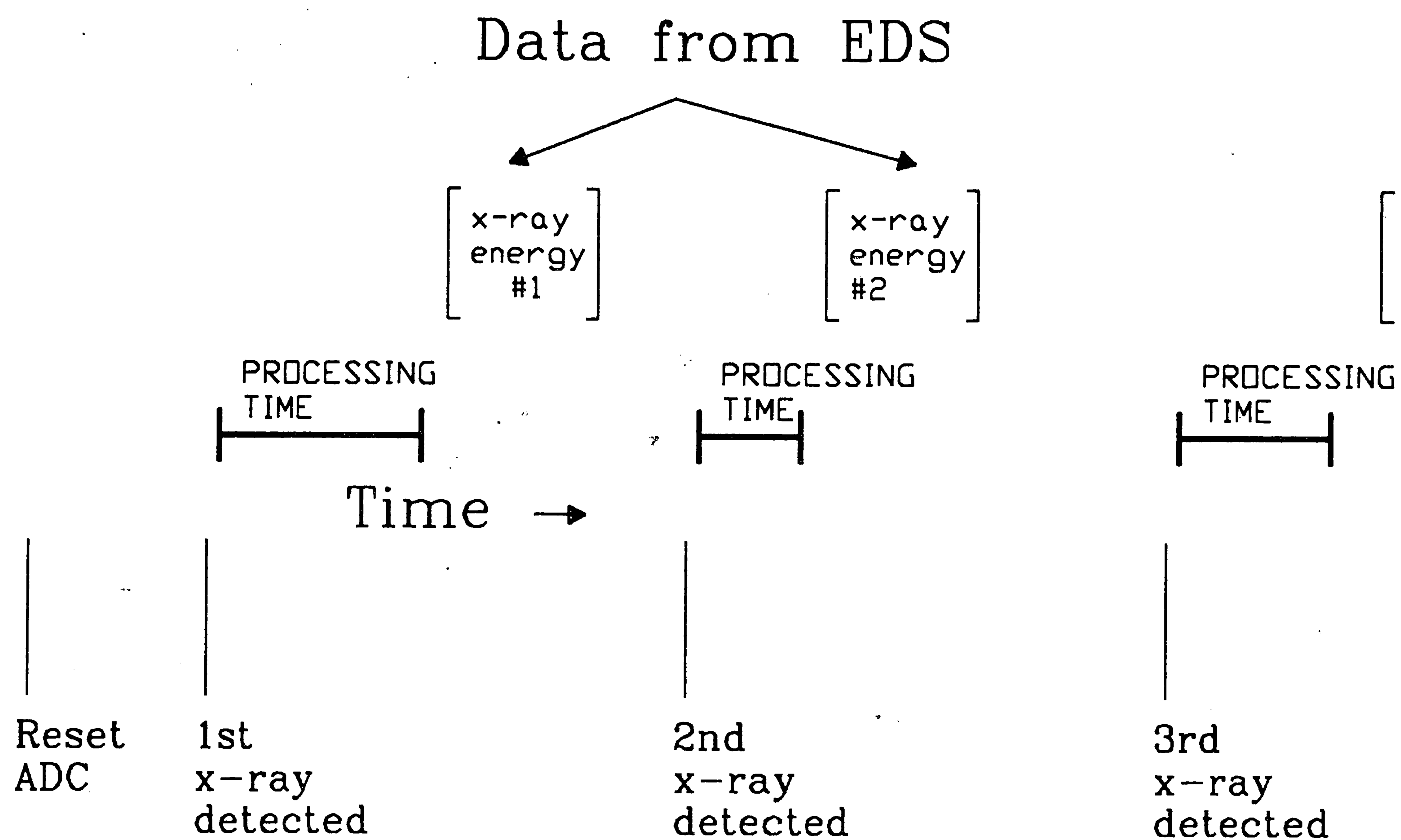


**Figure 6-10:** Diagram of data being transferred from an EDS spectrometer.

These examples show how a pre-specimen beam-blanking circuit can be controlled to minimize the electron dosage. Sometimes the PEELS spectrometer integration time is too lengthy for an experiment; for example when collecting a high-current low-loss signal. The first example shows how the spectrum can be flashed on the array for as little as a few microseconds.

The second example shows how the dosage can be controlled while collecting a time-series. The Gatan PEELS can not always be trusted to record spectra at equal time intervals. This is circumvented by blanking the beam in between integrations.

The third example demonstrates the collection of both core-loss spectra and low-loss spectra. Typically if a core-loss spectrum can be acquired with adequate statistics in under one second, then the accompanying low-loss spectrum will saturate the detector. To prevent the use of the attenuator and the artifacts that it introduces, a beam-blanker is used to flash the low-loss over

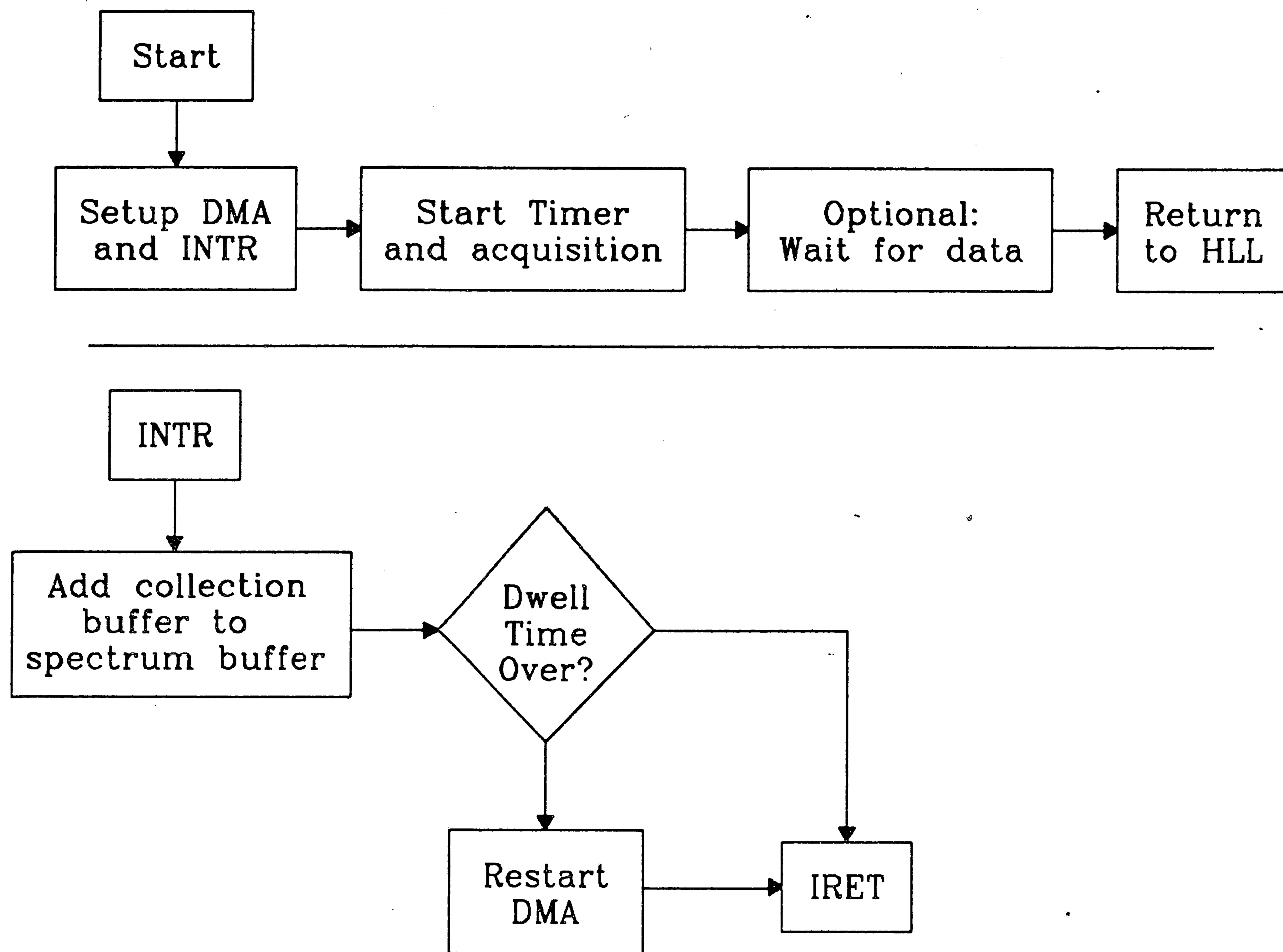


**Figure 6-11:** Flow chart of the EDS driver.

the array.

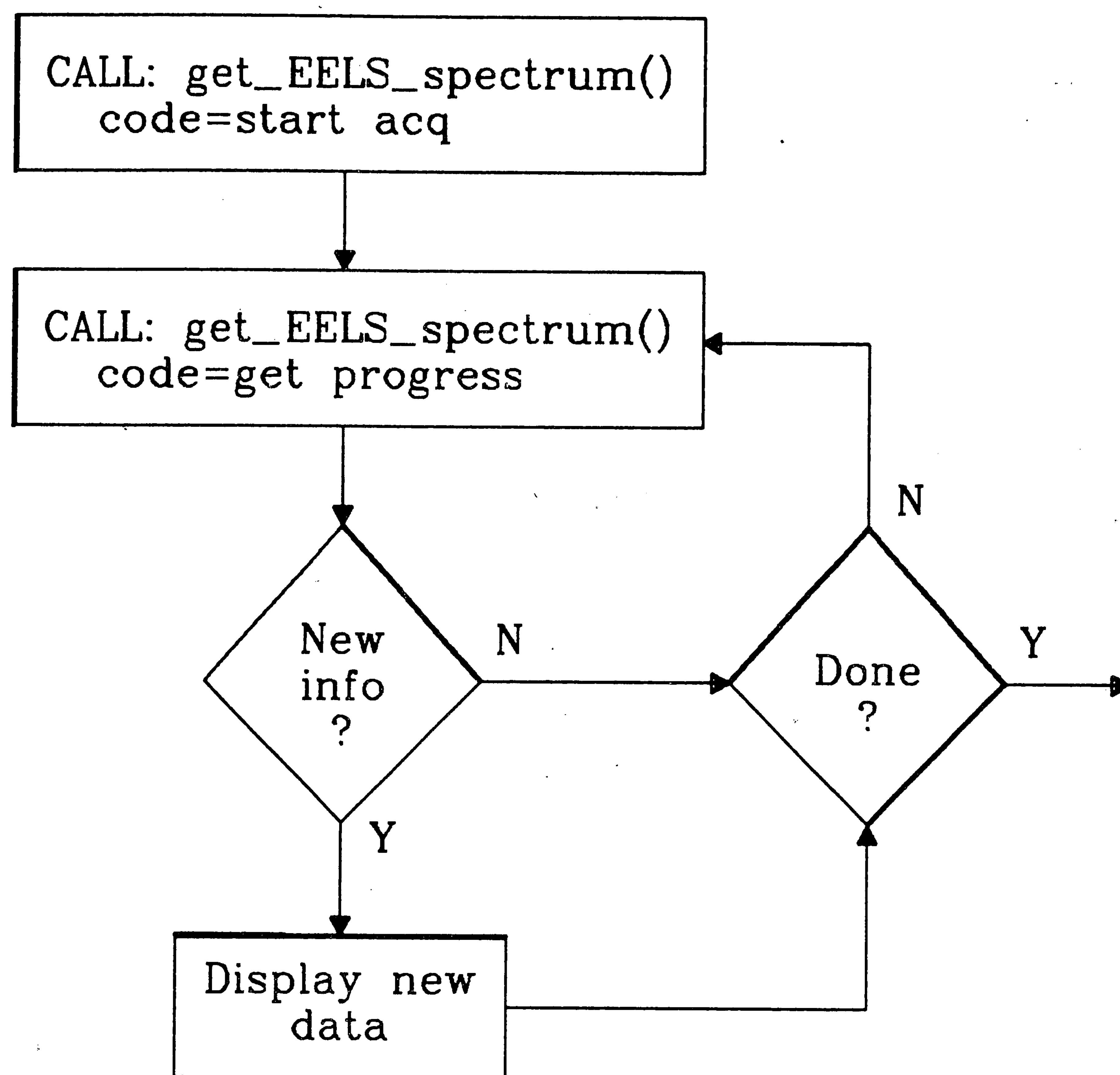


**Figure 6-12:** Flow chart of a simple MCA display routine.

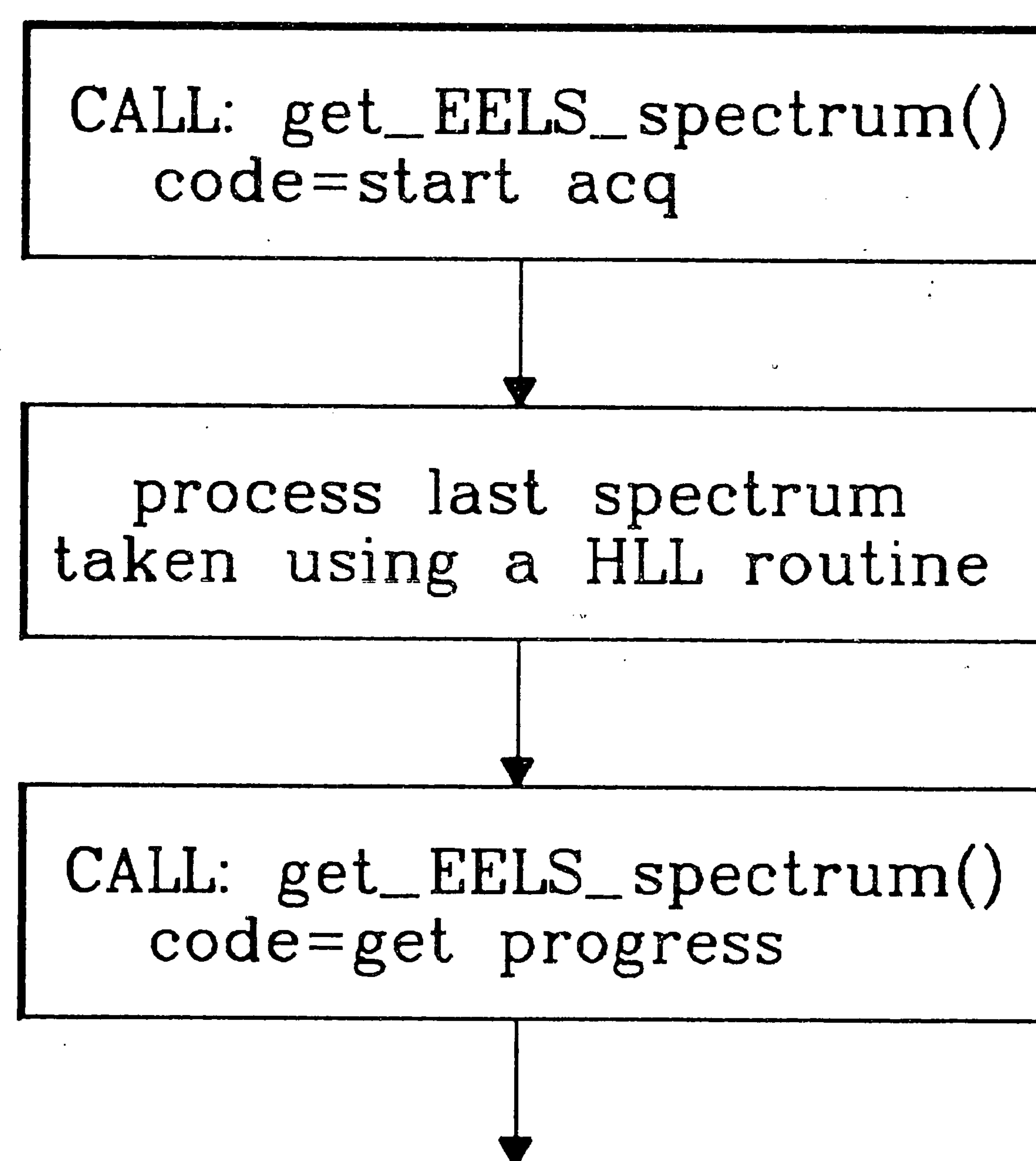


**Figure 6-13:** Minimizing dead time while processing on-the-fly.

d

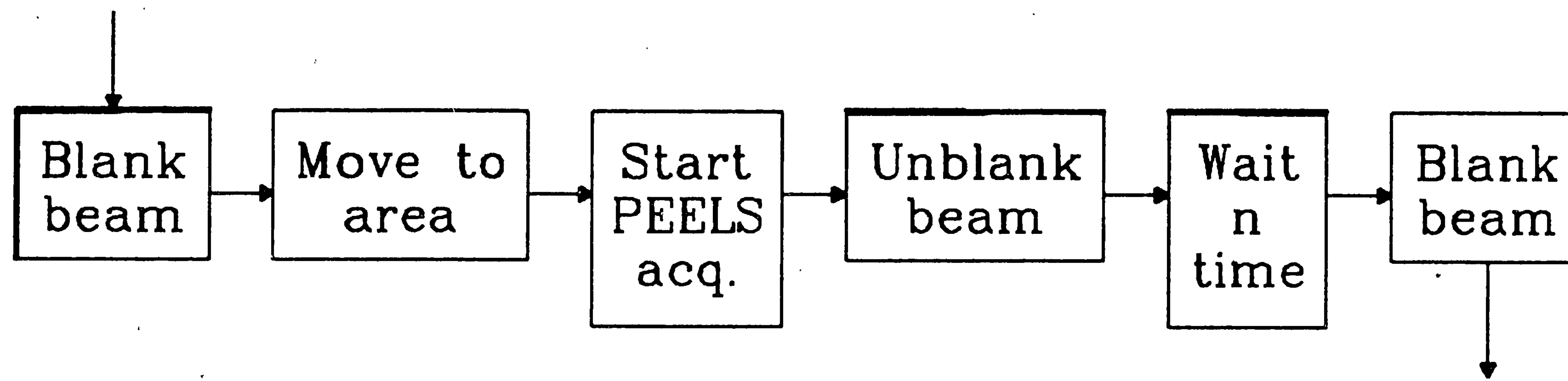


**Figure 6-14:** Minimizing dosage during normal spectrum collection using a pre-specimen beam-blanker.

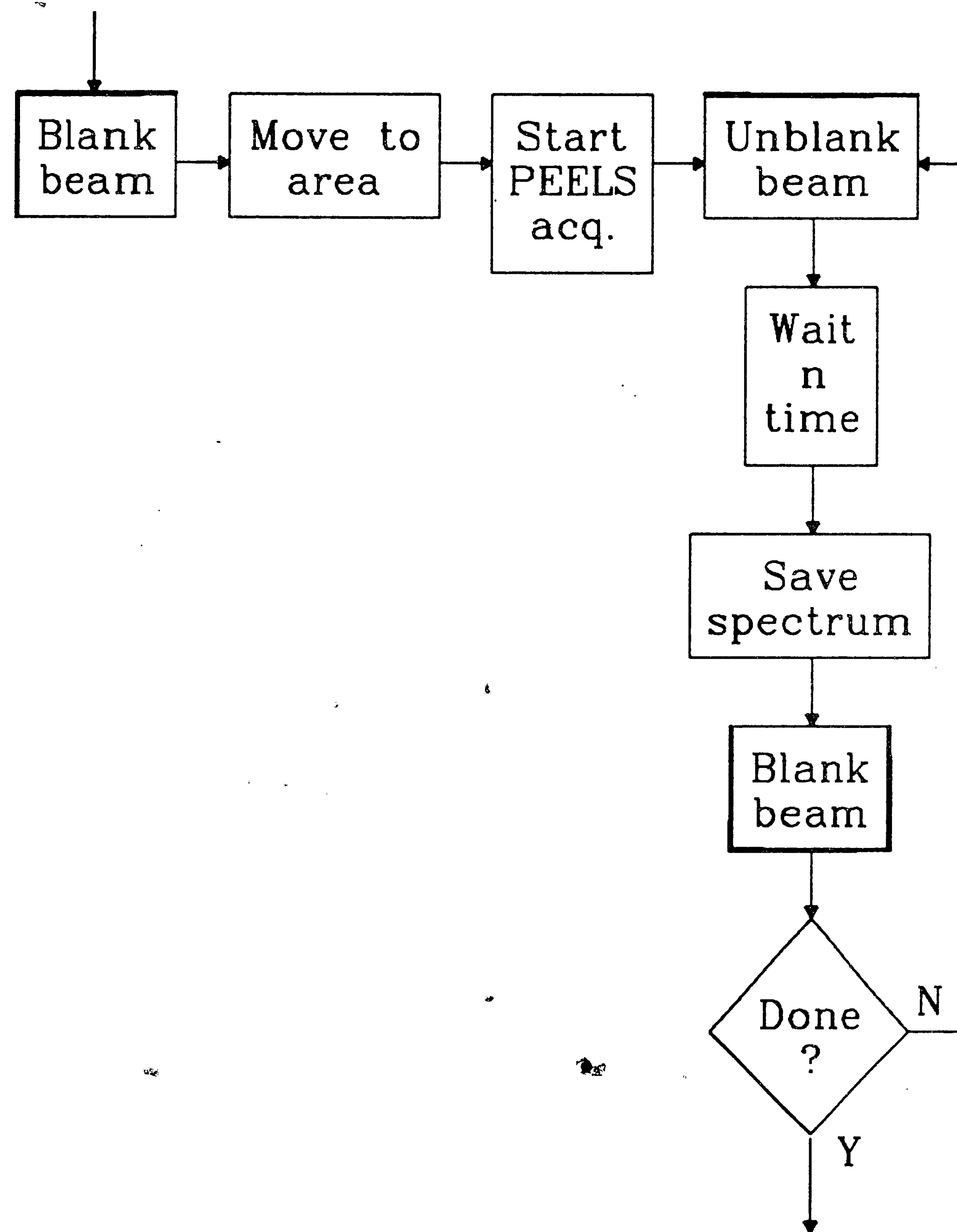


**Figure 6-15:** Collecting mass-loss data with a pre-specimen beam-blanker.

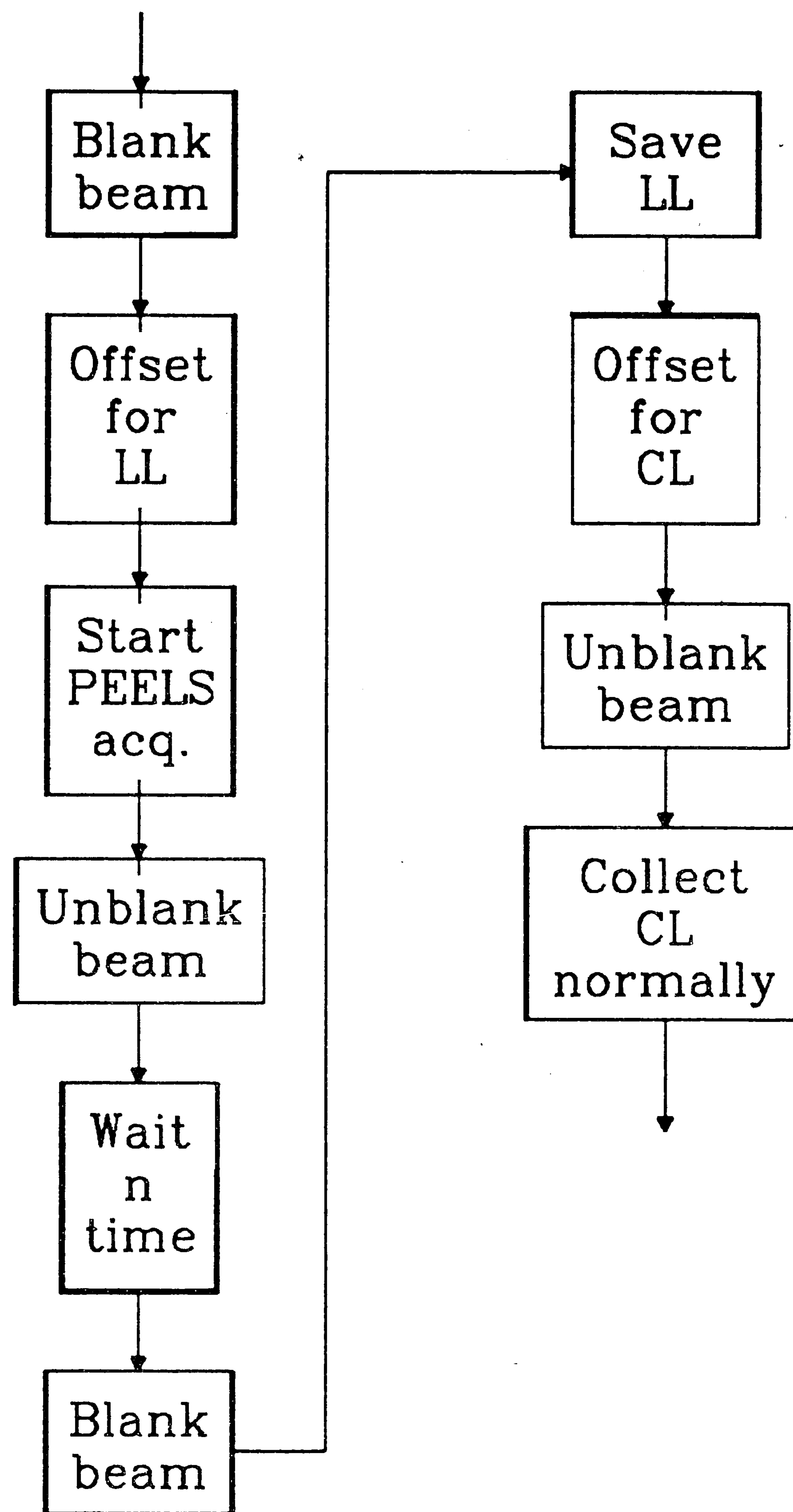


**Figure 6-16:** Collecting both a CL and a LL using a pre-specimen beam-blanker.

# Chapter 7
# Spectrum-imaging software tools

Several pieces of software were written to facilitate spectrum-imaging in addition to the collection software. These "tools" include an MCA package to collect and view a single spectrum, spectrum processing, and spectrum-imaging processing software.

While writing the MCA software, some new and interesting features were developed:

- Real-time auto EELS artifact removal. Dark noise and channel gain variations can be automatically removed from spectra prior to display in both view mode and acquisition mode.

- Artifact library with auto-updating. Dark noise spectra and the channel gain function can be stored and automatically updated. This library is referenced for artifact removal. Use of the library for dark noise removal is often unwise when high accuracy is required.

- Multiple integration view mode. The EELS view mode is a running sum of energy-loss events within a time window. Usually the time window is equal to the integration time, but often the high noise from a single integration hides a feature of interest, and so the time window is enlarged.

- EDS view mode. A running sum of x-ray counts within a time window. A very useful tool.

- Concurrent display of sum and difference spectra. Coordinated movement between these spectra allow easy recognition of trace elements while retaining a normal spectrum.

Spectrum-imaging tools developed:

- Correction algorithm for serious energy drifts.
- Robust spatial drift compensation.
- Program to examine a window of 1, or 9 adjacent spectra within a spectrum-image simultaneously, with the capability to move this window quickly around the spectrum-image.
- Auto-search a spectrum-image for edges.
- Spectrum image calculator. Performs mathematical manipulation of 1 or more spectra within a spectrum-image with another spectra or a constant. Also has smoothing, integration, difference, etc.

# Chapter 8
# Sample experiments

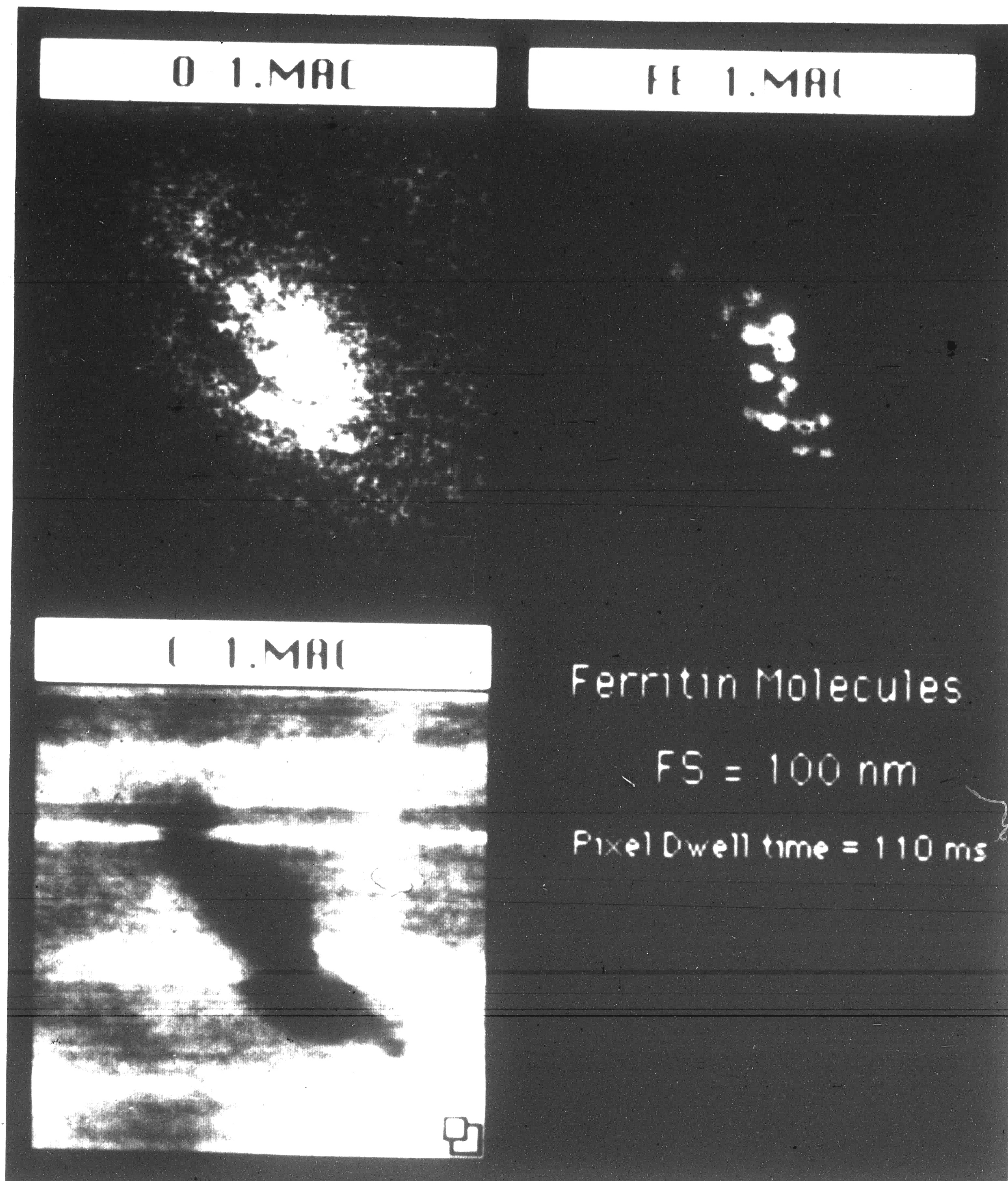


**Figure 8-1:** Processed image planes from a spectrum-image of ferritin molecules showing iron, carbon, nitrogen, and oxygen. The analysis method was linear least-squares with energy-drift corrections.

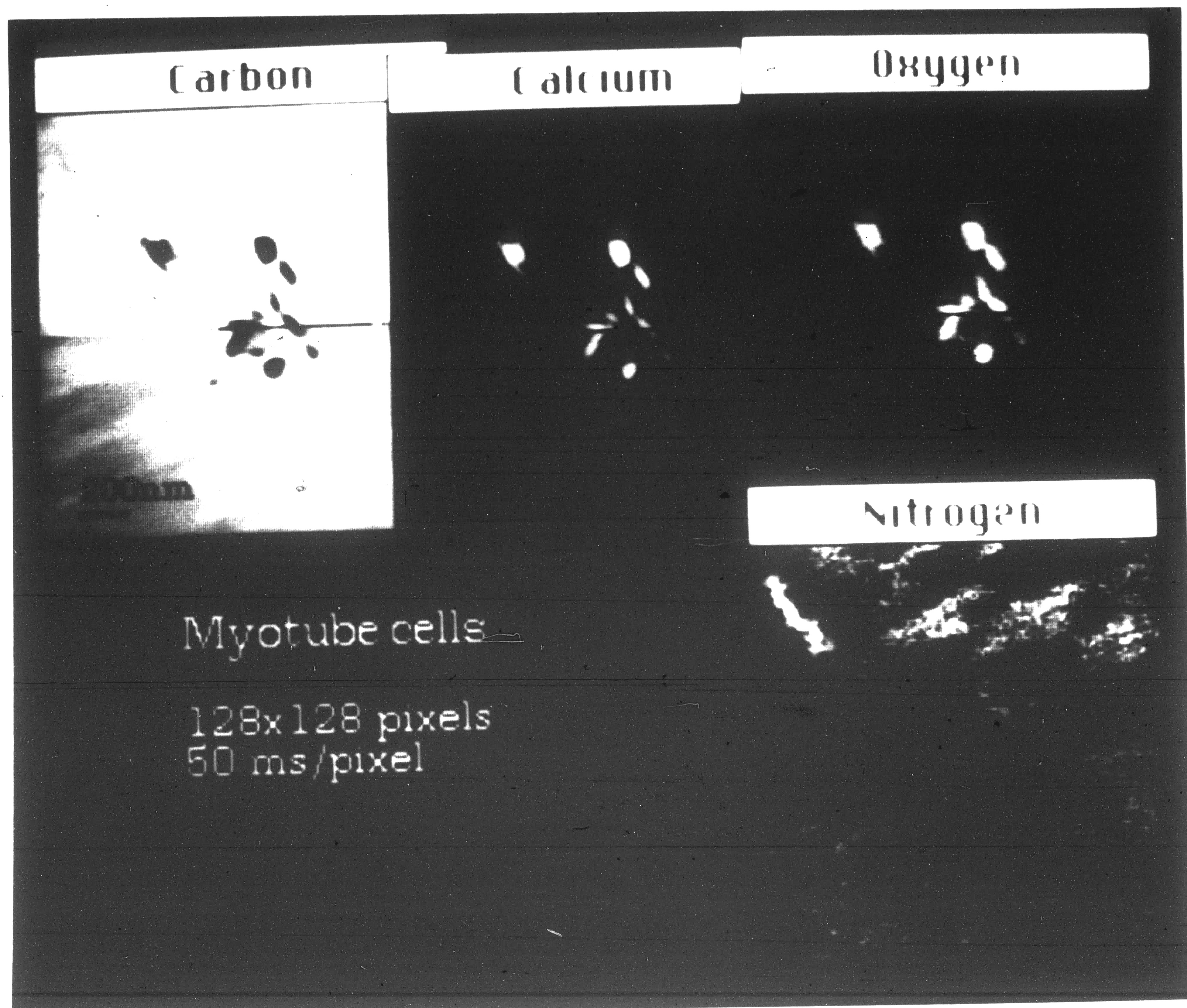


**Figure 8-2:** Processed image planes from a spectrum-image of myotube cells showing nitrogen, carbon, calcium, and oxygen. The analysis method was linear least-squares with energy-drift corrections. Note the total loss of beam current near the middle of the image.

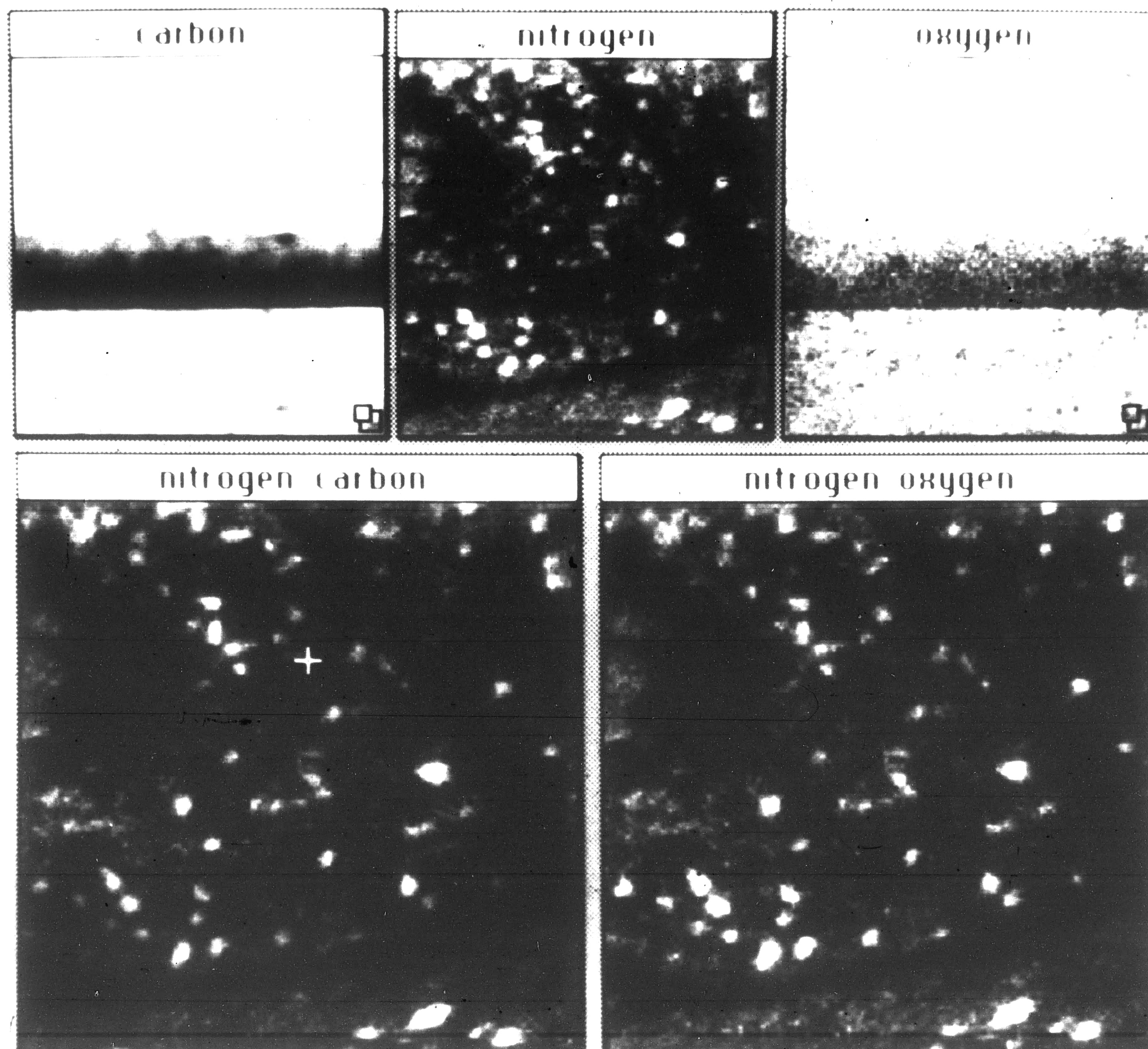


**Figure 8-3:** Processed image planes from a spectrum-image of a beta cell showing carbon, nitrogen, and oxygen without corrected beam current drift artifacts. The planes nitrogen/carbon and nitrogen/carbon show this artifact corrected by ratioing the nitrogen and oxygen planes to a plane of a major constituent (carbon). Notice the increase in noise in the corrected planes where there is large difference in beam current. The analysis method was linear least-squares with energy-drift corrections and spatial drift corrections.

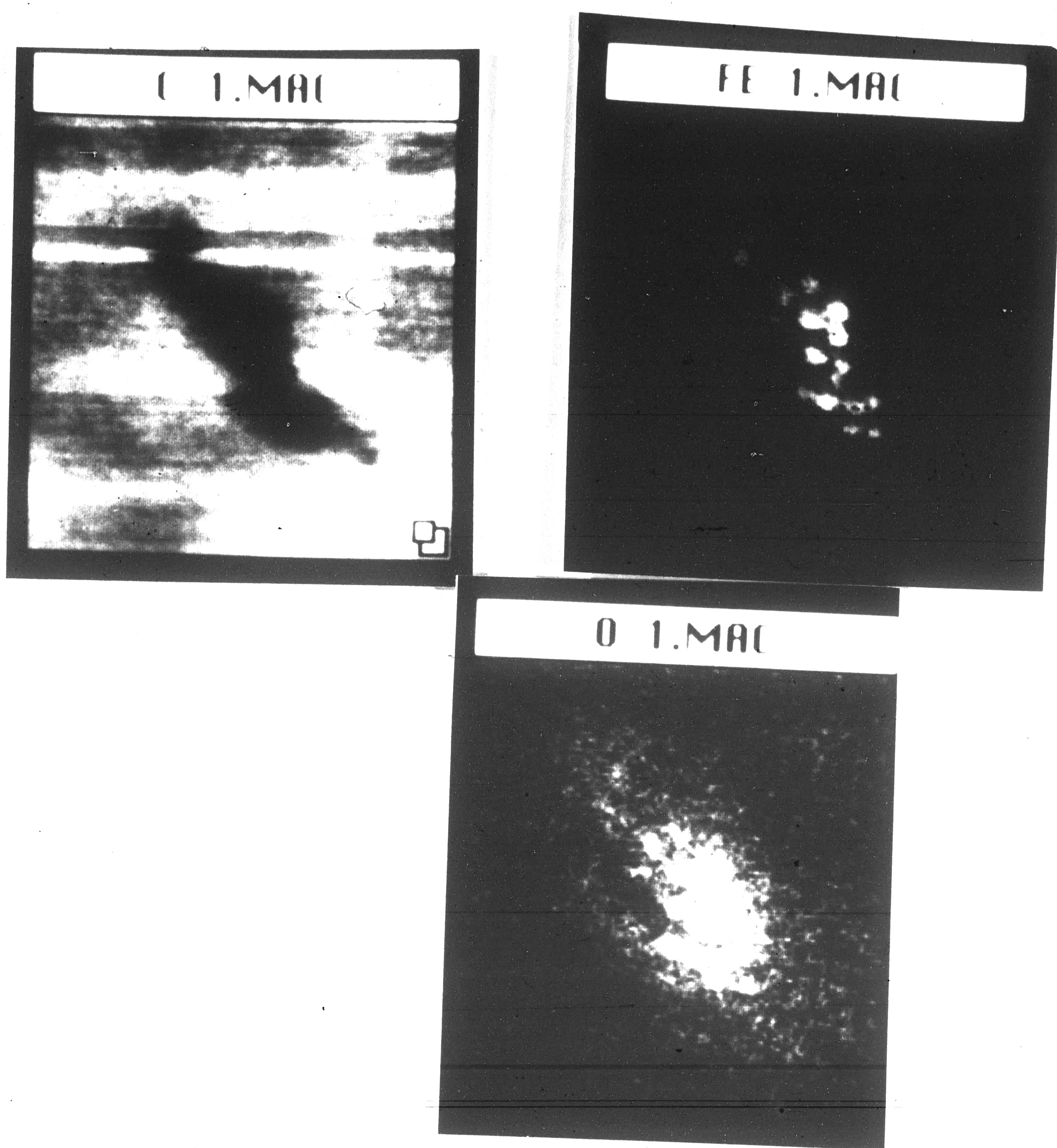


**Figure 8-4:** Oxygen, Iron, and Carbon image planes from a spectrum-image of Ferritin molecules.

Topography of Beta Cell Carbon Image (64 x 64)

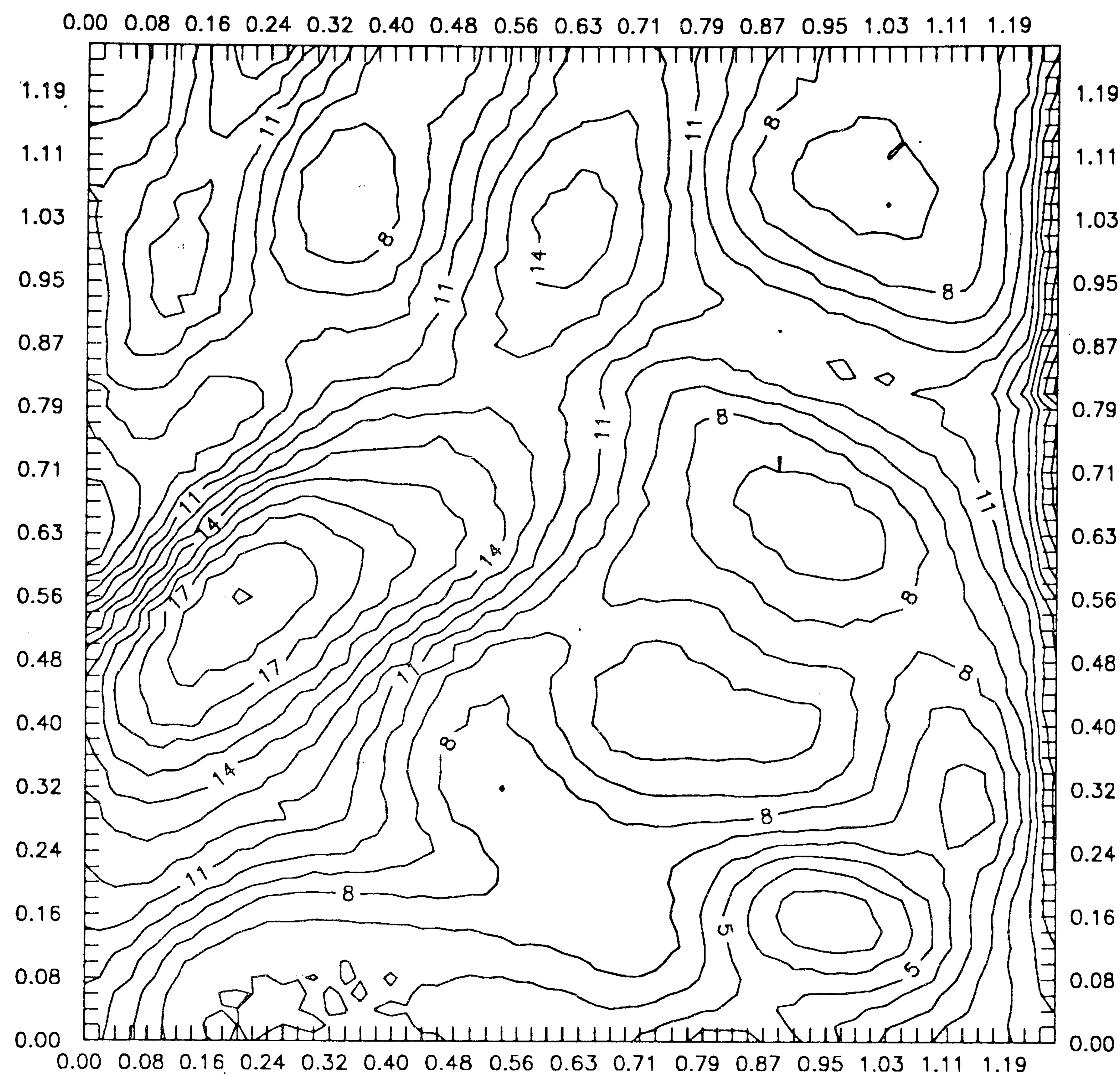


**Figure 8-5:** Processed carbon plane from a spectrum-image of a beta cell. The data has been smoothed spatial and plotted as a topographical map. independent dimensions are spatial coordinates, the dependent axis is absolute mass. The analysis method was linear least-squares.

# Chapter 9
# Conclusions

## 9.1 Summary of design achievements

To achieve spectrum-imaging in the electron microscope, several smaller goals were first accomplished. These include:

- A spectrum-image collection system was developed using a personal computer, expansion perpherals, and custom electronics. This allowed concurrent collection of parallel EELS spectra, EDS x-ray spectra, single-electron counting or current-measurement dark-field signals, measurement of current falling on apertures, and time. Modifications were made to the microscope to permit installation of this hardware; including external digital control of the scan coils.

- Acquisition code was written to optimize the collection of data through the hardware. Unique methods were developed to handle up to one-third of a megabyte per second of asynchronous data, and to handle spectrum-images as large as 256 megabytes. These routines were written to be called from a parent high-level language such as C or FORTRAN. Many of the routines can actively collect and process data in the background while the parent program runs as the foreground task. This construction allows straightforward and flexible design of experiments.

- New methods of artifact correction were necessary to compensate for variations in probe energy and current, specimen drift, and spectrometer artifacts. Some older techniques for correcting artifacts were implemented and evaluated.

- Standard methods of EELS spectrum analysis were extended to work on spectrum-images including linear-least squares, two-area background removal, and difference spectra. The multiple least-squares method of (Shuman..,1987) and later (Leapman..,1988) was extended to a general case so it could be used with materials systems. Techniques for calculating dielectric response and for examining extended fine structure (EXELFS) were implemented for point-analysis and evaluated for extension to spectrum-imaging.

- New methods and software tools were designed to view, search, and process spectrum-images. Edge-search algorithms were created to find unanticipated core-loss edges in a spectrum-image. A spectrum-image calculator was written to manipulate constants, spectra, images, or spectrum-images as objects, and to perform operations on or between these objects.

## 9.2 Summary of experiments

- Single-point analysis using EELS quantitative methods, plural scattering deconvolution, dielectric response computation, ELNES, and EXELFS.

- Spectrum-image analysis of several quantificational methods. Many quantitative image planes were generated from spectrum-images using linear least-squares removal of the background beneath a core-loss edge and a host of artifact correction methods.

- The near-edge structure of carbon was used to image three allotropes of carbon sperately from the same core-loss edge at every point in a spectrum-image.

- Radiation-induced mass-loss measurement using spectrum-images with an independent time or electron-dosage dimension.

## 9.3 The future of spectrum-imaging

The system described in this thesis collects EELS and x-ray data as fast as the spectrometers can transmit it. The collection and storage of spectrum-images is performed with no collection dead time. However this system would be inadequate for some ultra-fast readout CCD EELS spectrometers that will eventually reach fruition. Such a system will require a huge amount (16M or more) of fast memory (perhaps in a frame grabber) to collect 512x512 point spectrum-images in less than five seconds. This would be particularly useful for imaging catalysts and biological specimens that are extremely sensitive to electron radiation.

Spectra collected in the aforementioned system could potentially have only 1 or 2 counts per channel. Fortunately the CCD systems can be biased so they exhibit no dark noise and with the aid of an image intensifier placed before the CCD array, it would remain sensitive to single electrons. The spectra would require new methods of quantification. The most obvious method would be to display a single-electron counted dark-field image and have the user select areas of the spectrum-image to be combined using a mouse. The combined spectra would have better statistics than a single point and could be analyzed using techniques discussed in this thesis. This method would quatitatively take advantage of the spatial statistics of the spectrum-image and is probably the most important and obvious future development for spectrum-imaging.

More work needs to be done on utilizing both low-loss and core-loss structure of an EELS spectrum as an imaging signal. Further experiments may include plasmon shift imaging, surface and interfacial plasmon imaging,

EXELFS and ELNES imaging, and dielectric response imaging. Further work is needed using MLS techniques for quantificational imaging.

## 9.4 Summing up ...

Spectrum-imaging has clear advantages over the traditional "on-the-fly-processing" imaging techniques currently used by many commercially available systems.

- Processing individual EELS spectra in an image "on-the-fly" is often insufficient for quantitative imaging. The capability to process the spectrum-image multiple times is gained by saving the entire spectrum- image.

- Erroneous fitting and unexpected acquisition problems that frequently cause "on-the-fly" processing errors can often be overcome through modifications to the processing software without re-acquiring the image.

- Edges whose existence were not predicted prior to acquisition can also be processed.

- Processing time need not be limited to acquisition time, and thus complicated and robust analysis routines may be used. MLS routines in place of linear least-squares (LLS) and area ratio techniques can greatly improve accuracy and detectability. Other time-consuming analysis methods such as isolating chemical effects and dielectric information can be employed. Processing time for such routines most likely far exceed the desired acquisition time, particularly when specimen drift, beam sensitivity, and microscope operating costs are concerns.

# References

Ahn, C. C., and Krivanek, O. L. (1983) EELS Atlas, Arizona State University.

Barbour, J. C., Mayer, J. W., Grunes, L. A. (1984) An investigation of electron energy-loss spectroscopy used for composition analysis of crystalline and amorphous specimens. *Ultramicroscopy*, **14**, pp 79-84.

Beiser, A. (1987) Concepts of Modern Physics. 4th ed. New York, Plenum Press.

Boersch, H. & Geiger, J., Stickel, W. (1962) "Steigerung der Auflosung bei der Elektronen-Energieanalyse", (translation) Phys. Lett. **3**, pp64-6.

Bourdillon, A. J., El Mashri, S. M., Forty, A. J. (1984) Applications of extended energy-loss fine structure to the study of aluminum oxide films. *Phil. Mag.*,**49**, pp 341-352.

Colliex, C., Manoubi, T., Gasgnier, M., Brown, L. M. (1985) Near-edge fine structures on EELS core-loss edges. In *Scanning Electron Microscopy - 1985*, SEM Inc., A. M. F. O'Hare, Illinois, Part 2, pp 489-512.

Daniels, J. & Kruger, P. (1970) Electron energy losses and optical constants of Ne and CH(4). *Phys. Status Solidi (b)* 43, pp 659-64.

Disko, M. M., Krivanek, O. L., Rez, P. (1982) Orientation dependent extended fine structure in electron energy-loss spectra. *Phys. Rev. B*, **25**, pp 4252-4255.

Disko, M. M., Spence, J. C. H., Sankey, O. F. (1984) Site symmetry effects in the EELS fine structure of Be(2)C. *42nd Ann. Proc. Electron Microsc. Soc. Am.*, ed. G. W. Bailey, San Francisco, pp 564-565.

Egerton, R. F. (1981) SIGMAL: a program for calculating L-shell ionization cross-sections. *39th Ann. Proc. Electron. Microsc. Soc. Am.* ed. G. Bailey, pp 198-9.

Egerton, R. F. (1986) Electron Energy-Loss Spectroscopy in the Electron Microscope. New York, Plenum Press.

Geiger, J. (1981) Inelastic electron scattering with energy losses in the meV region. *39th Ann. Proc. Electron Microsc. Soc. Am.*, ed. G. W. Bailey, pp 182-5.

Grunes, L. A., Leapman, R. D., Walker, C., Hoffmann, R., Kunz, A. B. (1982) Oxygen K near-edge fine structure: An electron energy-loss investigation with comparisons to new theory for selected 3d transition-metal oxides. *Phys. Rev. B*, **25**, pp 7157-7173.

Hayes, T. M., Hunter, S. H. (1976) Structure of disordered materials from EXAFS in real space. *The Structure of Noncrystalline Materials*, ed. Gaskell, P. H., London, Taylor & Francis, LTD, pp 69-71.

Ibach, H., Mills, D. L. (1986) Electron energy loss spectroscopy and surface vibrations. New York, Academic Press, Inc.

Jeanguillaume, C., Colliex, C. (Nov 1988) Proc. of Electron Beam Induced Spectr. at Very High Spatial Resol. Conf., 349-357.

Johnson, D. E., Csillag, S., Monson, K. L., Stern, E. A. (1981) Analytical electron microscopy using extended energy-loss fine structure (EXELFS). In *Scanning Electron Microscopy*, SEM Inc., A. M. F. O'Hare, Illinois, Part 1, pp 105-115.

Kittel, C. (1986) Introduction to solid state physics - 6th edition. New York, John Wiley & Sons, Inc.

Krivanek, O. (1988) "Parallel-detection electron energy loss spectroscopy", EMSA bulletin **18:1**, pp 65-70.

Leapman, R. (1982) EXELFS spectroscopy of amorphous materials. In *Microbeam Analysis - 1982*, ed. K. F. J. Heinrich, San Francisco Press, San Francisco, pp 11-117.

Leapman, R. & Sywt, C. (1988) "Separation of overlapping core edges in EELS by multiple-least-squares fitting", Ultramicroscopy, *26*, pp 393-404.

Rabe, P., Tolkiehn, G., Werner, A. (1980) Anisotropic EXAFS in GeS. *J. Phys. C*, **13**, pp 1857-1864.

Rez, P. & Ahn, C. (1984) "Comparison of theoretical EELS edges with experimental data." Analytical Electron Microscopy, ed. D.B.Williams & D.C.Joy, San Frans. Press, pp 294-8.

Sayers, D. E., Stern, E. A., Lytle, F. W. (1971) New technique for investigating noncrystalline structures: Fourier analysis of the extended x-ray-absorption fine structure. *Phys. Re. Lett.*, **27**, pp 1204-1207.

Schattschneider, P. (1986) Fundamentals of inelastic electron scattering. New York, Springer-Verlag.

Schnattschneider, P. (1988) "The dielectic description of inelastic electron scattering", Proc. of Electron Beam Induced Spectr. w/High Spatial Resolu., 10-26.

Seeds, M. (1984) Foundations in Astronomy. Belmont, CA, Wadsworth, Inc.

Shuman, H., Kruit, P. (1985) *Rev. Sci. Instr.*, **56** 231-239.

Shuman, H. & Somlyo, A. (1987) "EELS analysis of near-trace-element concentrations of calcium", *Ultramicroscopy*, **21** 23-32.

Tafto, J., and Krivanek, O. L. (1982) Site-specific valence determination by electron energy-loss spectroscopy. *Phys. Rev. Lett.*, **48**, 560-563.

Tafto, J., and Zhu, J. (1982) Electron energy-loss near edge structure (ELNES), a potential technique in the studies of local atomic arrangements. *Ultramicroscopy*, **9**, pp 349-354.

Williams, D. (1987) Pratical Analytical Electron Microscopy in Materials Science. Phillips Electr. Instr.

Zallen, R. (1983) The physics of amorphous solids. New York, John Wiley & Sons, Inc.

# Vita

NAME: John Andrew Hunt

DOB: February 19, 1964

POB: Newark, NJ

PARENTS: John Edward and Alice Mary Halkier, Hunt

DEGREES: B.S. Electrical Engineering, Lehigh University (1987)